

Surveying Star Formation in the Galaxy

by

Adam G. Ginsburg

B.S., Rice University, 2007

M.S., University of Colorado, Boulder, 2009

A thesis submitted to the

Faculty of the Graduate School of the

University of Colorado in partial fulfillment

of the requirements for the degree of

Doctor of Philosophy

Department of Astrophysical and Planetary Sciences

2013

This thesis entitled:
Surveying Star Formation in the Galaxy
written by Adam G. Ginsburg
has been approved for the Department of Astrophysical and Planetary Sciences

John Bally

Prof. Jeremy Darling

Prof. Jason Glenn

Prof. Neal Evans

Date _____

The final copy of this thesis has been examined by the signatories, and we find that both the content and the form meet acceptable presentation standards of scholarly work in the above mentioned discipline.

Ginsburg, Adam G. (Ph.D., Astrophysics)

Surveying Star Formation in the Galaxy

Thesis directed by Prof. John Bally

I studied the formation of massive stars and clusters via millimeter, radio, and infrared observations. The Bolocam Galactic Plane Survey (BGPS) was the first millimeter-wave blind survey of the plane of our Galaxy. I wrote the data reduction pipeline for this survey and produced the final publicly released data products. I ran extensive tests of the pipeline, using simulations to probe its performance.

The BGPS detected over 8000 1.1 mm sources, the largest sample at this wavelength ever detected. As a single-wavelength continuum survey, the BGPS serves as a finder chart for millimeter and radio observations. I therefore performed follow-up surveys of BGPS sources in CO 3-2 and H₂CO, and others did similar follow-ups to measure velocities and distances towards these sources.

H₂CO observations of ultracompact HII regions and other millimeter-bright sources were used to measure the local molecular gas density. These measurements hint that density within molecular clouds does not follow a simple lognormal distribution. They also show that star-forming clouds all contain gas at density $\gtrsim 10^4 \text{ cm}^{-3}$.

I used the BGPS source catalog to identify the most massive compact clumps within the galaxy, identifying 18 with masses $M > 10^4 M_\odot$ in the first quadrant of the Galactic plane. As these objects are all actively star-forming, the starless timescale of massive proto-cluster clumps must be relatively short, with lifetimes $\lesssim 0.6 \text{ Myr}$.

Dedication

To stars and gas, for holding still for a picture.

Acknowledgements

To the people who have helped, family, friends, and colleagues.

Specific help on these projects came from Jim Braatz, Glen Langston, Phil Perrilat, Esteban Araya, Devin Silvia, and Jeff Mangum. Software was developed in collaboration with Jordan Mirocha and Thomas Robitaille. Co-authors who contribute to the works in this paper include: James Aguirre, Jeremy Darling, John Bally, Cara Battersby, Eli Bressert, Erik Rosolowsky, Miranda Dunham, Manuel Merello, Timothy Ellsworth-Bowers, Jason Glenn, Neal Evans, ...

Contents

Chapter

1	Introduction	1
1.1	Preface	1
1.2	Star Formation in the Galaxy	1
1.2.1	Gas Flow and Collapse	3
1.2.2	Turbulence	6
1.2.3	Mass Functions	8
1.3	Outline	11
2	Using outflows to track star formation in the W5 HII region complex	12
2.1	Preface	12
2.2	Introduction	13
2.3	OBSERVATIONS	14
2.3.1	JCMT HARP CO 3-2	14
2.3.2	FCRAO Outer Galaxy Survey	17
2.3.3	Spitzer	17
2.4	Analysis	17
2.4.1	Outflow Detections	17
2.4.2	Structure of the W5 molecular clouds: A thin sheet?	35
2.5	Sub-regions	38

2.5.1	Sh 2-201	38
2.5.2	AFGL 4029	40
2.5.3	W5 Ridge	40
2.5.4	Southern Pillars	44
2.5.5	W5 Southeast	47
2.5.6	W5 Southwest	49
2.5.7	W5 West / IC 1848	50
2.5.8	W5 NW	50
2.6	Discussion	54
2.6.1	Comparison to other outflows	54
2.6.2	Star Formation Activity	57
2.6.3	Evaluating Triggering	58
2.7	Outflow systems beyond W5	59
2.8	Conclusions	60
2.9	Acknowledgements	62
2.10	W5 Appendix: Optically Thin, LTE dipole molecule	63
3	The Bolocam Galactic Plane Survey	68
3.1	Preface	68
3.2	Version 1	68
3.3	Introduction	68
3.4	Calibration	70
3.4.1	Why was there a multiplicative offset in the v1.0 data release?	70
3.4.2	Comparing v1 and v2 calibration	70
3.4.3	Comparison to Other Surveys	71
3.5	Expansion of the BGPS and Observations	73
3.6	Data Reduction and Data Products	75

3.6.1	Sky Subtraction	75
3.6.2	New Map Types	77
3.6.3	Median Maps	78
3.6.4	Pointing	78
3.6.5	Pointing Comparison	79
3.6.6	ATLASGAL offset	83
3.7	The Angular Transfer Function of the BGPS	85
3.7.1	Simulations with synthetic sky and atmosphere	85
3.7.2	The Angular Transfer Function	87
3.7.3	Comparison with other data sets	89
3.7.4	Power Spectral Density comparison	91
3.8	Examination of BGPS and HiGal power-spectra	94
3.9	Source Extraction	96
3.9.1	Catalog Matching between v1.0 and v2.0	96
3.9.2	Source flux density, size, shape, and location distributions	97
3.10	Conclusions	100

Tables

Figures

Chapter 1

Introduction

1.1 Preface

This thesis¹ describes the research I have performed with a wide variety of collaborators, mostly centered on the Bolocam Galactic Plane Survey team led by John Bally and Jason Glenn. The BGPS data reduction process, at the core of this work, was done in collaboration with James Aguirre and Erik Rosolowsky.

However, the work proceeded somewhat haphazardly: I came into the BGPS team as the rare student enthusiastic about data reduction. I never planned to take over the BGPS data, but it happened a few years into my time at CU. This thesis is therefore somewhat scattered: some of the observations reported here were taken as ‘follow-up’ to the BGPS before it was completed.

This document primarily consists of a number of published papers centered around a common theme of radio and millimeter observations of the Galaxy, but without an obvious common driving question. I have therefore added thesis-specific introductions to each section to describe where they fit in to the bigger picture of this document. I’ve also included sections describing work that is not yet published but (hopefully) soon will be.

1.2 Star Formation in the Galaxy

It has been known for at least half a century that stars form from the gravitational collapse of clouds of cool material. The gas that will eventually form stars is typically observed as dark features

¹ Necessarily the first two words of a thesis?

obscuring background stars. The brighter nebulae, which have been studied for far longer (?), contain hot and diffuse gas. These nebulae, while spectacular, are not the construction materials of new stars. However, they mark the locations where new stars have formed - nebulae are often stellar nurseries.

To track down the cool star-forming material, it is necessary to observe at longer wavelengths. Infrared observations can pierce through obscuring material, as dust becomes more transparent at longer wavelengths. With near- and mid-infrared observations, such as those enabled by HgCdTe detectors like those in the NICFPS and TripleSpec instruments at Apache Point Observatory and the InSb detectors used on the Spitzer Space Telescope, it is possible to observe obscured young stars. These objects have just ignited fusion in their cores and represent the youngest generation of new stars.

But this material has already formed stars. To see the truly cold stuff, that which still has potential to form new stars, we need to examine gas that is not heated at all by stars. Assuming we want to look for gas that can form a star like our sun and that the density of the gas to form is $\sim 10^4$ particles per cubic centimeter (an assumption left unjustified for now), the Jeans scale requires a temperature $T \sim 10$ K, which means we need to look at wavelengths $\lambda \gtrsim 100\mu\text{m}$ in order to observe this gas.

Gas at these densities turns out to be quite rare. While there are thousands of stars within 100 pc of the sun, the closest known star-forming globules are at distances greater than 100 pc. While this sparsity is explained in part by our current position in the Galaxy (we're buzzing along its outskirts at 250 km s^{-1}), it reflects the reality that star formation in the present epoch is dispersed and rare.

Even more rare are the massive stars that end their lives in supernovae. While there are hundreds of stellar nurseries within a few hundred parsecs, the nearest region of massive star formation is the Orion Molecular Cloud at a distance of 400 pc. Out to 1000 pc, though, there are still only a handful of massive star forming regions, including Monoceros R2 and Cepheus A.

These massive stars in many ways are the most important to study in order to understand

the evolution of gas and dust in the universe and our own origins. In their deaths, they produce the heavy elements required to form dust, planets, and life. Throughout their lives and deaths, massive stars dump energy into the interstellar medium and effectively control the motions and future of the gas around them.

The bigger the star, the shorter it lives, so massive stars are nearly as rare as their birth regions. They also tend to be found nearby or within these birth regions. Since they can be found near large globs of dust, finding these globs can help us discover new groups of massive stars.

This thesis summarizes surveys within our Galaxy to discover and examine regions forming. The largest body of work described here is the Bolocam Galactic Plane Survey, the first dust continuum survey of a significant fraction of the Galactic Plane.

With that broad overview in place, the next sections describe a few of the specific problems addressed in this thesis in greater detail.

1.2.1 Gas Flow and Collapse

Stars form as the end state of the collapse of gas cores. The classic analysis used to determine when stars will form from a gas cloud is the Jeans analysis, which determines under what conditions an overdensity in a uniform isothermal medium becomes unstable to gravitational collapse. Jeans analysis defines a length scale

$$L_J = \left(\frac{\pi c_s^2}{G\rho_0} \right)^{1/2}$$

and a mass scale

$$M_J = \frac{1}{8} \left(\frac{8\pi kT}{G\mu} \right)^{3/2} \rho_0^{-1/2}$$

which defines the typical mass at which a core should form. In this equation, c_s is the sound speed in the gas, ρ_0 is the density of the medium, T is the gas temperature, μ is the mean mass per particle in amu, and G is the gravitational constant. More careful analyses including other factors, e.g. external pressure on the core, yield similar values.

The Jeans collapse time scale is within a factor of a few of the free-fall collapse time,

$$\tau_{ff} = \left(\frac{3\pi}{32G\rho_0} \right)^{1/2} = \pi \sqrt{\frac{3}{8}} \tau_J$$

$$\tau_J = \left(\frac{1}{4\pi G\rho_0} \right)^{1/2}$$

implying a typical mass infall rate for an isothermal core of

$$\dot{M} = M_J/\tau_J = \pi^2 \sqrt{32} \frac{c_s^3}{G}$$

(or $\dot{M} = 16\pi/\sqrt{3}c_s^3/G$ using τ_{ff}). Under free-fall collapse, then, a $1 M_\odot$ star takes only $\sim 10^4$ years to form, but a $100 M_\odot$ star takes ~ 1 Myr.

Real stars do not form so quickly, but initial accretion rates may be as high as $10^{-4} M_\odot \text{yr}^{-1}$ in cores, and the accretion must be at least that high for massive stars to form in times shorter than the lifetimes of their parent clouds.

Low-mass stars go through subsequent phases of collapse from the initial unstable core to a hydrostatic core in which collapse no longer proceeds isothermally as the dust becomes optically thick to its own radiation. Eventually a protostar forms, surrounded by a disk and a core. The core continues to accrete onto the star through the disk until all the material is either accreted or blown away in outflows. The disk accretes on to the star and forms planets.

This process for low-mass stars is well-understood in the broad strokes outlined here, and each phase in this process has been observationally confirmed. For massive stars, the picture is far less clear. It is still actively debated whether active stars ever have a “core” analogous to low-mass pre-stellar cores, since a $100 M_\odot$ gas cloud unstable to collapse would also be unstable at smaller scales and would therefore be likely to fragment into many lower-mass cores.

The two main competing theoretical extremes to get around this problem are known as the “turbulent core” and “competitive accretion” models. In the former, an additional support mechanism, turbulence, prevents fragmentation in massive cores, allowing a single core with $M > M_J(\text{thermal})$ to form into a single stellar system. By contrast, the competitive accretion model, in its most extreme form, asserts that all stars start their lives as $\sim M_J$ cores which exist within a

collapsing cloud. They are then able to accrete additional material from the cloud and grow from their minimum mass to fill the initial mass function (see Section ??).

Neither theory is presently able to account for feedback from the formed stars. Massive stars drastically affect their environment when they turn on, which can be long before they are done accreting. Massive stars probably go through phases similar to low-mass stars, but they may look quite different. They are likely to ignite fusion while still accreting within a dense core; feedback will begin while most of the mass that will eventually reach the star is still in the ‘core’ phase.

If this happens, the massive star will begin to illuminate a hypercompact H II region, in which the extremely high surrounding densities trap the ionizing radiation. Over time, the star’s luminosity will grow and the surrounding density decrease, either by accreting or being ejected, and the H II region will expand, going through an ultracompact (UC) H II phase before ending as a diffuse H II region.

Understanding these early phases is important for understand what sets a star’s final mass. In a core accretion model, $\sim 2/3$ of the gas in the original ‘core’ may accrete, and the other $\sim 1/3$ blow out, but the mass of the star should be very near the core mass. In the competitive accretion model, the core mass may have little influence on the final star mass, as most of the stellar mass will be Bondi-Hoyle accreted from the surrounding medium.

In order for Bondi-Hoyle (BH) accretion to be effective, though, the surrounding ‘clump’ medium must have a very high density. The BH accretion rate is strongly dependent on the mass of the accreting star and the sound speed of the gas:

$$\dot{M}_{BH} = \frac{4\pi\rho G^2 M^2}{c_s^3}$$

For a low-mass star in a low-density medium and a high-mass star in a high-density medium, the values are

$$\begin{aligned}\dot{M}_{BH} &= 1.6 \times 10^{-7} \left(\frac{M}{M_\odot} \right)^2 \left(\frac{n}{10^4 \text{cm}^{-3}} \right) \left(\frac{c_s}{1 \text{kms}^{-1}} \right)^{-3} M_\odot \text{yr}^{-1} \\ \dot{M}_{BH} &= 1.6 \times 10^{-4} \left(\frac{M}{10M_\odot} \right)^2 \left(\frac{n}{10^5 \text{cm}^{-3}} \right) \left(\frac{c_s}{1 \text{kms}^{-1}} \right)^{-3} M_\odot \text{yr}^{-1}\end{aligned}$$

The timescale for a $10M_{\odot}$ star to double its mass in a $n \sim 10^5 \text{ cm}^{-3}$ medium is ~ 50 kyr, but drops to only 5 kyr for density $n \sim 10^6 \text{ cm}^{-3}$. It is therefore crucial that we measure the density of the bulk of the gas around massive stars - the mass and density of the surrounding medium are essential parameters for determining whether competitive accretion is a viable model for growing massive stars.

Throughout the thesis, I examine the local gas density on parsec scales via line ratios and simpler column-density based estimates. I also examine tracers of infall and outflow to determine accretion properties of forming stars.

1.2.2 Turbulence

Turbulence is one of the defining features of the interstellar medium. Turbulence is thought to govern many properties of the ISM, rendering it scale-free and defining the distribution of velocities, densities, temperatures, and magnetic fields in the gas between stars.

Turbulence forms in fluids when the inertial force greatly exceeds the viscosity. It creates instabilities in the fluid that start on large scales and “cascade” energy to smaller scales. Once a small enough size-scale is reached, the viscosity exceeds the inertial force and the energy heats the fluid on local scales.

Turbulence is most easily modeled by a Kolmogorov spectrum, in which $\Delta v \propto \ell^{1/3}$, i.e. the typical velocity dispersion is greatest at the largest size scales. Kolmogorov turbulence strictly only describes incompressible fluids without magnetic fields, while the ISM is compressible and threaded by magnetic fields. Nonetheless, Kolmogorov turbulence is nearly consistent with some observed properties of the ISM. The Larson size-linewidth relation ($\sigma_{\text{km s}^{-1}} \approx 1.1 L_{pc}^{0.38}$), in particular, is similar to that predicted by Kolmogorov turbulence.

Turbulence is often quoted as a source of **pressure** based on the Kolmogorov description. At size scales much smaller than the driving scale of the turbulence (the “box size” in a simulation), turbulence becomes isotropic and can add support against gravitational collapse.

However, turbulence decays rapidly. The turbulent decay timescale $\tau_{decay} \propto \ell/v$, where ℓ

is the turbulent length scale and v is the velocity scale. It therefore increases with size scale as $\tau_{decay} \propto \ell^{2/3}$. Turbulence decays most quickly on the smallest sizescales.

We are therefore left with two conditions: Turbulence must be driven at large scales for turbulence to provide support against gravity², and it must be constantly driven to resupply the turbulence that is transferred to heat on the smallest scales.

Once stars form, however, large-scale driving of turbulence may not be the dominant shaping mechanism for the gas. Outflows from low-mass stars, soft UV from B stars, and ionizing UV and strong winds from OB stars can drive gas motions, disrupting gas or replenishing turbulent energy. Once stars have formed in a cloud, feedback rather than turbulence is likely to govern the future evolution of the cloud.

Because the ISM is compressible, interacting flows within the turbulent medium will result in density enhancements and voids. Many simulation studies have determined that the resulting density distribution, and correspondingly the column-density distribution, should be approximately log-normal. Observational studies agree that in regions not yet significantly affected by gravity, the column-density distribution is log-normal. In regions where stars are actively forming, i.e. regions in which gas self-gravity has affected a significant fraction of the gas, a high-density power-law tail forms.

One theory of star formation holds that the initial mass function of stars is determined entirely by turbulence. In this description, the highest overdensities in the turbulent medium become gravitationally unstable and separate from the turbulent flow as they collapse into protostellar cores. This idea has been a hot topic in the past few years, but it may be an overly simplistic view.

Turbulence is appealing to theorists as it is a difficult problem to address directly with observations, but it may have great predictive power. If turbulence is the dominant governing process of the ISM, then it is possible to derive a reasonably robust star-formation theory based

² Once stars form in a cloud and stellar feedback becomes significant, turbulence can be driven at all scales, but the turbulent support needed to slow or prevent the initial collapse of starless cores cannot be driven by local stars.

on the excursion set theory successfully applied to cosmological structure formation (???).

However, in reality, turbulence is just one of many processes governing the ISM and star formation. Stellar feedback, in the form of radiation, winds, supernovae, and outflows imposes a preferred driving scale on any individual region, and in many cases these processes will happen faster than turbulent processes. The notion of **initial conditions** for star formation, while theoretically appealing, may prove too strong an oversimplification when searching for a complete theory of star formation.

Throughout this thesis, I consider and measure the drivers, effects and properties of turbulence on a few different scales.

In the W5 and IRAS 05358 regions (Chapter ?? and ?), I examined outflows as potential drivers of turbulence. In IRAS 05358, I concluded that the outflows could provide the observed turbulence in the \sim pc-scale ‘clump’, but that the central core had energy dissipation much faster than turbulence could be resupplied. In W5, I rule out protostellar outflows as a significant driver of turbulence.

In Chapter ??, I examine the density probability distribution function (PDF) in giant molecular clouds (GMCs). Because H₂CO is uniquely capable of measuring local volume density, I was able to place interesting constraints on the density PDFs in non-star-forming GMCs, namely that they are unlikely to be the simple log-normal distributions expected from isothermal incompressible turbulence.

1.2.3 Mass Functions

Perhaps the most fundamental goal of star formation studies is to determine the Initial Mass Function (IMF) of stars and what, if anything, causes it to vary. It is also one of the most challenging statistically and observationally.

The IMF defines the probability distribution function of stellar masses at birth, and therefore differs greatly from the present-day stellar mass function that is very strongly affected by stellar death at the highest masses. In order to determine the mass function for the most massive stars,

it is necessary to look at their birth places. These birth places are dusty, dense, and rare.

It remains somewhat unclear whether the IMF is a universal function or is sampled independently for individual clusters. If it is universal, there is a possibility of forming massive stars anywhere stars form. If cluster-dependent, then a massive star must form with a surrounding cluster.

Some groups now claim that the initial mass function is decided in the gas phase by the formation of cores. The Core Mass Function measures the probability distribution function of core masses, where cores are generally identified observationally as column-density peaks in millimeter/submillimeter emission maps. The CMF has a similar functional form to the IMF, but its mean is higher by a factor ~ 3 in local star forming regions, leading to the claim that star formation proceeds from CMF- \gtrsim IMF with 30% efficiency. This idea has recently been explored theoretically by ?) and ?) and observationally by the Herschel Gould's Belt team (??).

Gas clouds follow a mass function that extends up to the largest possible coherent scales, giant molecular clouds with scales $\sim 50 - 100$ pc that are limited by the scale-height of the ISM in Galactic disks. Between ‘cores’ and GMCs, intermediate scale blobs are often called ‘clumps’. The mass function of these clumps has yet to be determined.

The mass function of GMCs was determine from CO emission towards the Galactic plane and in nearby galaxies (e.g., M33) where they can be resolved. The CMF was measured in nearby clouds where $30''$ beams easily resolve ~ 0.1 pc cores. However, clumps are only found in large numbers in the Galactic plane, where distances are uncertain. They cannot be resolved in other galaxies (except by ALMA now).

To understand star formation on a galactic scale, it is necessary to understand the transition from large-scale giant molecular clouds and proto-stellar cores. Clouds follow a shallow mass function, with the largest clouds containing most of the gas. Cores and stars are both drawn from steep mass functions in which most of the mass near some peak in the distribution. Presumably there must be some intermediate state of the gas that is drawn from an intermediate distribution, shallower than ‘cores’ but steeper than ‘clouds’.

The BGPS (Chapter ??) presents the first real opportunity to explore the mass function of clumps on scales intermediate between cores and giant clouds. While I do not explicitly examine core or clump mass functions in this thesis, their measurement is an important motivation for the large-area surveys we have performed.

1.2.3.1 Clusters

Clusters are also drawn from a mass function comparable to stars, but their distribution is better measured than for stars. Clusters are easily visible - and resolvable - in other galaxies, and massive clusters are less likely to be embedded than massive stars. In normal galaxies, cluster populations are consistent with a Schechter distribution: a power-law $\alpha \sim 2$ with an exponential cutoff at large masses.

$$N(M)dM = CM^{-2}e^{-M}dM$$

Since clusters are not drawn from the same parent distribution as GMCs (which have $\alpha \sim 1$, so $N(M)dM = CM^{-1}dM$), it is plausible that their precursors are, instead, the intermediate-scale ‘clumps’ observed in the millimeter continuum. However, the clump mass function has yet to be measured, so even this first step of determining plausibility is incomplete.

Clusters are an important observational tool in astrophysics. For stellar studies, they have been used to select populations of co-eval stars. In extragalactic studies, they are frequently the smallest observable individual units. However, many recent works have pointed out that clusters may be short-lived, transient phenomena (????). Any study of their populations must take in to account their dissolution. The most massive clusters, however, are both the most easily observed and the longest lived, and therefore provide some of the most useful tools for understanding stars.

As with massive stars, massive clusters are rare. Only a handful of young massive clusters are known within our Galaxy, including the most massive, NGC 3603, the Arches cluster, and Westerlund 1 (?). These are the only locations in the galaxy known to be forming multiple stars near the (possible) upper stellar mass limit. Despite their importance, though, only a handful

of these clusters are known and the population of such clusters is effectively unconstrained. The incomplete knowledge of clusters is due to extinction and confusion within the plane.

In Chapter ??, I search the BGPS for candidate proto-massive star clusters. Because the Galactic disk is optically thin at 1.1 mm, a complete census of proto-clusters is possible.

1.3 Outline

This thesis includes 5 chapters. Chapter ?? describes observations of the W5 star-forming region to identify outflows; this chapter is somewhat tangential to the rest. Chapter ?? describes the BGPS data reduction process and data pipeline. Chapter ?? is a Letter identifying massive proto-clusters in the BGPS. Chapter ?? is the pilot study of H₂CO towards previously-known UCHII regions. It includes the methodology and analysis of turbulent properties of Galactic GMCs. Chapter ?? expands upon Chapter ??, detailing the expansion of the H₂CO survey to BGPS-selected sources. Chapter ?? concludes.

Chapter 2

Using outflows to track star formation in the W5 HII region complex

2.1 Preface

Only a few months after arriving at CU, I was given the opportunity to visit the peak of Mauna Kea to perform observations with the JCMT. I spend about 3 weeks at the telescope over the course of two years primarily mapping the W5 complex. A side-project done during these observations resulted in my Comps II project on IRAS 05358+3543. These data were taken using Jonathan Williams' Hawaii time allocation with the HARP receiver. The data were taken with essentially no plan for how they would be used. The paper may have diminished our group's overall interest in the W5 region: it turns out that star formation is probably at its end here, being quenched by massive-star feedback. However, there is a largely ignored cloud to the northwest of the well-studied W5 bubbles that has significant potential to form new stars.

The W5 study was originally intended to include a Bolocam census of cores, but the data in this region turned out to be the most problematic and contained little signal. We acquired additional data in 2009, but never got around to performing a joint analysis of the CO and continuum data. In part, at least, this is because W5 is so faint at millimeter wavelengths compared to many Galactic Plane sources.

This work is essentially a very detailed study of a star-forming region with minimal implications for star forming theories at the moment.

2.2 Introduction

Galactic-scale shocks such as spiral density waves promote the formation of giant molecular clouds (GMCs) where massive stars, star clusters, and OB associations form. The massive stars in such groups can either disrupt the surrounding medium or promote further star formation. While ionizing and soft UV radiation, stellar winds, and eventually supernova explosions destroy clouds in the immediate vicinity of massive stars, as the resulting bubbles age and decelerate, they can also trigger further star formation. In the “collect and collapse” scenario (e.g. ?), gas swept-up by expanding bubbles can collapse into new star-forming clouds. In the “radiation-driven implosion” model (??), pre-existing clouds may be compressed by photo-ablation pressure or by the increased pressure as they are overrun by an expanding shell. In some circumstances, forming stars are simply exposed as low-density gas is removed by winds and radiation from massive stars. These processes may play significant roles in determining the efficiency of star formation in clustered environments (?).

Feedback from low mass stars may also control the shape of the stellar initial mass function in clusters (??). Low mass young stars generate high velocity, collimated outflows that contribute to the turbulent support of a gas clump, preventing the clump from forming stars long enough that it is eventually blown away by massive star feedback. It is therefore important to understand the strength of low-mass protostellar feedback relative to other feedback mechanisms.

Outflows are a ubiquitous indicator of the presence of ongoing star formation (?). CO outflows are an indicator of ongoing embedded star formation at a younger stage than optical outflows because shielding from the interstellar radiation field is required for CO to survive. Although Herbig- Haro shocks and H₂ knots reveal the locations of the highest-velocity segments of these outflows, CO has typically been thought of as a “calorimeter” measuring the majority of the mass and momentum ejected from protostars or swept up by the ejecta (?).

The W5 star forming complex in the outer galaxy is a prime location to study massive star formation and triggering. The bright-rimmed clouds in W5 have been recognized as good candidates

for ongoing triggering by a number of groups (??). The clustering properties were analyzed by ?) using Spitzer infrared data, and a number of significant clusters were discovered. The whole W5 complex may be a product of triggering, as it is located on one side of the W4 chimney thought to be created by multiple supernovae during the last ~ 10 MYr (?), Figure ??).

Following ?), we adopt a distance to W5 of 2 kpc based on the water-maser parallax distance to the neighboring W3(OH) region (?). As with W3, the W5 cloud is substantially ($\approx 1.5 \times$) closer than its kinematic distance would suggest ($v_{LSR}(-40 \text{ km s}^{-1}) \approx 3 \text{ kpc}$). Given this distance, ?) derived a total gas mass of $6.5 \times 10^4 M_\odot$ from a $2 \mu\text{m}$ extinction map.

The W5 complex was mapped in the ^{12}CO 1-0 emission line by the Five College Radio Astronomy Observatory (FCRAO) using the SEQUOIA receiver array (?). The same array was used to map W5 in the ^{13}CO 1-0 line (C. Brunt, private communication). Some early work searched for outflows in W5 (?), but the low-resolution CO 1-0 data only revealed a few, and only one was published. The higher resolution and sensitivity observations presented here reveal many additional outflows.

While W5 is thought to be associated with the W3/4/5 complex, there are other infrared sources in the same part of the sky that are not obviously associated with W5. Some of these have been noted to be in the outer arm (several kpc behind W5) by ?) and ?).

In section 2, we present the new and archival data used in our study. In section 3, we discuss the outflow detection process and compare outflow detectability in W5 to that in Perseus. In section 4, we discuss the physical properties of the outflows and their implications for star formation in the W5 complex. In section 5, we briefly describe the outer-arm outflows discovered.

2.3 OBSERVATIONS

2.3.1 JCMT HARP CO 3-2

CO J=3-2 345.79599 GHz data were acquired at the 15 m James Clerk Maxwell Telescope (JCMT) using the HARP array on a series of observing runs in 2008. On 2-4 January, 2008,

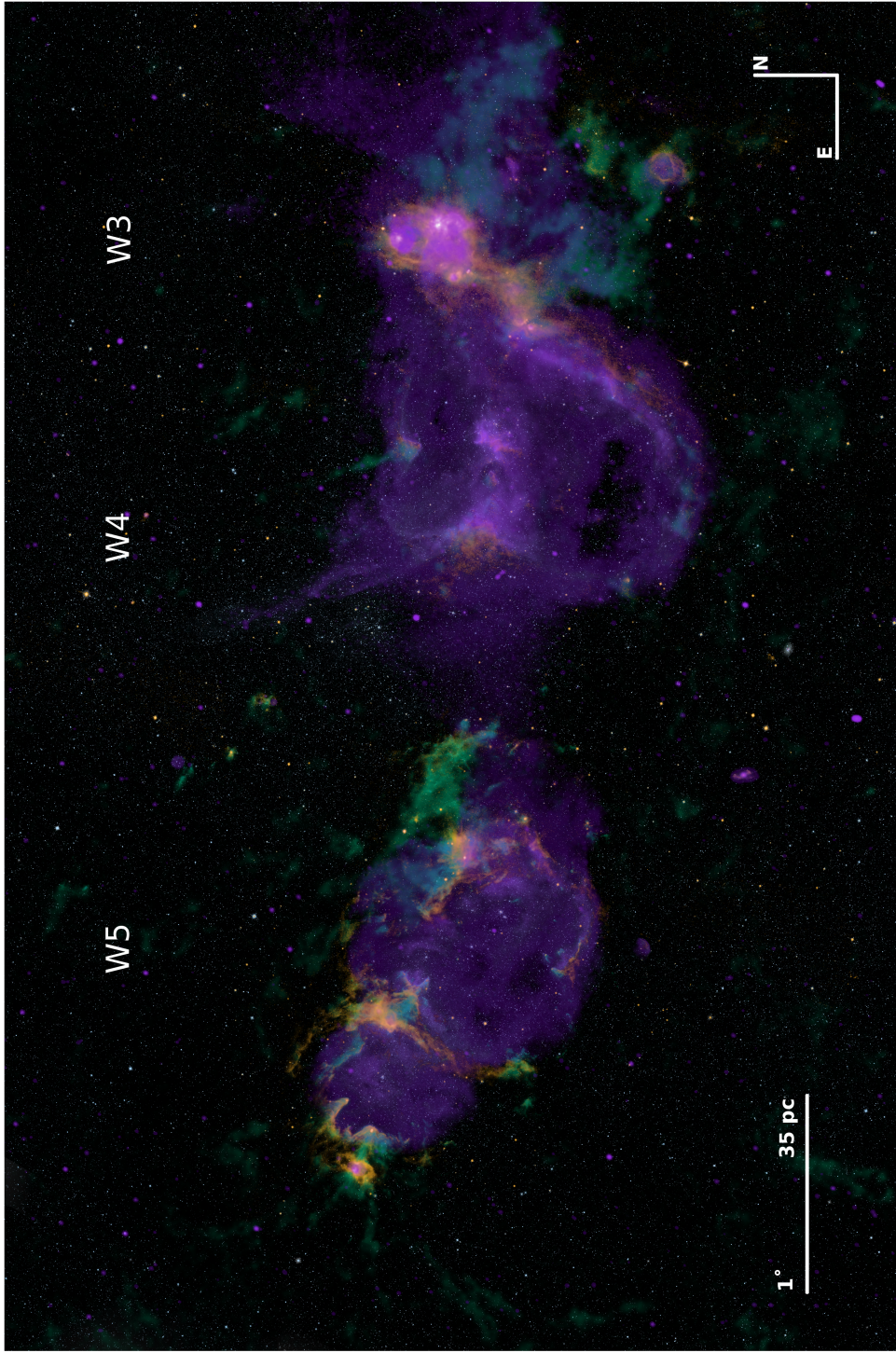


Figure 2.1 An overview of the W3/4/5 complex (also known as the “Heart and Soul Nebula”) in false color. Orange shows $8 \mu\text{m}$ emission from the Spitzer and MSX satellites. Purple shows 21 cm continuum emission from the DRAO CGPS (?); the DSS R image was used to set the display opacity of the 21 cm continuum as displayed (purely for aesthetic purposes). The green shows JCMT ^{12}CO 3-2 along with FCRAO ^{12}CO 1-0 to fill in gaps that were not observed with the JCMT. The image spans $\sim 7^\circ$ in galactic longitude. This overview image shows the hypothesized interaction between the W4 superbubble and the W3 and W5 star-forming regions (?).

~ 800 square arcminutes were mapped. During the run, τ_{225} , the zenith opacity at 225 GHz measured using the Caltech Submillimeter Observatory tipping radiometer, ranged from 0.1 to 0.4 ($0.4 < \tau_{345\text{GHz}} < 1.6^1$). Additional areas were mapped on 4-7 August, 16-20 and 31 October, and 1 and 12-15 Nov 2008 in similar conditions. A total of ~ 3 square degrees (12000 arcmin 2) in the W5 complex were mapped (a velocity-integrated mosaic is shown in Figure ??).

HARP is a 16 pixel SIS receiver array acting as a front-end to the ACSIS digital auto-correlation spectrometer. In January 2008, 14 of the 16 detectors were functional. In the 2nd half of 2008, 12 of 16 were functional, necessitating longer scans to achieve similar S/N.

In January 2008, a single spectral window centered at 345.7959899 with bandwidth 1.0 GHz and channel width 488 kHz (0.42 km s $^{-1}$) was used. In August 2008 and later, we used 250 MHz bandwidth and 61 kHz (0.05 km s $^{-1}$) channel width. At this frequency, the beam FWHM is 14'' (0.14 pc at a distance of 2 kpc) 2 .

A raster mapping strategy was used. In 2008, the array was shifted by 1/2 of an array spacing (58.2'') between scans. Data was sampled at a rate of 0.6s per integration. Two perpendicular scans were used for each field observed. Most fields were 10 \times 10' and took ~ 45 minutes. When only 12 receptors were available, 1/4 array stepping (29.1'') was used with a sample rate of 0.4s per integration.

Data were reduced using the SMURF package within the STARLINK software distribution 3 . The SMURF command MAKECUBE was used to generate mosaics of contiguous sub-fields. The data were gridded on to cubes with 6'' pixels and smoothed with a $\sigma = 2$ -pixel gaussian, resulting in a map FWHM resolution of 18'' (0.17 pc). A linear fit was subtracted from each spectrum over emission-free velocities (generally -60 to -50 and -20 to -10 km s $^{-1}$) to remove the baseline. The final map RMS was $\sigma_{T_A^*} \sim 0.06 - 0.11K$ in 0.42 km s $^{-1}$ channels.

The sky reference position (off position) in January 2008 was J2000 2:31:04.069 +62:59:13.81. In later epochs, off positions closer to the target fields were selected from blank sky regions identified

¹ <http://docs.jach.hawaii.edu/JCMT/SCD/SN/002.2/node5.html>

² http://docs.jach.hawaii.edu/JCMT/OVERVIEW/tel_overview/

³ <http://starlink.jach.hawaii.edu/>

in January 2008 in order to increase observing efficiency. A main-beam efficiency $\eta_{mb} = 0.60$ was used as per the JCMT website to convert measurements to T_{mb} , though maps and spectra are presented in the original T_A^* units.

2.3.2 FCRAO Outer Galaxy Survey

The FCRAO Outer Galaxy Survey (OGS) observed the W5 complex in ^{12}CO (?) and ^{13}CO 1-0 (C. Brunt, private communication). The ^{13}CO data cube achieved a mean sensitivity of 0.35 K per 0.13 km s^{-1} channel, or 0.6 K km s^{-1} integrated. The ^{13}CO cube was integrated over all velocities and resampled to match the BGPS map using the MONTAGE⁴ package. The FWHM beam size was $\theta_B = 50''$ (0.48 pc). The integrated ^{12}CO data cube, with a sensitivity $\sigma = 1K \text{ km s}^{-1}$, is displayed with region name identifications in Figure ??.

2.3.3 Spitzer

Spitzer IRAC and MIPS $24 \mu\text{m}$ images from ?) were used for morphological comparison. The reduction and extraction techniques are detailed in their paper.

2.4 Analysis

2.4.1 Outflow Detections

Outflows were identified in the CO data cubes by manually searching through position-velocity space for line wings using STARLINK's GAIA display software. Outflow candidates were identified by high velocity wings inconsistent with the local cloud velocity distribution, which ranged from a width of 3 km s^{-1} to 7 km s^{-1} . Once an outflow candidate was identified in the position-velocity diagrams, the velocity range over which the wing showed emission in the position-velocity diagram (down to $T_A^* = 0$) was integrated over to create a map from which the approximate outflow size and position was determined (e.g. Figures ?? and ??).

⁴ <http://montage.ipac.caltech.edu/>

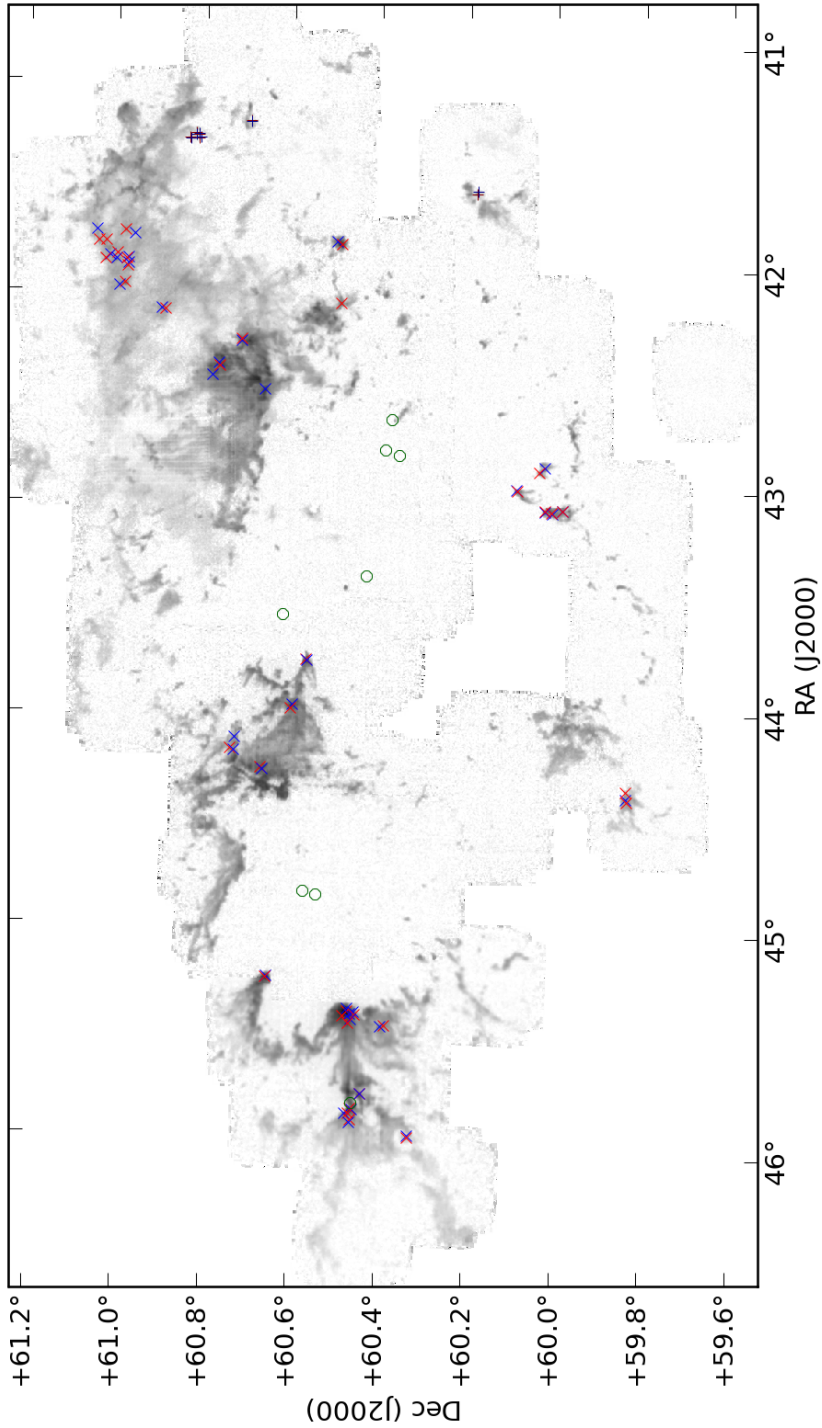


Figure 2.2 A mosaic of the CO 3-2 data cube integrated from -20 to -60 km s^{-1} . The grayscale is linear from 0 to 150 K km s^{-1} . The red and blue X's mark the locations of redshifted and blueshifted outflows. Dark red and dark blue plus symbols mark outflows at outer arm velocities. Green circles mark the location of all known B0 and earlier stars in the W5 region from SIMBAD.

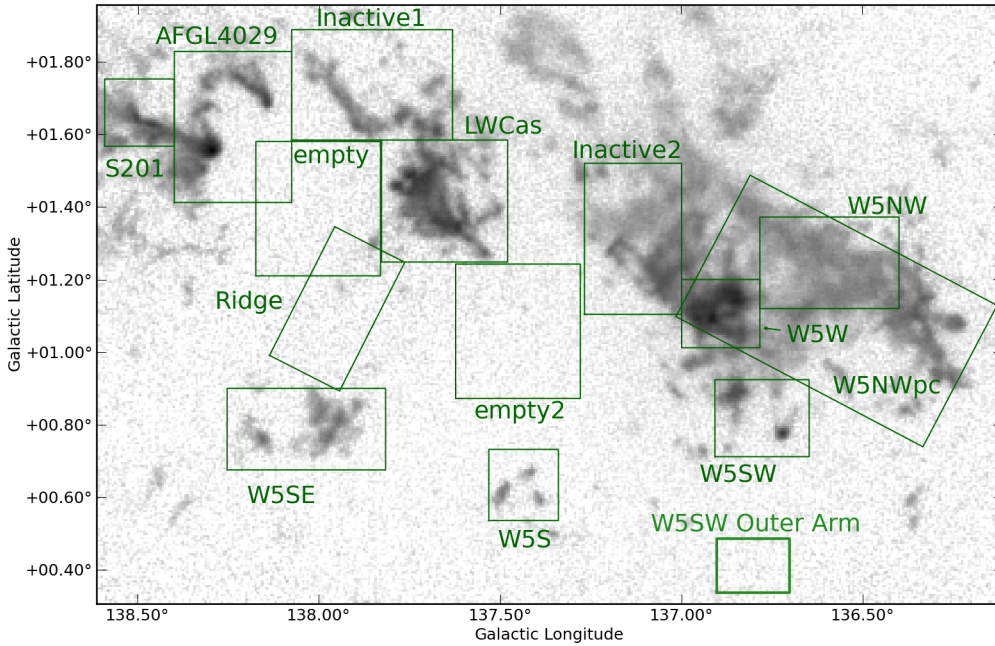


Figure 2.3 Individual region masks overlaid on the FCRAO ^{12}CO integrated image. The named regions, S201, AFGL4029, LWCas, W5NW, W5W, W5SE, W5S, and W5SW, were all selected based on the presence of outflows within the box. The inactive regions were selected from regions with substantial CO emission but without outflows. The ‘empty’ regions have essentially no CO emission within them and are used to place limits on the molecular gas within the east and west ‘bubbles’. W5NWpc is compared directly to the Perseus molecular cloud in Section ??

Unlike ?) and ?), we did not use an ‘objective’ outflow identification method because of the greater velocity complexity and poorer spatial resolution of our observations. The outflow selection criteria in these papers requires the presence of a sub-mm clump in order to identify a candidate driving source (and therefore a targeted region in which to search for outflows), making a similar objective identification impossible for our survey. As discussed later in Section ??, the regions associated with outflows have wide lines and many are double-peaked. Additionally, many smaller areas associated with outflows have collections of gaussian-profiled clumps that are not connected to the cloud in position-velocity diagrams but are not outflows. In particular, W5 is pockmarked by dozens of small cometary globules that are sometimes spatially coincident with the clouds but slightly offset in velocity.

While ?) described the benefits of 3D visualization using isosurface contours, we found that the varying signal-to-noise across large-scale (~ 500 pixel 2) regions with significant extent in RA/Dec and limited velocity dynamic range made this method difficult for W5. There were many low-intensity outflows that were detectable by careful searches through position-velocity space that are not as apparent using isosurface methods. Out of the 55 outflows reported here, only 14 ⁵ would be considered obvious, high-intensity, high-velocity flows from their spectra alone; the rest could not be unambiguously detected without a search through position-velocity space.

In the majority of sources, the individual outflow lobes were unresolved, although some showed hints of position-velocity gradients at low significance and in many the red and blue flows are spatially separated. Only Outflow 1’s lobes were clearly resolved (Figure ??). Some of most suggestive gradients occurred where the outflow merged with its host molecular cloud in position-velocity space, making the gradient difficult to distinguish (e.g., Outflow 12, Figure ??). Bipolar pairs were selected when there were red and blue flows close to one another. The classification of a bipolar flow was either ‘yc’ (yes - confident), ‘yu’ (yes - unconfident), or ‘n’ (no) in Table ???. This identification is discussed in the captions for each outflow figure in the online supplement. The

⁵ Outflows 15, 20, 24, the cluster of outflows 26-32, 47, 48, 52, and 53 could all have readily been detected by pointed single-dish measurements.

AFGL 4029 region has many red and blue lobes but confusion prevented pairing.

In cases where only the red- or blue-shifted lobe was visible, the surrounding pixels were searched for lower-significance and lower-velocity counterparts. For cases in which emission was detected, a candidate counterflow was identified and incorporated into the catalog. However, in 12 cases, the counterflow still evaded detection, either because of confusion or because the counterflow is not present in CO.

The outflow positions are overlaid on the CO 3-2 image in Figure ?? to provide an overview of where star formation is most active. The figures in Section ?? show outflow locations overlaid on small-scale images.

Because our detection method involved searching for high-velocity outflows by eye, there should be no false detections. However, it is possible that some of these outflows are generated by mechanisms other than protostellar jets and winds since we have not identified their driving sources.

One possible alternative driving mechanism is a photoevaporation flow, which could be accelerated up to the sound speed of the ionized medium, $c_{II} \approx 10 \text{ km s}^{-1}$. Gas accelerating away from the cloud would not be detected as an outflow because it would be rapidly ionized. However, gas driven inward would be accelerated and remain molecular. It could exhibit red and / or blue flows depending on the line of sight orientation. While there are viable candidates for this form of outflow impersonator, such flows can only have peak velocities $v \lesssim c_{II}/4 \approx 2.5 \text{ km s}^{-1}$ in the strong adiabatic shock limit, so that any gas seen with higher velocity tails are unlikely to be radiation-driven.

Another plausible outflow impostor is the high-velocity tail in a turbulent distribution. However, for a typical molecular cloud, the low temperatures would require very high mach-number shocks ($\mathcal{M} \gtrsim 10$ assuming $T_{cloud} \sim 20 \text{ K}$ and $v_{flow} \sim 3 \text{ km s}^{-1}$) that in idealized turbulence should be rare and short-lived. It is not known how frequent such high-velocity excursions will be in non-ideal turbulence with gravity (A. Goodman, P. Padoan, private communication). Finally, it is less likely for turbulent intermittency to have nearly coincident red and blue lobes, so intermittency

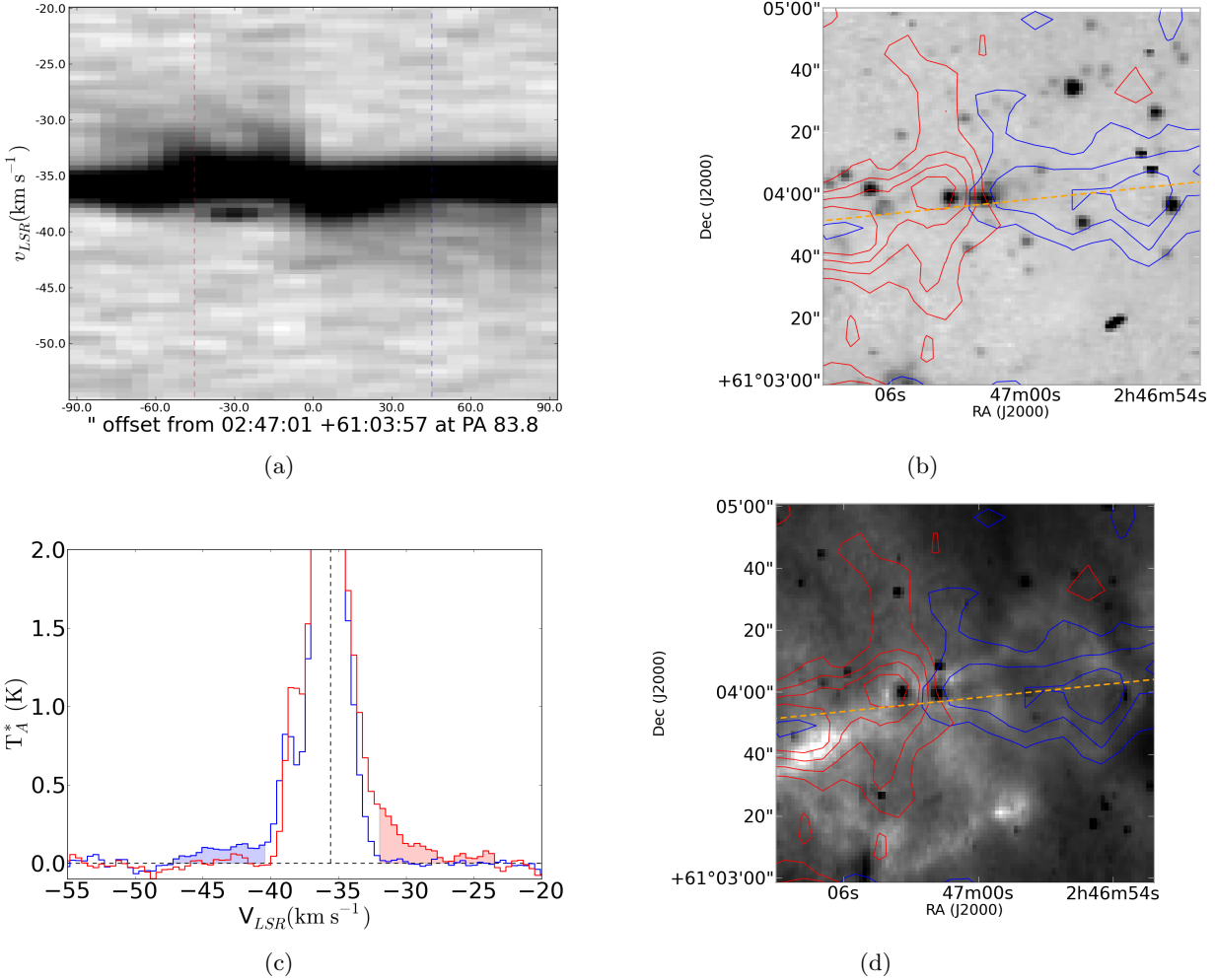


Figure 2.4 Position-velocity diagrams (a), spectra (c), and contour overlays of Outflow 1 on Spitzer 4.5 μ m (b) and 8 μ m (d) images. This outflow is clearly resolved and bipolar. (a): Position-velocity diagram of the blue flow displayed in arcsinh stretch from $T_A^* = 0$ to 3 K. Locations of the red and blue flows are indicated by vertical dashed lines. The location of the position-velocity cut is indicated by the orange dashed line in panels (b) and (d), although the position-velocity cut is longer than those cut-out images. (b) Spitzer 4.5 μ m image displayed in logarithmic stretch from 30 to 500 MJy sr $^{-1}$. (c): Spectrum of the outflow integrated over the outflow aperture and the velocity range specified with shading. The velocity center (vertical dashed line) is determined by fitting a gaussian to the ^{13}CO spectrum in an aperture including both outflow lobes. In the few cases in which ^{13}CO 1-0 was unavailable, a gaussian was fit to the ^{12}CO 3-2 spectrum. (d): Contours of the red and blue outflows superposed on the Spitzer 8 μ m image displayed in logarithmic stretch. The contours are generated from a total intensity image integrated over the outflow velocities indicated in panel (c). The contours in both panels (b) and (d) are displayed at levels of 0.5, 1, 1.5, 2, 3, 4, 5, 6 K km s $^{-1}$ ($\sigma \approx 0.25$ K km s $^{-1}$). The contour levels and stretches specified in this caption apply to all of the figures in the supplementary materials except where otherwise noted.

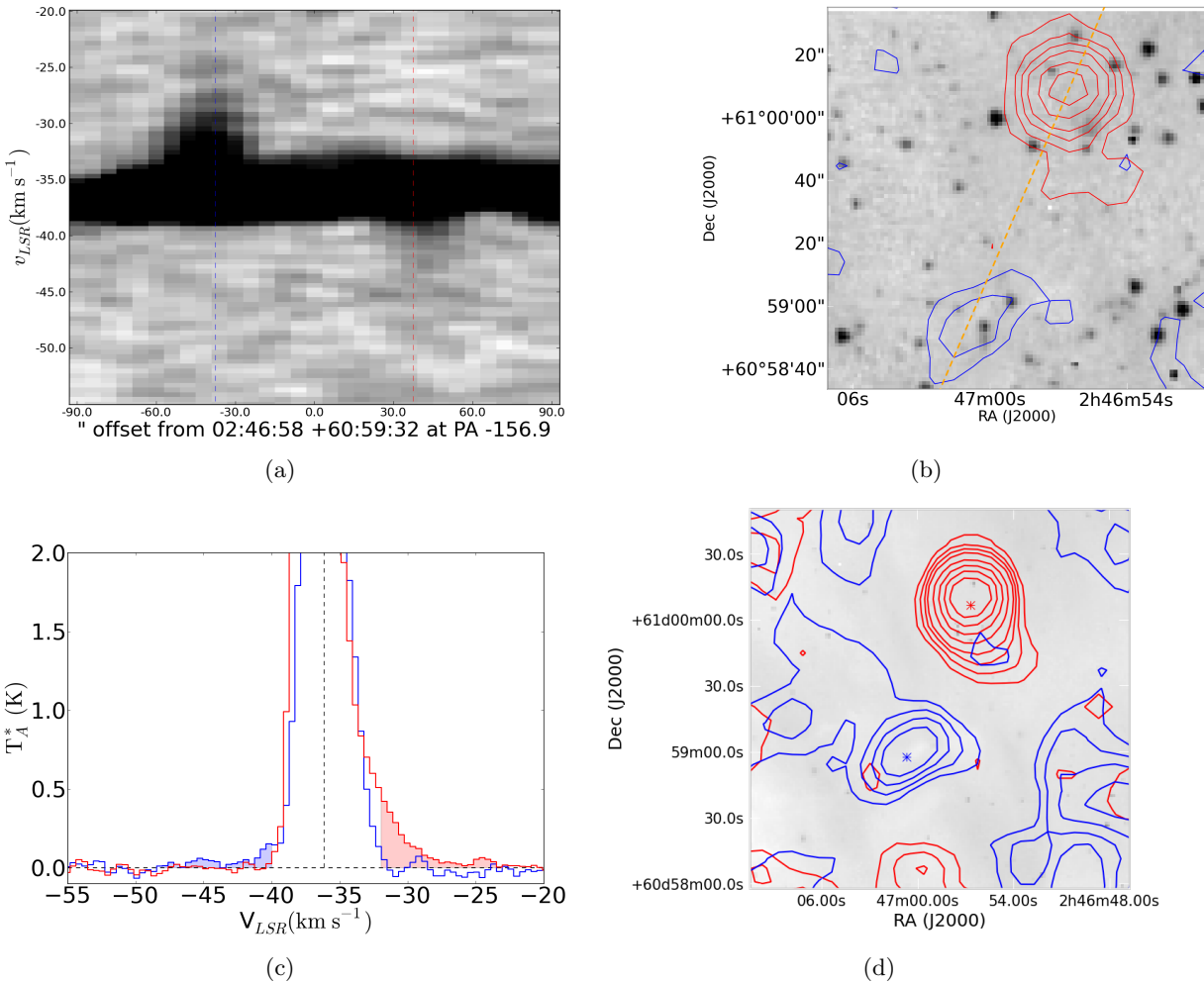


Figure 2.5 Position-velocity diagram, spectra, and contour overlays of Outflow 2 (see Figure ?? for a complete description). While the two lobes are widely separated, there are no nearby lobes that could lead to confusion, so we regard this pair as a reliable bipolar outflow identification.

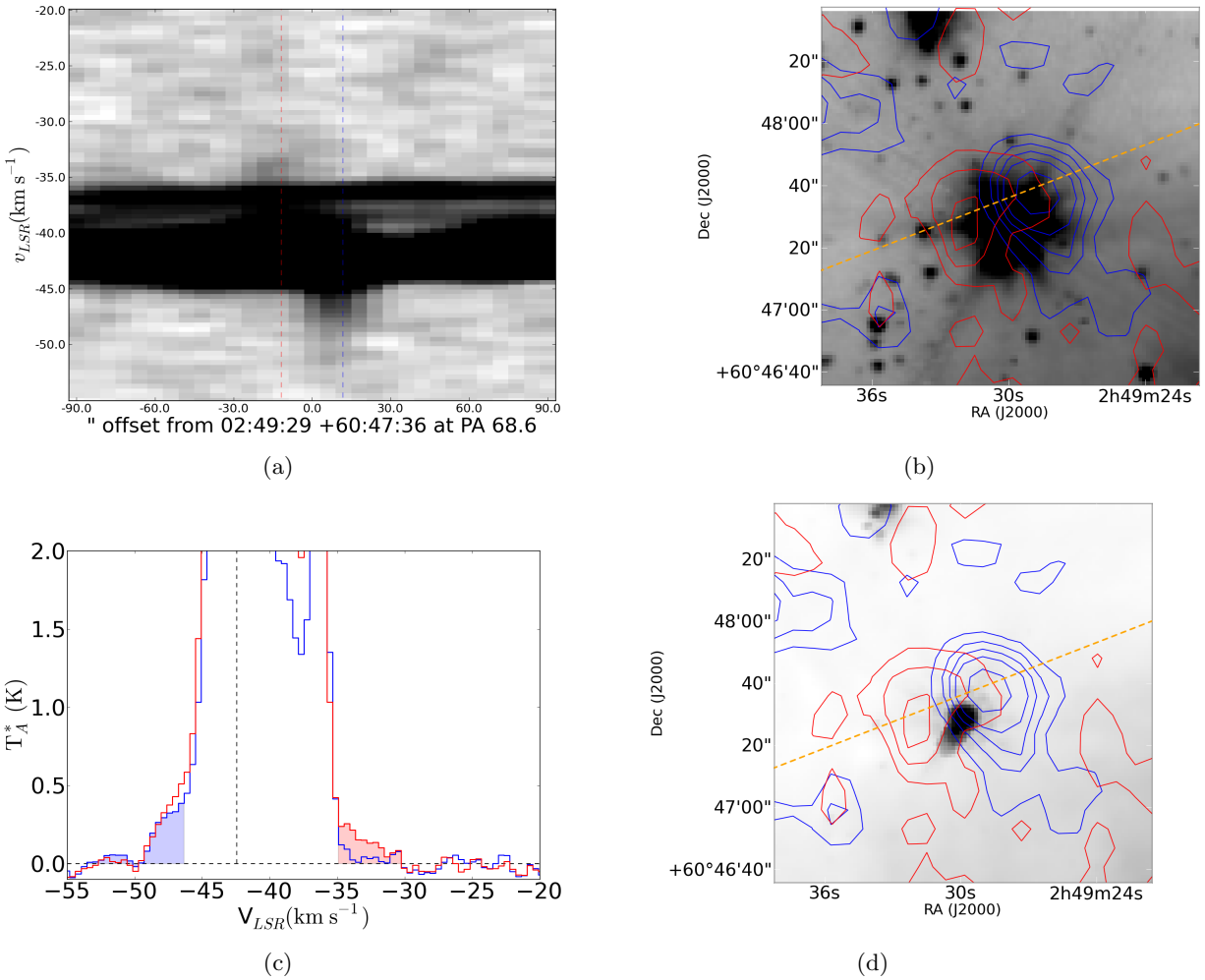


Figure 2.6 Position-velocity diagram, spectra, and contour overlays of Outflow 12. Much of the red outflow is lost in the complex velocity profile of the molecular cloud(s), but it is high enough velocity to still be distinguished.

can be morphologically excluded in most cases.

2.4.1.1 Comparison to Perseus CO 3-2 observations

We used the HARP CO 3-2 cubes from ?) to evaluate our ability to identify outflows. We selected an outflow that was well-resolved and unconfused, L1448, and evaluated it at both the native sensitivity of the ?) observations and degraded in resolution and sensitivity to match our own. We focus on L1448 IRS2, labeled Outflow 30 in ?). Figure ?? shows a comparison between the original quality and degraded data.

Integrating over the outflow velocity range, we measure each lobe to be about $1.6' \times 0.8'$ (0.14×0.07 pc). Assuming a distance to Perseus of 250 pc (e.g. ?), we smooth by a factor of 8 by convolving the cube with a $\text{FWHM} = 111''$ gaussian, then downsample by the same factor of 8 to achieve $6''$ square pixels at 2 kpc. The resulting noise was reduced because of the spatial and spectral smoothing and was measured to be ≈ 0.05 K in 0.54 km s^{-1} channels, which is comparable to the sensitivity in our survey. It is still possible to distinguish the outflows from the cloud in position-velocity space. Each lobe is individually unresolved (long axis $\sim 12''$ compared to our beam FWHM of $18''$), but the two are separated by $\gtrsim 20''$ and therefore an overall spatial separation can still be measured. Because they are just barely unresolved at this distance, the lobes' surface brightnesses are approximately the same at 2 kpc as at 250 pc; if this outflow were seen at a greater distance it would appear fainter.

?) detected 4 outflows within this map, plus an additional confused candidate. We note an additional grouping of outflowing material in the north-middle of the map (centered on coordinate 150×150 in Figure ??). In the smoothed version, only three outflows are detected in the blue and two in the red, making flow-counterflow association difficult. The north-central blueshifted component appears to be the counterpart of the red flow when smoothed, although it is clearly the counterpart of the northwest blue flow in the full-resolution image.

We are therefore able to detect any outflows comparable to L1448 (assuming a favorable geometry), but are likely to see clustered outflows as single or possibly extended lobes and will

count fewer lobes than would be detected at higher resolution. Additionally, it is clear from this example that two adjacent outflows with opposite polarity are not necessarily associated, and therefore the outflows' source(s) may not be between the two lobes.

In order to determine overall detectability of outflows compared to Perseus, we compare to ?) in Figure ???. Out of 29 outflows in their survey with measured ‘lobe lengths’, 22 (71%) were smaller than $128''$ which would be below our $18''$ resolution if observed at 2 kpc. Even the largest lobes (HRF26R, HRF28R, HRF44B) would only extend $\sim 60''$ at 2 kpc. Each lobe in the largest outflow in our survey, Outflow 1, is $\sim 80''$ ($660''$ at 250pc), but no other individual outflow lobes in W5 are clearly resolved. However, as seen in Figure ???, many bipolar lobes are **separated** by more than the telescope resolution, and the overall lobe separation distribution (as opposed to the lobe length, which is mostly unmeasured in our sample) in W5 is quite similar to the separation distribution in Perseus. The 2-sample KS test gives a 25% probability that they are drawn from the same distribution (the null hypothesis that they are drawn from the same distribution cannot be rejected).

On average, the ?) outflow velocities are similar to ours (Figure ??). We detect lower velocity outflows because we do not set a strict lower velocity limit criterion. We do not detect the highest velocity outflows most likely because of our poorer sensitivity to the faint high-velocity tips of outflows, although it is also possible that no high-velocity ($v > 20 \text{ km s}^{-1}$) flows exist in the W5 region. Note that the histogram compares quantities that are not directly equivalent: the outflows in ?) and our own data are measured out to the point at which the outflow signal is lost, while the ‘region’ velocities are full-width half-max (FWHM) velocities.

Finally, we use the detectability of outflows in Perseus to inform our expectations in W5. Since it appears that we can detect outflows from low-mass protostars with sub-stellar to $\sim 30L_\odot$ luminosities at the distance of W5 and these objects should be the most numerous in a standard initial mass function, the distribution of physical properties in W5 outflows should be similar to those in Perseus. However, because W5 is a somewhat more massive cloud ($M_{W5} \approx 5M_{\text{Perseus}}$

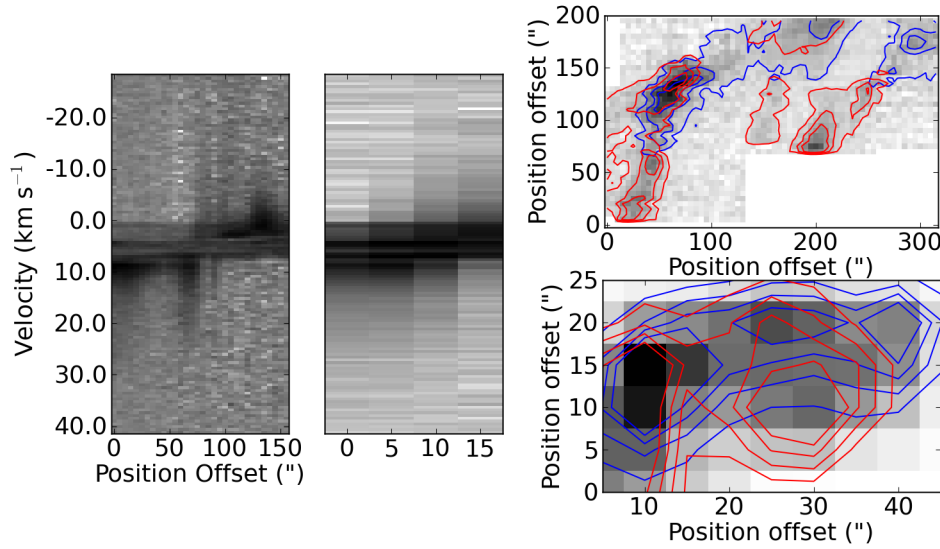


Figure 2.7 Comparison of L1448 seen at a distance of 250 pc (left) versus 2 kpc (middle) with sensitivity 0.5 K and 0.05K per 0.5 km s^{-1} channel respectively. *Far Left:* Position-velocity diagram (log scale) of the outflow L1448 IRS2 at its native resolution and velocity. L1448 IRS2 is the rightmost outflow in the contour plots. The PV diagram is rotated 45° from RA/Dec axes to go along the outflow axis. *Middle Left:* Position-velocity diagram (log scale) of the same outflow smoothed and rebinned to be eight times more distant. *Top Right:* The integrated map is displayed at its native resolution (linear scale). The red contours are of the same data integrated from 6.5 to 16 km s^{-1} and the blue from -6 to 0 km s^{-1} . Contours are at 1,3, and 5 K km s^{-1} ($\sim 6, 18, 30\sigma$). Axes are offsets in arcseconds. Because we are only examining the relative detectability of outflows at two distances, we are not concerned with absolute coordinates. *Bottom Right:* The same map as it would be observed at eight times greater distance. Axes are offsets in arcseconds assuming the greater distance. Contours are integrated over the same velocity range as above, but are displayed at levels 0.25,0.50,0.75,1.00 K km s^{-1} ($\sim 12, 24, 48, 60\sigma$). The entire region is detected at high significance, but dominated by confusion. It is still evident that the red and blue lobes are distinct, but they are each unresolved.

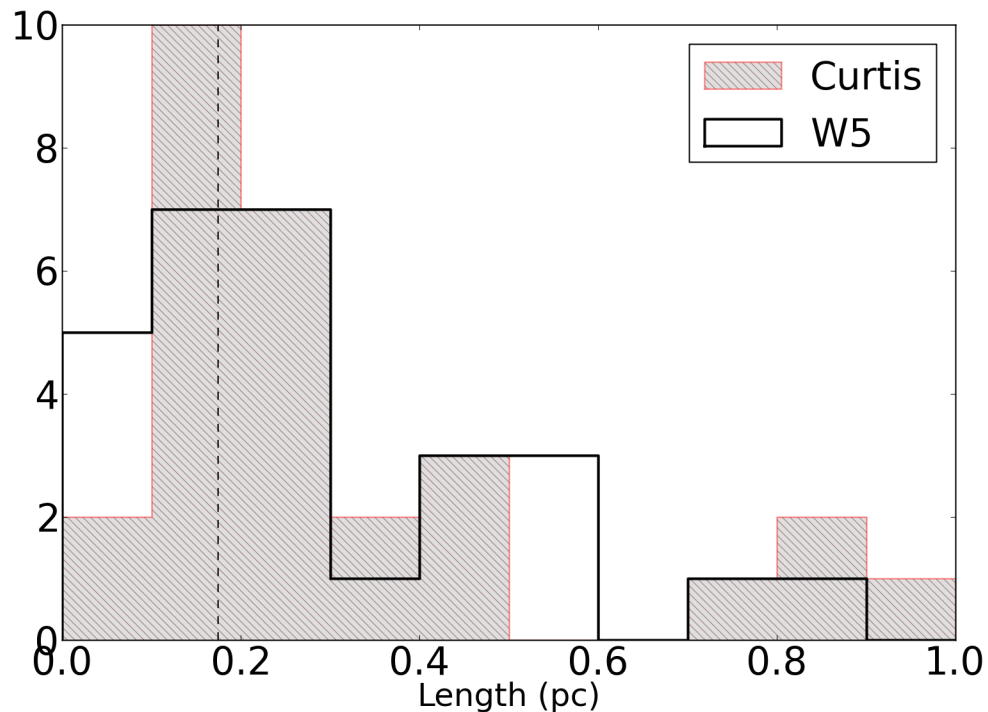


Figure 2.8 Histogram of the measured outflow lobe separations. The grey hatched region shows ? values. The vertical dashed line represents the spatial resolution of our survey. The two distributions are similar.

⁶), we might expect the high-end of the distribution to extend to higher values of outflow mass, momentum, and energy. Since we will likely see clustered outflows confused into a smaller number of distinct lobes, we expect a bias towards higher values of the derived quantities but a lower detection rate.

2.4.1.2 Velocity, Column Density, and Mass Measurements

Throughout this section, we assume that the CO lines are optically thin and thermally excited. The measured properties are presented in Table ???. These assumptions are likely to be invalid, so we also discuss the consequences of applying ‘typical’ optical depth corrections to the derived quantities. Because we do not measure optical depths and the optical depth correction for CO 3-2 is less well quantified than for CO 1-0 (??)⁷ , we only present the uncorrected measurements in Table ??.

The outflow velocity ranges were measured by examining both RA-velocity and Dec-velocity diagrams interactively using the STARLINK GAIA data cube viewing tool. The velocity limits are set to include all outflow emission that is distinguishable from the cloud (i.e. the velocity at which outflow lobes dominate over the gaussian wing of the cloud emission) down to zero emission. An outflow size (or lobe size, following ?) was determined by integrating over the blue and red velocity ranges and creating an elliptical aperture to include both peaks; the position and size therefore have approximately beam-sized ($\approx 18''$) accuracy. The integrated outflow maps are shown as red and blue contours in Figure ???. The velocity center was computed by fitting a gaussian to the FCRAO ^{13}CO spectrum averaged over the elliptical aperture.

The column density is estimated from ^{12}CO J=3-2 assuming local thermal equilibrium (LTE) and optically thin emission using the equation $N(\text{H}_2) = 5.3 \times 10^{18} \eta_{mb}^{-1} \int T_A^*(v) dv$ for $T_{ex} = 20$ K. The derivation is given in the Appendix. The column density in the lobes is likely to be dominated

⁶ M_{W5} is estimated from ^{13}CO . We also estimate the total molecular mass in W5 using the X-factor and acquire $M_{W5} = 5.0 \times 10^4 M_\odot$, in agreement with ?), who estimated a molecular mass of 4.4×10^4 from ^{12}CO using the same X-factor. ?) estimated a total gas mass of 6.5×10^4 from a 2MASS extinction map. The total molecular mass in Perseus is $M_{Perseus} \sim 10^4$ (?)

⁷ In ?), this correction factor ranged from 1.8 to 14.3; ?) did not enumerate the optical depth correction they used but it is typically around 7 (?).

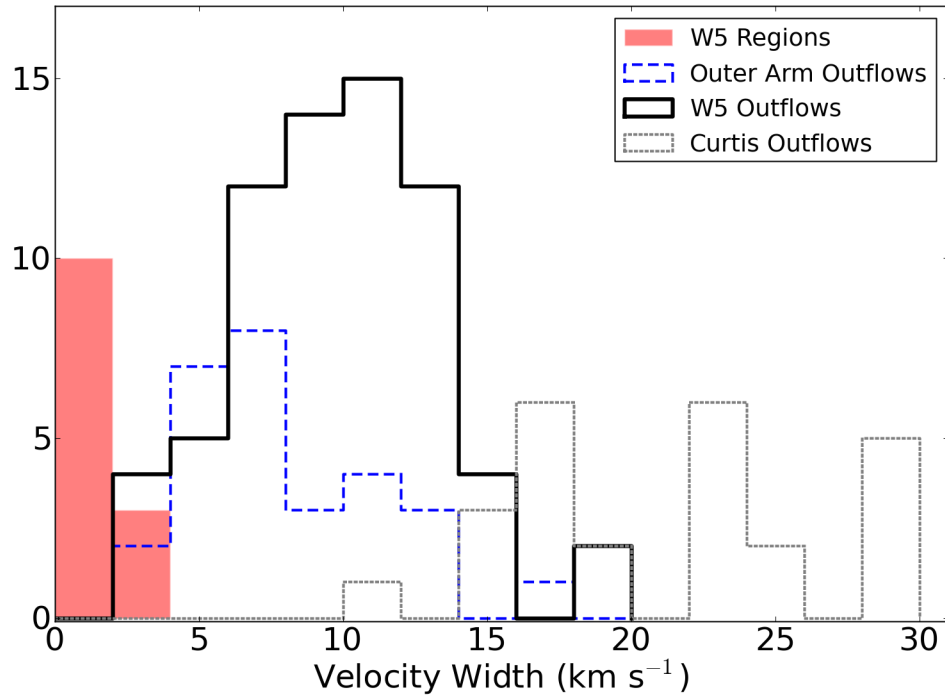


Figure 2.9 Histogram of the outflow line widths. *Black lines*: histogram of the measured outflow widths (half-width zero-intensity, measured from the fitted central velocity of the cloud to the highest velocity with non-zero emission). *Blue dashed lines*: outflow half-width zero-intensity (HWZI) for the outer arm (non-W5) sample. *Solid red shaded*: The measured widths (HWHM) of the sub-regions as tabulated in Table ???. *Gray dotted*: Outflow v_{max} (HWZI) values for Perseus from ?).

by low-velocity gas and therefore our dominant uncertainty may be missing low-velocity emission rather than poor assumptions about the optical depth.

The scalar momentum and energy were computed from

$$p = M \frac{\sum T_A^*(v)(v - v_c)\Delta v}{\sum T_A^*(v)\Delta v} \quad (2.1)$$

$$E = \frac{M}{2} \frac{\sum T_A^*(v)(v - v_c)^2\Delta v}{\sum T_A^*(v)\Delta v} \quad (2.2)$$

where v_c is the ^{13}CO 1-0 centroid velocity. The same assumptions used in determining column density are applied here.

We estimate an outflow lifetime by taking half the distance between the red and blue outflow centroids divided by the maximum measured velocity difference ($\Delta v_{max} = (v_{max,red} - v_{max,blue})/2$), $\tau_{flow} = L_{flow}/(2\Delta v_{max})$, where L_{flow} refers to the length of the flow. This method assumes that the outflow inclination is 45° ; if it is more parallel to the plane of the sky, we overestimate the age, and vice-versa. The momentum flux is then $\dot{P} = p/\tau$. Similarly, we compute a mass loss rate by dividing the total outflow mass by the dynamical age, which yields what is likely a lower limit on the mass loss rate (if the lifetime is underestimated, the mass loss rate is overestimated, but the outflow mass is always a lower limit because of optical depth and confusion effects).

The dynamical ages are highly suspect since the red and blue lobes are often unresolved or barely resolved, and diffuse emission averaged with the lobe emission can shift the centroid position. Additionally, it is not clear what portion of the outflow corresponds to the centroid: the bow shock or the jet could both potentially dominate the outflow emission. [?\)](#) discuss the many ways in which the dynamical age can be in error. Our mass loss rates are similar to those in Perseus **without** correcting our measurements for optical depth, while our outflow masses are an order of magnitude lower. It therefore appears that our dynamical age estimates must be too low, since we have no reason to expect protostars in W5 to be undergoing mass loss at a greater rate than those in Perseus. However, given more reliable dynamical age estimates from higher resolution observations of shock tracers, the mass loss rates could be corrected and compared to other star-forming regions.

Because the emission was assumed to be optically thin, the mass, column, energy, and momentum measurements we present are strictly lower limits. While some authors have computed correction factors to ^{12}CO 1-0 optical depths (e.g. ?), the corrections are different for the 3-2 transition (1.8 to 14.3, ?). Additionally, CO 3-2 may require a correction for sub-thermal excitation because of its higher critical density (the CO 3-2 critical density is 27 times higher than CO 1-0; see Appendix ?? for modeling of this effect).

Additionally, most of the outflow mass is at the lowest distinguishable velocities in typical outflows (e.g. ?). It is therefore plausible that in the more turbulent W5 region, a greater fraction of the outflow mass is blended (velocity confused) with the cloud and therefore not included in mass, momentum, and energy measurements. This omission could be greater than the underestimate due to poor opacity assumptions.

The total mass of the W5 outflows is $M_{tot} \approx 1.5M_\odot$, substantially lower, even with an optical depth correction of 10×, than the $163 M_\odot$ reported in Perseus (?). ?) also include a correction factor of 2.5 to account for higher temperatures in outflows and a factor of 2 to account for emission blended with the cloud. The temperature correction is inappropriate for CO 3-2 (see Appendix ??, Figure ??), but the resulting total outflow mass in W5 with an optical depth correction and a factor of 2 confusion correction is about $30 M_\odot$. In order to make our measurements consistent with a mass of $160 M_\odot$, a density upper limit in the outflowing gas of $n(\text{H}_2) < 10^{3.5}\text{cm}^{-3}$ is required, since a lower gas density results in greater mass for a given intensity (see Appendix ??, Figure ??). However, we expect the total outflow mass in W5 to be greater than in Perseus because of the greater cloud mass, implying that the density in the flows must be even lower, or additional corrections are needed.

The total outflow momentum is $p_{tot} \approx 10.9M_\odot \text{ km s}^{-1}$, versus a quoted $517 M_\odot \text{ km s}^{-1}$ in Perseus (?). ?) included inclination and dissociative shock corrections for the momentum measurements on top of the correction factors already applied to the mass. If these corrections are removed from the Perseus momentum total (except for optical depth, which is variable in their data and therefore cannot be removed), the uncorrected outflow momentum in Perseus would be

about $74 M_{\odot}$ km s $^{-1}$. The W5 outflow momentum, if corrected with a ‘typical’ optical depth in the range 7-14, would match or exceed this value. If an additional CO 3-2 excitation correction (in the range 1-20) is applied, the W5 outflow momentum would significantly exceed that in Perseus.

Assuming a turbulent line width $\Delta v \sim 3$ km s $^{-1}$ (approximately the smallest FWHM line-width observed), the total turbulent momentum in the ambient cloud is $p = M_{tot}\Delta v = 1.3 \times 10^5 M_{\odot}$ km s $^{-1}$, which is $\sim 10^5$ times the measured outflow momentum - the outflows detected in our survey cannot be the sole source of the observed turbulent line widths, even if corrected for optical depth and missing mass.

Table ?? presents the turbulent momentum for each sub-region computed by multiplying the measured velocity width by the integrated ^{13}CO mass. Even if the outflow measurements are orders of magnitude low because of optical depth, cloud blending, sub-thermal excitation, and other missing-mass considerations, outflows contribute negligibly to the total momentum of high velocity gas in W5. This result is unsurprising, as there are many other likely sources of energy in the region such as stellar wind bubbles and shock fronts between the ionized and molecular gas. Additionally, in regions unaffected by feedback from the HII region (e.g. W5NW), cloud-cloud collisions are a possible source of energy.

Figure ?? displays the distribution of measured properties and compares them to those derived in the COMPLETE (?) and ?) HARP CO 3-2 surveys of Perseus. Our derived masses are substantially lower than those in ?) even if corrected for optical depth, but our momenta are similar to the CPOC (COMPLETE Perseus Outflow Candidate) sample and our energies are higher, indicating a bias towards detecting mass at high velocities. The bias is more heavily towards high velocities than the CO 1-0 used in ?). The discrepancy between our values and those of ?) and ?) can be partly accounted for by the optical depth correction applied in those works: ^{13}CO was used to correct for opacity at low velocities, where most of the outflow mass is expected. Those works may also have been less affected by blending because of the smaller cloud line widths in Perseus.

The momentum flux and mass loss rate are compared to the values derived in Perseus by ?) and ?) in Figures ?? and ???. Both of our values are computed using the dynamical timescale

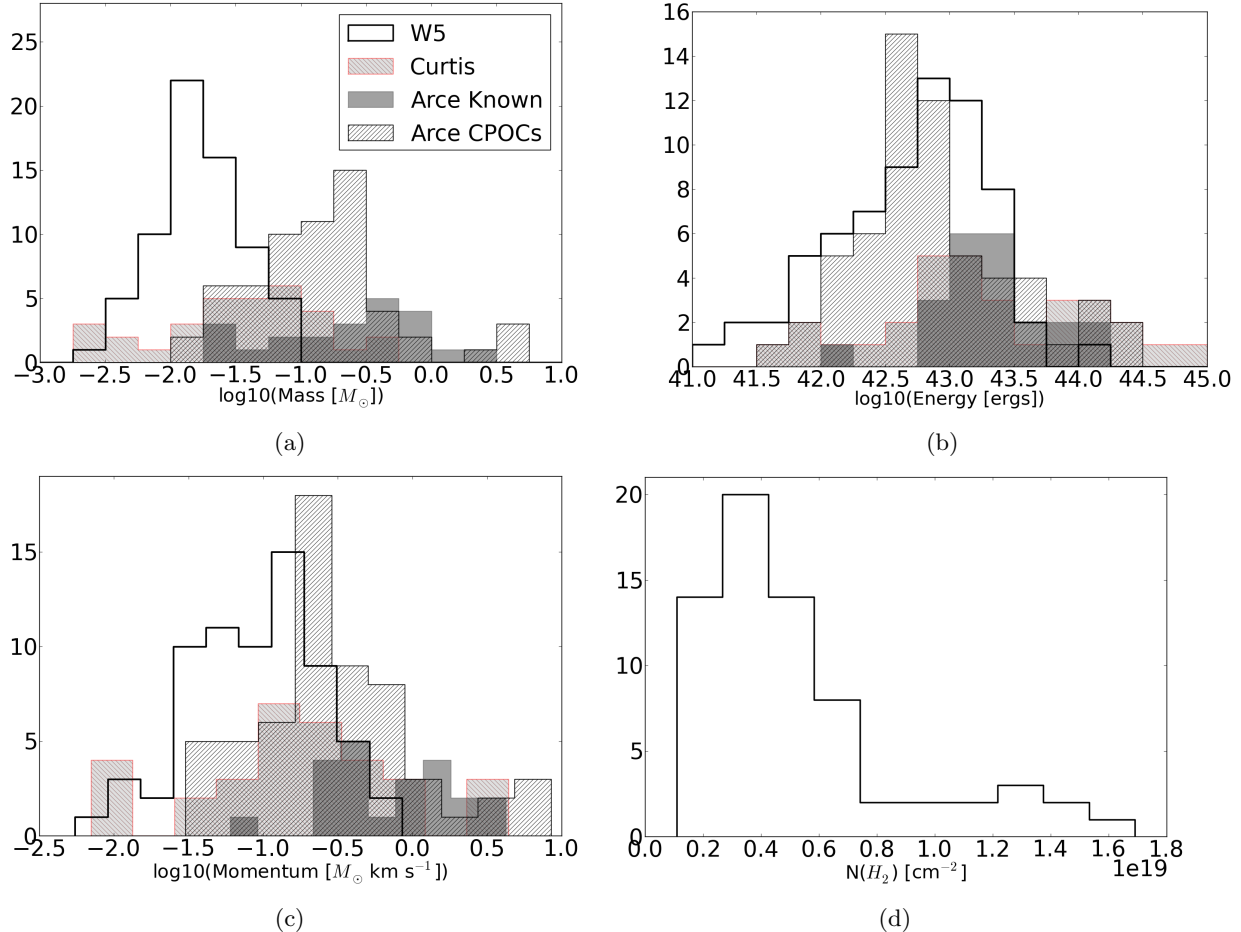


Figure 2.10 Histograms of outflow physical properties. The solid unfilled lines are the W5 outflows (this paper), the forward-slash hashed lines show ?) CPOCs , the dark gray shaded region shows ?) values for known outflows in Perseus, and the light gray, backslash-hashed regions show ?) CO 3-2 outflow properties. The outflow masses measured in Perseus are systematically higher partly because both surveys corrected for line optical depth using ^{13}CO . The medians of the distributions are $0.017, 0.044, 0.33$, and $0.14 M_\odot$ for W5, Curtis, Arce Known, and Arce CPOCs respectively, which implies that an optical depth and excitation correction factor of 2.5-20 would be required to make the distributions agree (although W5, being a more massive region, might be expected to have more massive and powerful outflows). It is likely that CO 3-2 is sub-thermally excited in outflows, and CO outflows may be destroyed by UV radiation in the W5 complex while they easily survive in the lower-mass Perseus region, which are other factors that could push the W5 mass distribution lower.

τ_d measured from outflow lobe separation, while the ?) values are derived using a more direct momentum-flux measurement in which the momentum flux contribution of each pixel in the resolved outflow map is considered. The derived momentum fluxes (Figure ??) are approximately consistent with the ?) Perseus momentum fluxes; ?) measure momentum fluxes in a range $1 \times 10^{-6} < \dot{P} < 7 \times 10^{-4} M_\odot \text{ km s}^{-1} \text{ yr}^{-1}$, higher than our measured $6 \times 10^{-7} < \dot{P} < 1 \times 10^{-4} M_\odot \text{ km s}^{-1} \text{ yr}^{-1}$ by approximately the opacity correction they applied. As seen in Figure ??, the ?) momentum flux measurements in Perseus cover a much lower range $6 \times 10^{-8} < \dot{P} < 2 \times 10^{-5} M_\odot \text{ km s}^{-1} \text{ yr}^{-1}$ and are not consistent with our measurements. This disagreement is most likely because of the difference in method. The W5 outflows exhibit substantially higher mass-loss rates and momentum fluxes if we assume a factor of 10 opacity correction, as expected from our bias toward higher-velocity, higher-mass flows.

2.4.2 Structure of the W5 molecular clouds: A thin sheet?

The W5 complex extends $\sim 1.6^\circ \times 0.7^\circ$ within 20° of parallel with the galactic plane. At the assumed distance of 2 kpc, it has a projected length of ~ 60 pc (Figure ??). In the $8 \mu\text{m}$ band (Figure ??), the region appears to consist of two blown-out bubbles with $\sim 10 - 15$ pc radii centered on $\ell = 138.1, b = 1.4$ and $\ell = 137.5, b = 0.9$. While the bubbles are filled in with low-level far-infrared emission, there is no CO detected down to a $3 - \sigma$ limit of 3.0 K km s^{-1} ($^{12}\text{CO } 1-0$), 2.4 K km s^{-1} ($^{12}\text{CO } 3-2$, excepting a few isolated clumps), and 1.5 K km s^{-1} ($^{13}\text{CO } 1-0$). Using the X-factor (the CO-to-H₂ conversion factor) for ^{12}CO $N(\text{H}_2) = 3.6 \times 10^{20} \text{ cm}^{-2}/(\text{K km s}^{-1})$, we derive an upper limit $N(\text{H}_2) < 1.1 \times 10^{21} \text{ cm}^{-2}$, or $A_V \lesssim 0.6$. Individual ‘wisps’ and ‘clumps’ of CO can sometimes be seen, particularly towards the cloud edges, but in general the bubbles are absent of CO gas.

Given such low column limits, the W5 cloud must be much smaller along the line of sight than its ~ 50 pc size projected on the sky. Alternately, along the line-of-sight, the columns of molecular gas are too low for CO to self-shield, and it is therefore destroyed by the UV radiation of W5’s O-stars. In either case, there is a significant excess of molecular gas in the plane of the

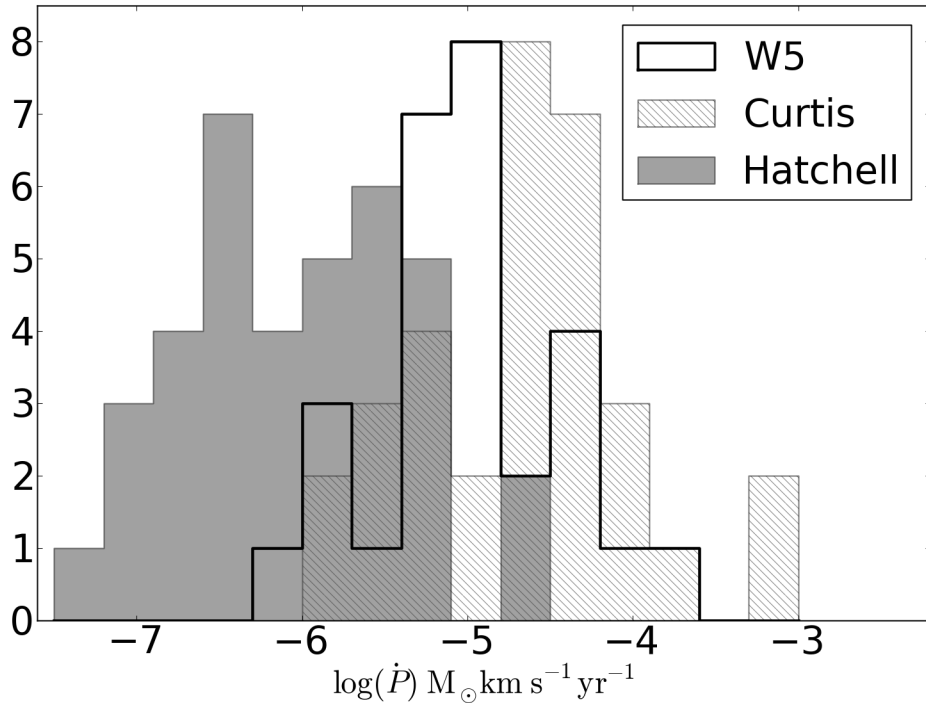


Figure 2.11 Histogram of the measured outflow momentum fluxes. The black thick line shows our data, the grey shaded region shows the ?) data, and the hatched region shows ?) values. Our measurements peak squarely between the two Perseus JCMT CO 3-2 data sets, although the ?) results include an opacity correction that our data do not, suggesting that our results are likely consistent with ?) but inconsistent with the ?) direct measurement method.

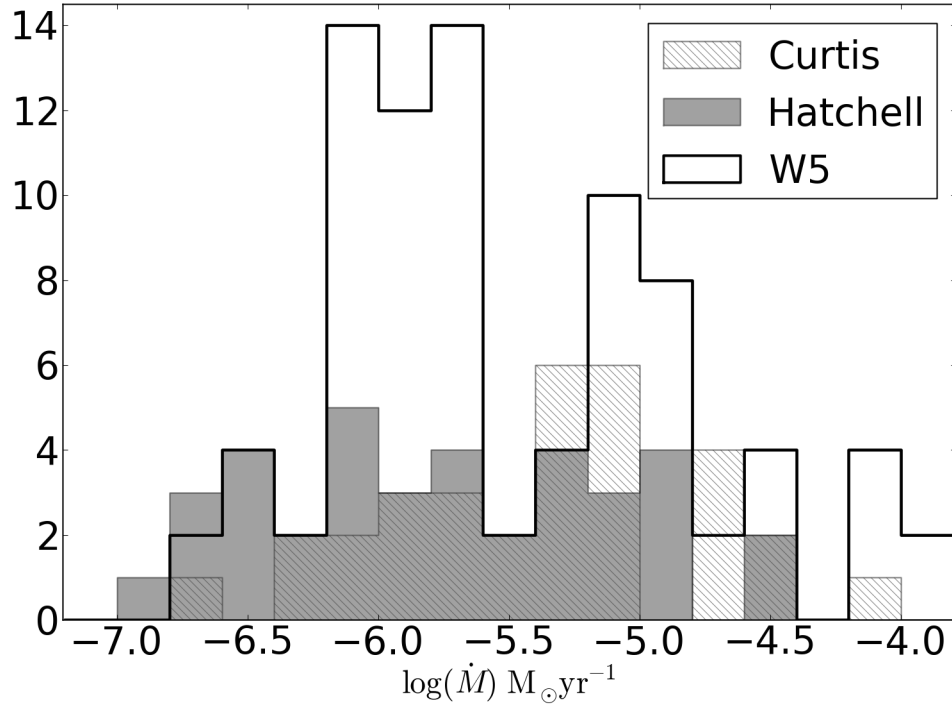


Figure 2.12 Histogram of the measured mass loss rate. The black thick line shows our data, while the grey shaded region shows the ?) data, which is simply computed by $\dot{M} = \dot{P} \times 10/5 \text{ km s}^{-1}$, where the factor of 10 is a correction for opacity. Our mass loss rates are very comparable to those of ?), but different methods were used so the comparison may not be physically meaningful. ?) (hatched) used a dynamical time method similar to our own and also derived similar mass loss rates, although their mass measurements have been opacity-corrected using the ^{13}CO 3-2 line. Because our mass loss rates agree reasonably with Perseus, but our outflow mass measurements are an order of magnitude low, we believe our dynamical age estimates to be too small.

sky compared to the line of sight, which makes W5 an excellent location to perform unobscured observations of the star formation process. The implied thin geometry of the W5 molecular cloud may therefore be similar to the bubbles observed by ?), but on a larger scale.

There is also morphological evidence supporting the face-on hypothesis. In the AFGL 4029 region (Section ??) and all along the south of W5, there are ridges with many individual cometary ‘heads’ pointing towards the O-stars that are unconfused along the line of sight. This sort of separation would not be expected if we were looking through the clouds towards the O-stars. W5W, however, presents a counterexample in which there are two clouds along the line of sight that may well be masking a more complex geometry.

2.5 Sub-regions

Individual regions were selected from the mosaic for comparison. All regions with multiple outflows and indicators of star formation activity were named and included as regions for analysis. Additionally, three “inactive” regions were selected based on the presence of ^{13}CO emission but the lack of outflows in the ^{12}CO 3-2 data. Finally, two regions devoid of CO emission were selected as a baseline comparison and to place upper limits on the molecular gas content of the east and west ‘bubbles’. The regions are identified on the integrated ^{13}CO image in Figure ??.

Average spectra were taken of each “region” within the indicated box. Gaussians were fit to the spectrum to determine line-widths and centers (Figure ??, Table ??). Gaussian fits were necessary because in many locations there are at least two velocity components, so the second moment (the “intensity-weighted dispersion”) is a poor estimator of line width. Widths ranged from $v_{FWHM} = 2.3$ to 6.2 km s^{-1} (Figure ??).

2.5.1 Sh 2-201

Sh 2-201 is an HII region and is part of the same molecular cloud as the bright-rimmed clouds in W5E, but it does not share a cometary shape with these clouds (Figure ??). Instead, it is internally heated and has its own ionizing source (?). The AFGL 4029 cloud edge is at a projected

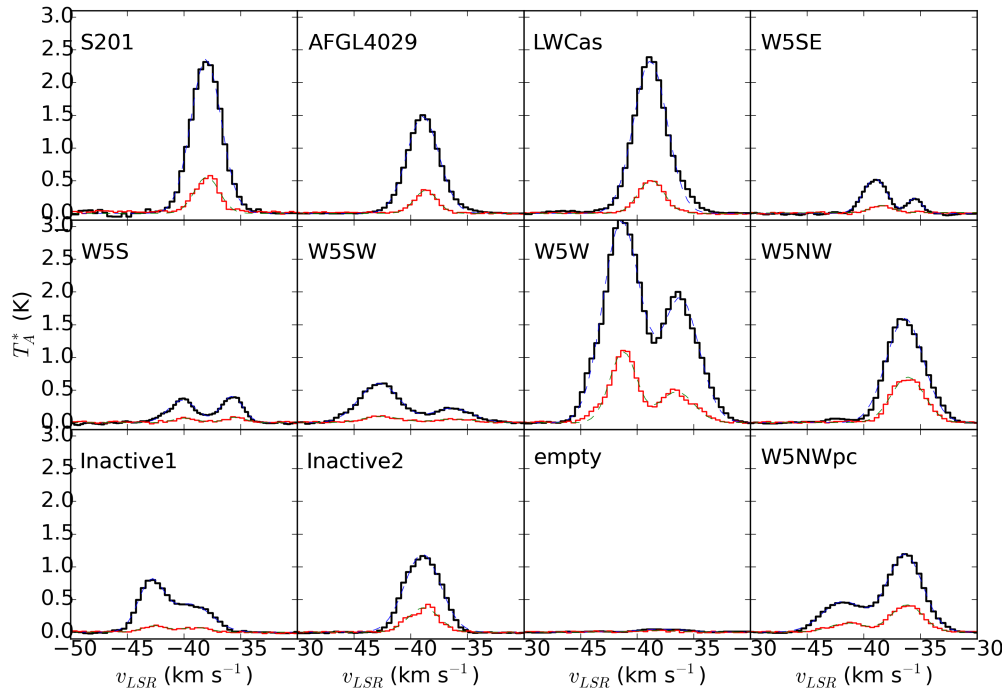


Figure 2.13 Spatially averaged spectra of the individual regions analyzed. ^{12}CO 3-2 is shown by thick black lines and ^{13}CO 1-0 is shown by thin red lines. Gaussian fits are overplotted in blue and green dashed lines, respectively. The fit properties are given in Table ??.

distance of ~ 7 pc from the nearest exposed O-star, and the closest illuminated point in the Spitzer 8 and 24 μm maps is at a projected distance of ~ 5 pc. The star forming process must therefore have begun before radiation driven shocks from the W5 O-stars could have impacted the cloud.

2.5.2 AFGL 4029

AFGL 4029 is a young cluster embedded in a cometary cloud (Figure ??). There is one clear bipolar outflow and 6 single-lobed flows that cannot be unambiguously associated with an opposite direction counterpart. The cluster is mostly unresolved in the data presented here and is clearly the most active CO clump in W5. It contains a cluster of at least 30 B-stars (?). The outflows from this region have a full width $\Delta v \approx 30 \text{ km s}^{-1}$, which is entirely inconsistent with a radiation-driven inflow or outflow since it is greater than the sound speed in the ionized medium.

The northeast cometary cloud is strongly affected by the W5 HII region. It has an outflow in the head of the cloud (Figure ??), and the cloud shows a velocity gradient with distance from the HII region. The polarity of the gradient suggests that the cometary cloud must be on the far side of the ionizing O-star along the line of sight assuming that the HII region pressure is responsible for accelerating the cloud edge.

2.5.3 W5 Ridge

The W5 complex consists of two HII region bubbles separated by a ridge of molecular gas (Figure ??). This ridge contains the LW Cas optical nebula, a reflection nebula around the variable star LW Cas, on its east side and an X-shaped nebula on the west. The east portion of LW Cas Nebula is bright in both the continuum and CO J=3-2 but lacks outflows (see Figure ??). The east portion also has the highest average peak antenna temperature, suggesting that the gas temperature in this region is substantially higher than in the majority of the W5 complex (higher spatial densities could also increase the observed T_A , but the presence of nearby heating sources make a higher temperature more plausible). It is possible that high gas temperatures are suppressing star formation in the cloud. Alternately, the radiation that is heating the gas may

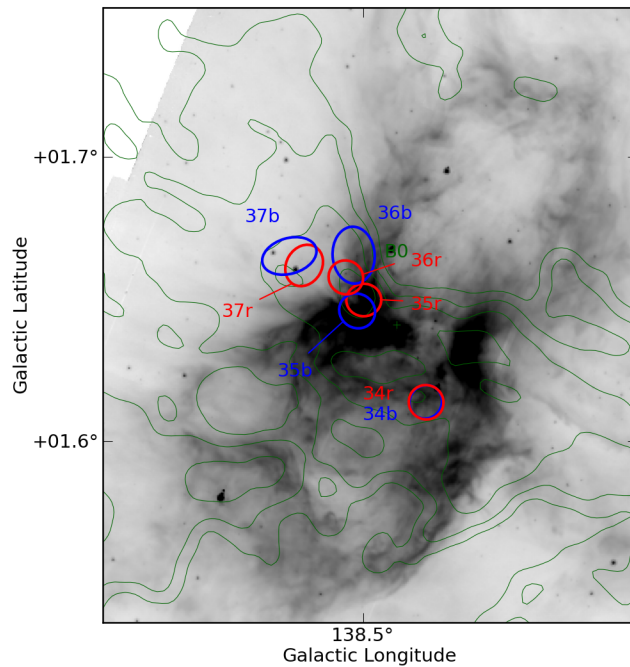


Figure 2.14 Small scale map of the Sh 2-201 region plotted with CO 3-2 contours integrated from -60 to -20 km s⁻¹ at levels 3,7.2,17.3,41.6, and 100 K km s⁻¹. The IRAC 8 μ m image is displayed in inverted log scale from 800 to 8000 MJy sr⁻¹. Contours of the CO 3-2 cube integrated from -60 to -20 km s⁻¹ are overlaid at logarithmically spaced levels from 3 to 100 K km s⁻¹ (3.0,7.2,17.3,41.6,100; $\sigma \approx 0.7$ K km s⁻¹). The ellipses represent the individual outflow lobe apertures mentioned in Section ??.

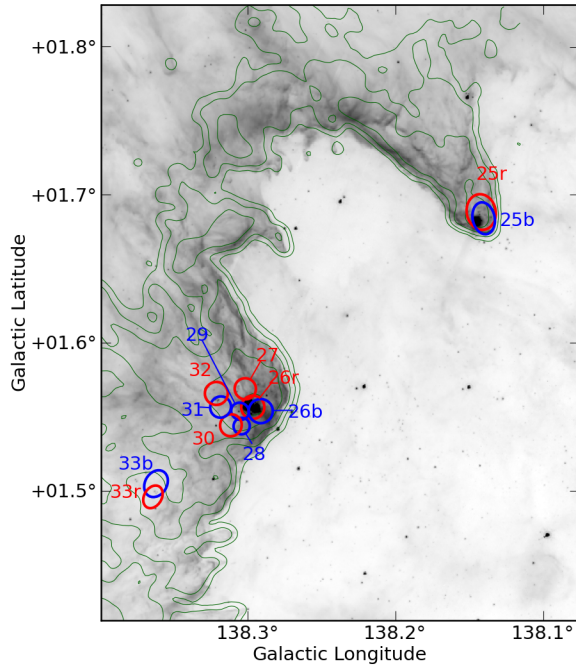


Figure 2.15 Small scale map of the AFGL 4029 region plotted with CO 3-2 contours integrated from -60 to -20 km s^{-1} at levels $3, 7.2, 17.3, 41.6$, and 100 K km s^{-1} . The IRAC $8 \mu\text{m}$ image is displayed in inverted log scale from 800 to 8000 MJy sr^{-1} . Contours of the CO 3-2 cube integrated from -60 to -20 km s^{-1} are overlaid at logarithmically spaced levels from 3 to 100 K km s^{-1} ($3.0, 7.2, 17.3, 41.6, 100; \sigma \approx 0.7 \text{ K km s}^{-1}$). Outflows 26-32 are ejected from a forming dense cluster. A diagram displaying the kinematics of the northern cometary cloud is shown in Figure ??.

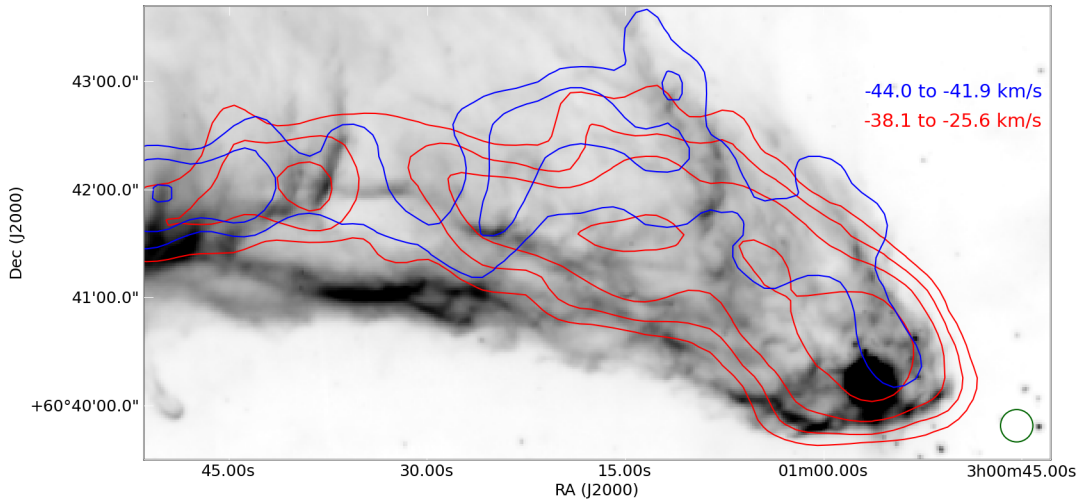


Figure 2.16 The northeast cometary cloud. Contours are shown at 0.5, 1, 2, and 5 K km s^{-1} integrated over the ranges -44.0 to -41.9 km s^{-1} (blue) and -38.1 to -35.6 km s^{-1} (red). There is a velocity gradient across the tail, suggesting that the front edge is being pushed away along the line of sight.

destroy any outflowing CO, which is more likely assuming the two Class I objects identified in this region by ?) are genuine protostars.

The ridge is surprisingly faint in HI 21 cm emission compared to the two HII regions (Figure ??) considering its $24 \mu m$ surface brightness. The integrated HI intensity from -45 to -35 km s $^{-1}$ is $\sim 800 \text{ K km s}^{-1}$, whereas in the HII region bubble it is around 1000 K km s^{-1} . The CO-bright regions show lower levels of emission similar to the ridge at $700\text{-}800 \text{ K km s}^{-1}$. However, the ridge contains no CO gas and very few young stars (Figure 7 in ?). It is possible that the ridge contains cool HI but has very low column-densities along the direction pointing towards the O-stars, in which case the self-shielding is too little to prevent CO dissociation. This ridge may therefore be an excellent location to explore the transition from molecular to atomic gas under the influence of ionizing radiation in conditions different from high-density photodissociation (photon-dominated) regions.

We examine Outflow 20 as a possible case for pressure-driven implosion (radiation, RDI, or gas pressure, PDI) by examining the relative timescales of the outflow driving source and the HII-region-driven compression front. A typical molecular outflow source (Class 0 or I) has a lifetime of $\sim 5 \times 10^5$ years (?). Given that there is an active outflow at the head of this cloud, we use 0.5 MYr as an upper limit. The approximate distance from this source to the cloud front behind it is $\sim 3.3 \text{ pc}$. If we assume the cloud front has been pushed at a constant speed $v \leq c_{II} \approx 10 \text{ km s}^{-1}$, we derive a lower limit on its age of 0.3 MYr. While these limits allow for the protostar to be older than the compression front by up to 0.2 MYr, it is likely that the compression front moved more slowly (e.g., 3 km s^{-1} if it was pushed by a D-type shock front) and that the protostar is not yet at the end of its lifetime - it is very plausible that this source was born in a radiation-driven implosion.

2.5.4 Southern Pillars

There are 3 cometary clouds that resemble the “elephant trunk” nebula in IC 1396 (Figure ??). Each of these pillars contains evidence of at least one outflow in the head of the cloud (see the supplementary materials, outflows 16-19 and 38) These pillars are low-mass and isolated;

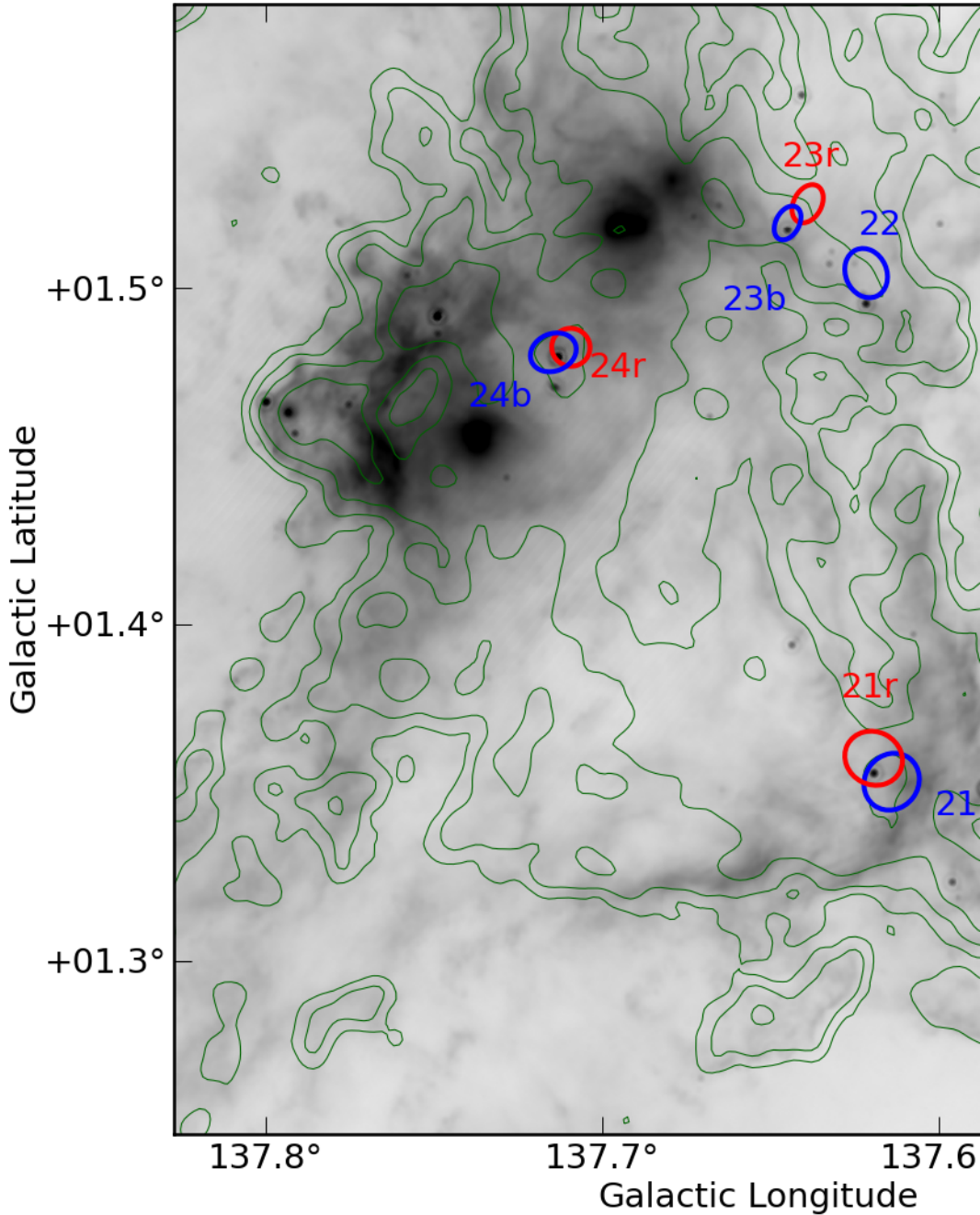


Figure 2.17 Small scale map of the LW Cas nebula plotted with CO 3-2 contours integrated from -60 to -20 km s^{-1} at levels $3, 7.2, 17.3, 41.6$, and 100 K km s^{-1} . The feature containing outflows 20 and 21 is the X-shaped ridge referenced in Section ???. This sub-region is notable for having very few outflows associated with the most significant patches of CO emission. The gas around it is heated on the left side by the O7V star HD 18326 ($D_{proj} = 8.5 \text{ pc}$), suggesting that this gas could be substantially warmer than the other molecular clouds in W5.

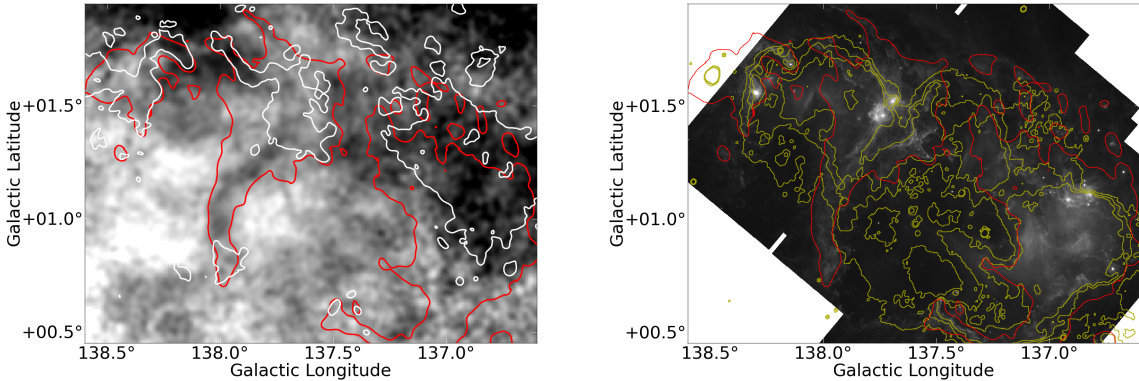


Figure 2.18 *Top:* The DRAO 21 cm HI map integrated from -45 to -35 km s^{-1} displayed in grayscale from 700 (black) to 1050 (white) K km s^{-1} with IRAS $100 \mu\text{m}$ contours (red, 40 MJy sr^{-1}) and ^{12}CO 1-0 contours integrated over the same range (white, 4 K km s^{-1}) overlaid. The ridge of IRAS $100 \mu\text{m}$ emission at $\ell = 138.0$ coincides with a relative lack of HI emission at these velocities, suggesting either that there is less or colder gas along the ridge. *Bottom:* The Spitzer $24 \mu\text{m}$ map with 21 cm continuum contours at 6, 8, and 10 MJy sr^{-1} overlaid. The IRAS contours are also overlaid to provide a reference for comparing the two figures and to demonstrate that the HII region abuts the cold-HI area. The moderate excess of continuum emission implies a somewhat higher electron density along the line of sight through the ridge.

there is no other outflow activity in southern W5. However, because of the bright illumination on their northern edges and robust star formation tracers, these objects present a reasonable case for triggered star formation by the RDI mechanism.

The kinematics of these cometary clouds suggest that they have been pushed in different directions by the HII region (Figure ??). The central cometary cloud (Figure ??b) has two tails. The southwest tail emission peaks around -39.5 km s^{-1} and the southeast tail peaks at -41.5 km s^{-1} , while the head is peaked at an intermediate -40.5 km s^{-1} . These velocity shifts suggest that the gas is being accelerated perpendicular to the head-tail axis and that the southeast tail is on the back side of the cometary head, while the southwest tail is on the front side. The expanding HII region is crushing this head-tail system.

The southeast cometary cloud (Figure ??a) peaks at -35.0 km s^{-1} . There are no clearly-separated CO tails as in the central cloud, but there is a velocity shift across the tail, in which the west (right) side is blueshifted compared to the east (left) side, which is the opposite sense from the central cometary cloud.

The southwest cometary cloud (Figure ??c) peaks at -40.3 km s^{-1} and has weakly defined tails similar to the central cloud. Both of its tails are at approximately the same velocity (-42.5 km s^{-1}).

The kinematics of these tails provide some hints of their 3D structure and location in the cloud. Future study to compare the many cometary flows in W5 to physical models and simulations is warranted. Since these flows are likely at different locations along the line of sight (as required for their different velocities), analysis of their ionized edges may allow for more precise determination of the full 3D structure of the clouds relative to their ionizing sources.

2.5.5 W5 Southeast

The region identified as W5SE has very little star formation activity despite having significant molecular gas ($M_{13}\text{CO} \sim 800M_\odot$). While there are two outflows and two Class I objects (?) in the southeast of the two clumps ($\ell = 138.15, b = 0.77$, Figure ??), the main clump ($\ell = 138.0, b = 0.8$)

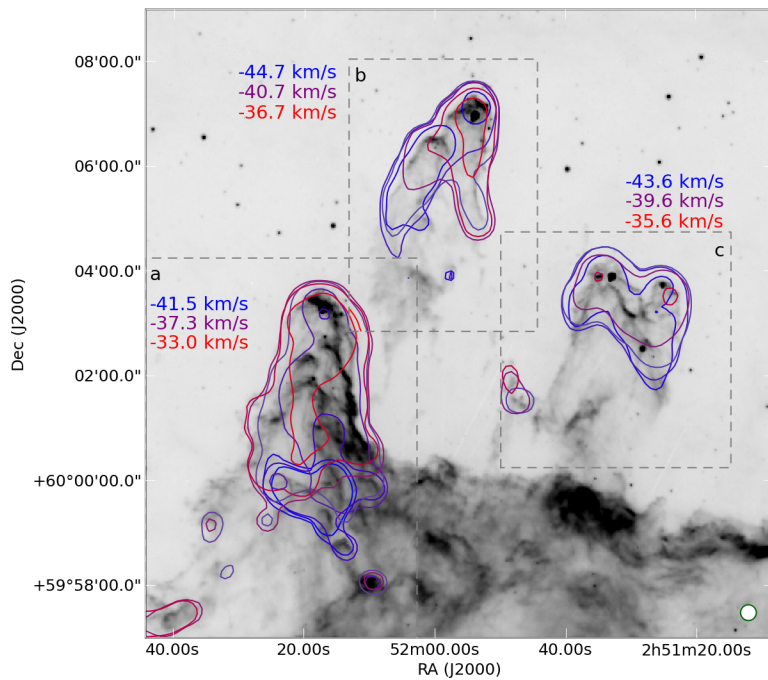


Figure 2.19 CO 3-2 contours overlaid on the Spitzer $8 \mu\text{m}$ image of the W5S cometary clouds described in Section ???. Contours are color-coded by velocity and shown for 0.84 km s^{-1} channels at levels of 1 K (a, b) and 0.5 K (c). The velocity ranges plotted are (a) -41.5 to -33.0 km s^{-1} (b) -44.7 to -36.7 km s^{-1} (c) -43.6 to -35.6 km s^{-1} . The labels show the minimum, maximum, and middle velocities to guide the eye. The grey boxes indicate the regions selected for CO contours; while there is CO emission associated with the southern $8 \mu\text{m}$ emission, we do not display it here. The velocity gradients are discussed in Section ???.

has no detected outflows. The CO emission is particularly clumpy in this region, with many independent, unresolved clumps both in position and velocity. In the 8 and 24 micron Spitzer images, it is clear that these clouds are illuminated from the northwest. This region represents a case in which the expanding HII region has impacted molecular gas but has not triggered additional star formation. The high clump-to-clump velocity dispersion observed in this region may be analogous to the W5S cometary clouds (Section ??) but without condensed clumps around which to form cometary clouds.

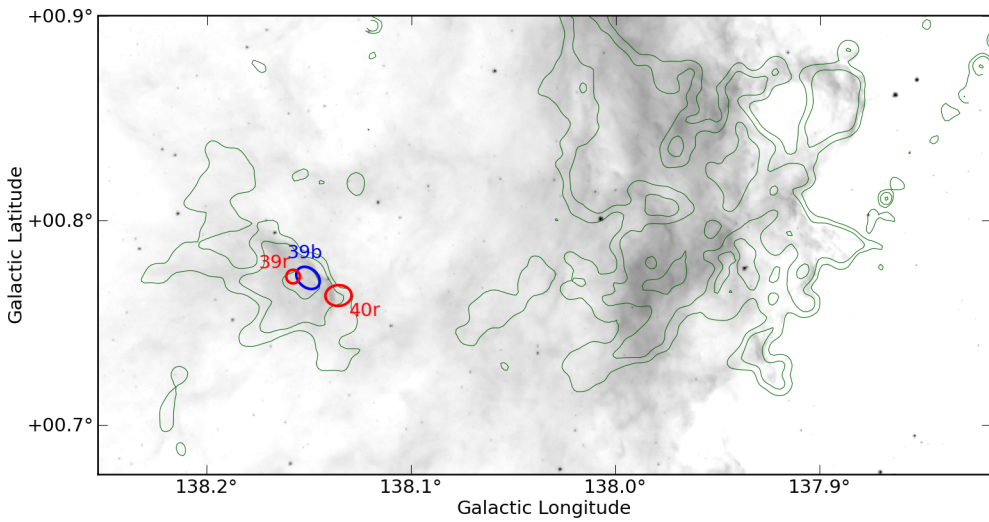


Figure 2.20 Small scale map of the W5 SE region showing the star-forming clump containing outflows 39 and 40 and the non-star-forming clump at $\ell = 138.0, b = 0.8$. CO 3-2 contours integrated from -60 to -20 km s $^{-1}$ are displayed at levels 3,7,2,17,3,41,6, and 100 K km s $^{-1}$.

2.5.6 W5 Southwest

There is an isolated clump associated with outflows in the southwest part of W5 (Figure ??) at $v_{LSR} \sim -45$ km s $^{-1}$. While this clump is likely to be associated with the W5 region, it shows little evidence of interaction with the HII region. If it is eventually impacted by the expanding ionization front (i.e. if it is within the W5 complex), this clump will be an example of “revealed”, not triggered, star formation.

The other source in W5SW is a cometary cloud with a blueshifted head and redshifted tail (Figure ??; Outflow 13). The head contains a redshifted outflow; no blueshifted counterpart was detected (the velocity gradient displayed in Figure ?? is smaller than the outflow velocity and is also redshifted away from the head). The lack of a blueshifted counterpart may be because the flow is blowing into ionized gas where the CO is dissociated.

Because of its evident interaction with the HII region, this source is an interesting candidate for a non-protostellar outflow impersonator. However, because the head is blueshifted relative to the tail, we can infer that the head has been accelerated towards us by pressure from the HII region, implying that it is in the foreground of the cloud. Given this geometry, a radiation-driven flow would appear blueshifted, not redshifted, as the detected flow is. Additionally, the outflow is seen as fast as 7.5 km s^{-1} redshifted from the cloud, which is a factor of 2 too fast to be driven by radiation in a standard D-type shock. Finally, the outflow velocity is much greater than seen in a simulation of a cometary cloud by ?), while the head-to-tail velocity gradient is comparable.

2.5.7 W5 West / IC 1848

There is a bright infrared source seen in the center of W5W (IRAS 02459+6029; Figure ??), but the nearest CO outflow lobe is $\approx 1 \text{ pc}$ away. The nondetection may be due to confusion in this area: there are two layers of CO gas separated by $\sim 5 \text{ km s}^{-1}$, so low-velocity outflow detection is more difficult. Unlike the rest of the W5 complex, this region appears to have multiple independent confusing components along the line of sight (Figure ??), and therefore the CO data provide much less useful physical information (multiple components are also observed in the ^{13}CO data, ruling out self-absorption as the cause of the multiple components).

2.5.8 W5 NW

The northwest cluster containing outflows 1-8 is at a slightly different velocity ($\sim -35 \text{ km s}^{-1}$) than the majority of the W5 cloud complex ($\sim -38 \text{ km s}^{-1}$; Figure ??), but it shares contiguous emission with the neighboring W5W region. It contains many outflows and therefore is actively

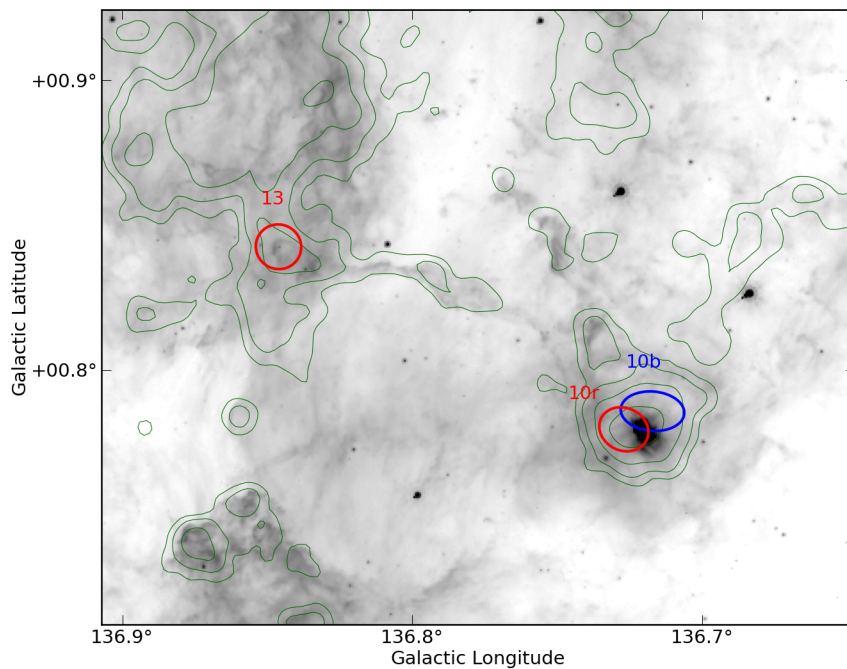


Figure 2.21 Small scale map of the W5 SW region plotted with CO 3-2 contours integrated from -60 to -20 km s^{-1} at levels $3, 7.2, 17.3, 41.6$, and 100 K km s^{-1} . Outflow 13 is at the head of a cometary cloud (Figure ??) and therefore has clearly been affected by the expanding HII region, but the region including bipolar Outflow 10 shows no evidence of interaction with the HII region.

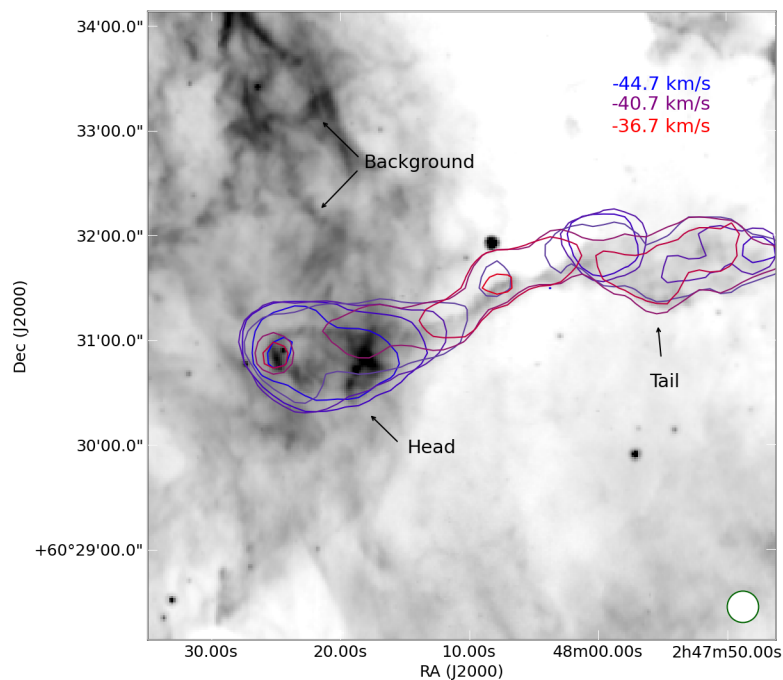


Figure 2.22 The cometary cloud in the W5 Southwest region (Outflow 13). Contours are shown at 1 K for 0.84 km s⁻¹ wide channels from -37.2 km s⁻¹ (blue) to -30.5 km s⁻¹ (red). The head is clearly blueshifted relative to the tail and contains a spatially unresolved redshifted outflow.

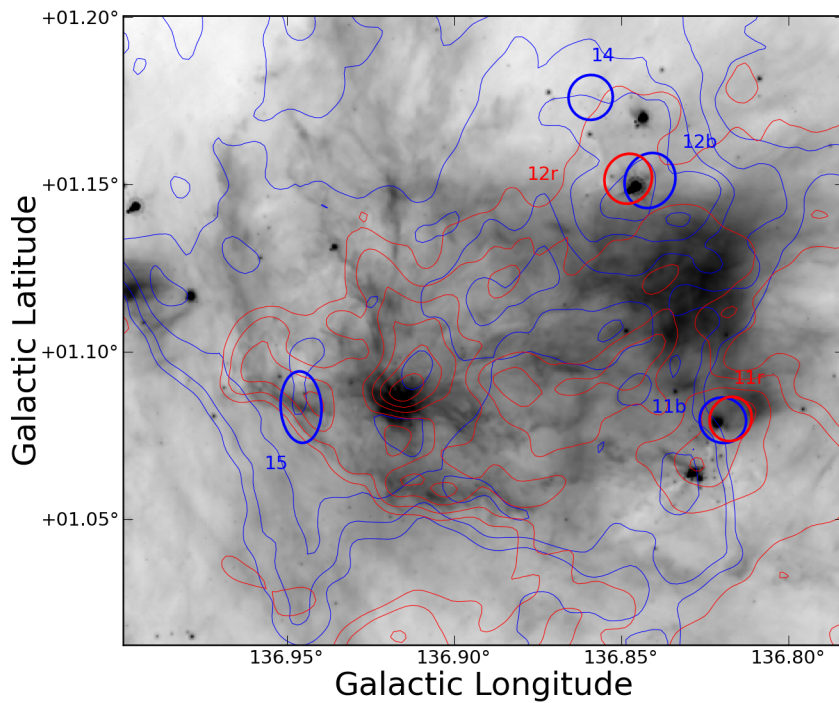


Figure 2.23 Small scale map of the W5 W region. The IRAC $8 \mu\text{m}$ image is displayed in inverted log scale from 800 to 8000 MJy sr^{-1} . Contours of the CO 3-2 cube integrated from -50 to -38 km s^{-1} (blue) and -38 to -26 km s^{-1} (red) are overlaid at levels $5, 10, 20, 30, 40, 50, 60 \text{ K km s}^{-1}$ $\sigma \approx 0.5 \text{ K km s}^{-1}$. The lack of outflow detections is partly explained by the two spatially overlapping clouds that are adjacent in velocity.

forming stars (Figure ??). However, this cluster exhibits much lower CO brightness temperatures and weaker Spitzer $8 \mu\text{m}$ emission than the “bright-rimmed clouds” seen near the W5 O-stars. We therefore conclude that the region has not been directly impacted by any photoionizing radiation from the W5 O-stars.

The lack of interaction with the W5 O-stars implies that the star formation in this region, though quite vigorous, has not been directly triggered. Therefore not all of the current generation of star formation in W5 has been triggered on small or intermediate scales (e.g., radiation-driven implosion). Even the “collect and collapse” scenario seems unlikely here, as the region with the most outflows also displays some of the smoothest morphology (Figures ?? and ??); in “collect and collapse” the expansion of an HII region leads to clumping and fragmentation, and the spaces between the clumps should be relatively cleared out.

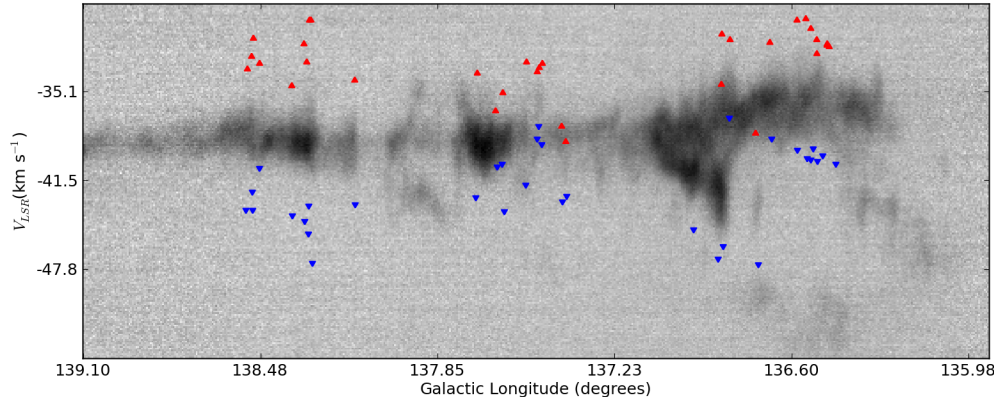


Figure 2.24 Integrated longitude-velocity diagram of the W5 complex from $b = 0.25$ to $b = 2.15$ in ^{12}CO 1-0 from the FCRAO OGS. The W5NW region is seen at a distinct average velocity around $\ell = 136.5$, $v_{\text{LSR}} = -34 \text{ km s}^{-1}$. The red and blue triangles mark the longitude-velocity locations of the detected outflows. In all cases, they mark the low-velocity start of the outflow.

2.6 Discussion

2.6.1 Comparison to other outflows

The outflow properties we derive are similar to those in the B0-star forming clump IRAS 05358+3543 ($M \approx 600M_{\odot}$?), in which CO 3-2 and 2-1 were used to derive outflow masses in the

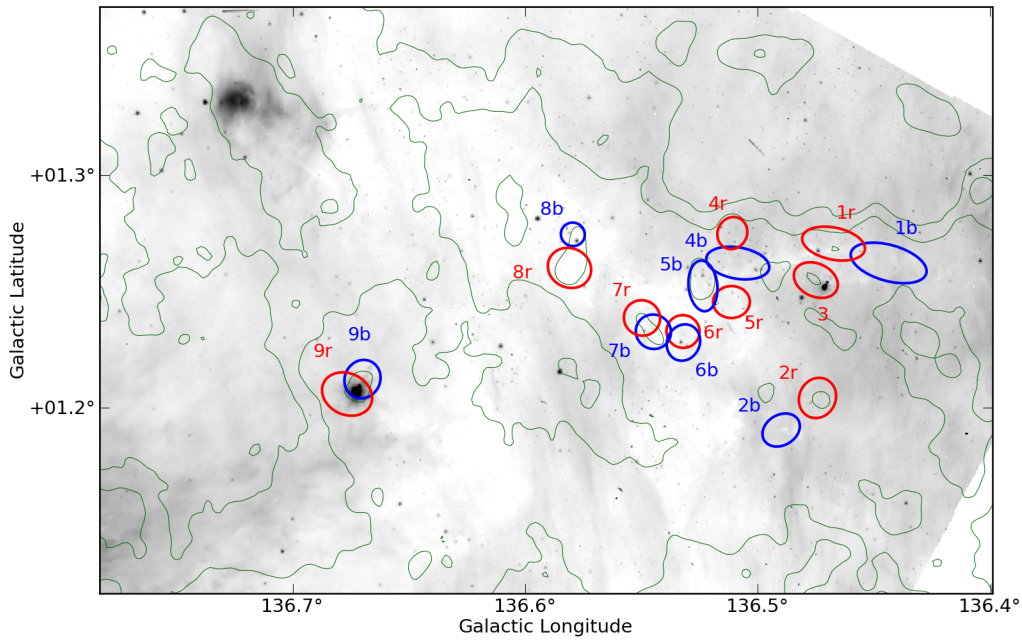


Figure 2.25 Small scale map of the W5 NW region plotted with CO 3-2 contours integrated from -60 to -20 km s^{-1} at levels $3, 7, 2, 17, 3, 41, 6$, and 100 K km s^{-1} . Despite its distance from the W5 O-stars, $D_{proj} \approx 20$ pc, this cluster is the most active site of star formation in the complex as measured by outflow activity.

range 0.01-0.09 M_{\odot} . However, some significantly larger outflows, up to 1.6 pc in one direction were detected, while the largest resolved outflow in our survey was only 0.8 pc (one direction).

As noted in Section ??, the total molecular mass in W5 is larger than Perseus, $M_{W5} \sim 4.5 \times 10^4 M_{\odot}$ while $M_{Perseus} \sim 10^4 M_{\odot}$ (?). The length distribution of outflows (Figure ??) is strikingly similar, while other physical properties have substantially different mean values with or without correction factors included.

The W5NW region is more directly comparable to Perseus, with a total mass of $\sim 1.5 \times 10^4 M_{\odot}$ (Table ??) and a similar size. In Figure ??, we show both the W5NW region, which contains all of the identified outflows, and the W5NWpc region, which is a larger area intended to be directly comparable in both mass and spatial scale to the Perseus molecular cloud. The W5NWpc region contains more than an order of magnitude more turbulent energy than the Perseus complex ($E_{turb,Per} = 1.6 \times 10^{46}$ ergs, ?) despite its similar mass. Even the smaller W5NW region has $\sim 5 \times$ more turbulent energy than the Perseus complex, largely because of the greater average line width ($\sigma_{FWHM,W5NW} \approx 3.5$ km s $^{-1}$). As with the whole of W5, there is far too much turbulent energy in W5NW to be provided by outflows alone, implying the presence of another driver of turbulence.

Figure ?? shows the W5NWpc region and Perseus molecular cloud on the same scale, though in two different emission lines. The Perseus cloud contains many more outflows and candidates (70 in Perseus vs. 13 in W5NWpc) despite a much larger physical area surveyed in W5. While it is likely that many of the W5W outflows will break apart into multiple flows at higher resolution, it does not seem likely that each would break apart into 5 flows, as would be required to bring the numbers into agreement. Since the highest density of outflows in Perseus is in the NGC 1333 cloud, it may be that there is no equivalently evolved region in W5NWpc. The W5W region may be comparably massive, but it is also confused and strongly interacting with the W5 HII region - either star formation is suppressed in this region, or outflows are rendered undetectable. In the latter case, the most likely mechanisms for hiding outflows are molecular dissociation by ionizing radiation and velocity confusion.

Another possibility highlighted in Figure ?? is that the W5NW region is interacting with

the W4 bubble. The cloud in the top right of Figure ?? is somewhat cometary, has higher peak brightness temperature, and is at a slightly different velocity (-45 km s^{-1}) than W5NW. The velocity difference of $\sim 8 \text{ km s}^{-1}$ could simply be two clouds physically unassociated along the line of sight, or could indicate the presence of another expanding bubble pushing two sheets of gas away from each other. Either way, the northwest portion of the W5NW region is clumpier than the area in which the outflows were detected, and it includes no outflow detections.

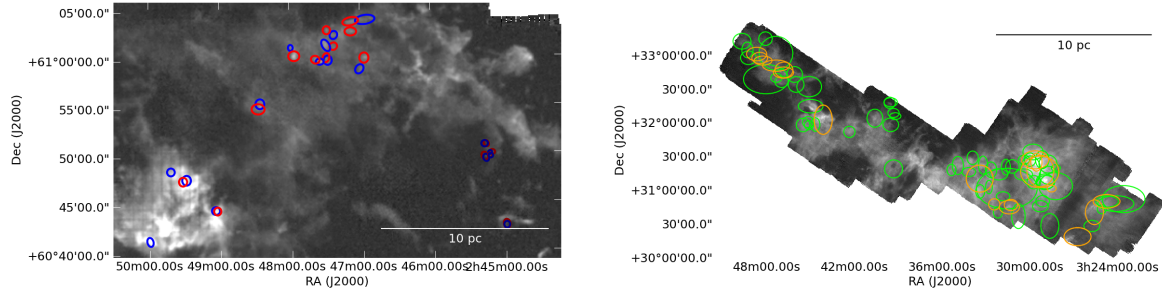


Figure 2.26 (a) An integrated CO 3-2 image of the W5W/NW region with ellipses overlaid displaying the locations and sizes of outflows. The dark red and blue ellipses in the lower right are associated with outer-arm outflows. W5W is the bottom-left, CO-bright region. W5NW is the top-center region containing the cluster of outflows. (b) An integrated CO 1-0 image of the Perseus molecular cloud from the COMPLETE survey (?). Note that the spatial scale is identical to that of (a) assuming that W5 is 8 times more distant than Perseus. The green ellipses represent (?) CPOCs while the orange represent known outflows from the same paper.

2.6.2 Star Formation Activity

CO outflows are an excellent tracer of ongoing embedded star formation (e.g. ?). We use the locations of newly discovered outflows to qualitatively describe the star formation activity within the W5 complex and evaluate the hypothesis that star formation has been triggered on small or intermediate scales.

Class 0/I objects are nearly always associated with outflows in nearby star-forming regions (e.g. Perseus ??). However, ?) detected 171 Class I sources in W5 using Spitzer photometry. Since our detection threshold for outflow appears to be similar to that in Perseus (Section ??), the lower number of outflow detections is surprising, especially considering that some of the detected outflows are outside the Spitzer-MIPS field (MIPS detections are required for Class I objects, and

flows 1-4 are outside that range) or are in the outer arm (flows 39-54). Additionally, we should detect outflows from Class 0 objects that would not be identified by Spitzer colors.

There are a number of explanations for our detection deficiency. The Class I objects detected within the HII region “bubble” most likely have outflows in which the CO is dissociated similar to jet systems in Orion (e.g. HH46/47, a pc-scale flow in which CO is only visible very near the protostar; ??). This hypothesis can be tested by searching for optical and infrared jets associated with these objects, which presumably have lower mass envelopes and therefore less extinction than typical Class I objects. Additionally, there are many outflow systems that are likely to be associated with clusters of outflows rather than individual outflows as demonstrated in Section ??, where we were able to identify fewer outflows when ‘observing’ the Perseus objects at a greater distance. There are 24 sources in the ?) Class I catalog within 15'' (one JCMT beam at 345 GHz) of another, and in many cases there are multiple ?) Class I sources within the contours of a single outflow system.

2.6.3 Evaluating Triggering

In the previous section, we discussed in detail the relationship between each sub-region and the HII region. Some regions are observed to be star-forming but not interacting with the HII region (W5NW, Sh 2-201), while others are interacting with the HII region but show no evidence or reduced evidence of star formation (W5SE, W5W, LW Cas). At the very least, there is significant complexity in the triggering mechanisms, and no one mechanism or size scale is dominant. If we were to trust outflows as unbiased tracers of star formation, we might conclude that the majority of star formation in W5 is untriggered (spontaneous), but such a conclusion is unreliable because both radiatively triggered star formation and “revealed” star formation may not exhibit molecular outflows (although ionized atomic outflows should still be visible around young stars formed through these scenarios).

In Section ??, we analyzed a particular case in which the RDI mechanism could plausibly have crushed a cloud to create the observed protostar. It is not possible to determine whether

interaction with the HII region was a necessary precondition for the star's formation, but it at least accelerated the process. The other cometary clouds share this property, but in total there are only 5 cometary clouds with detected outflows at their tips, indicating that this mechanism is not the dominant driver of star formation in W5.

The ‘collect and collapse’ scenario might naively be expected to produce an excess of young stars at the interaction front between the HII region and the molecular cloud. However, because such interactions naturally tend to form instabilities, this scenario produces cloud morphologies indistinguishable from those of RDI. There is not an obvious excess of sources associated with cloud edges over those deep within the clouds (e.g., Figure ??). We therefore cannot provide any direct evidence for this triggering scenario.

The overall picture of W5 is of two concurrent episodes of massive-star formation that have lead to adjacent blown-out bubbles. Despite the added external pressure along the central ridge, it is relatively deficient in both star formation activity and dense gas, perhaps because of heating by the strong ionizing radiation field. The lack of star formation along that central ridge implies that much of the gas was squeezed and heated, but it was not crushed into gravitationally unstable fragments. While some star formation may have been triggered in W5, there is strong evidence for pre-existing star formation being at least a comparable, if not the dominant, mechanism of star formation in the complex.

2.7 Outflow systems beyond W5

Fifteen outflows were detected at velocities inconsistent with the local W5 cloud velocities. Of these, 8 are consistent with Perseus arm velocities ($v_{LSR} > -55 \text{ km s}^{-1}$) and could be associated with different clouds within the same spiral arm. The other 7 have central velocities $v_{LSR} < -55 \text{ km s}^{-1}$ and are associated with the outer arm identified in previous surveys (e.g. ?). The properties of these outflows are given in Tables ?? and ??; the distances listed are kinematic distances assuming $R_0 = 8.4 \text{ kpc}$ and $v_0 = 254 \text{ km s}^{-1}$ (?).

Of these outflows, all but one are within $2'$ of an IRAS point source. Outflow 54 is the most

distant in our survey at a kinematic distance $d = 7.5$ kpc ($v_{lsr} = -75.6$ km s $^{-1}$) and galactocentric distance $D_G = 14.7$ kpc. It has no known associations in the literature.

Outflows 41 - 44 are associated with a cloud at $v_{LSR} \sim -62$ km s $^{-1}$ known in the literature as LDN 1375 and associated with IRAS 02413+6037. Outflows 53 and 55 are at a similar velocity and associated with IRAS 02598+6008 and IRAS 02425+6000 respectively. All of these sources lie roughly on the periphery of the W5 complex.

Outflows 45 - 52 are associated with a string of IRAS sources and HII regions to the north of W5 and have velocities in the range $-55 < v_{LSR} < -45$. They therefore could be in the Perseus arm but are clearly unassociated with the W5 complex. Outflows 45 and 46 are associated with IRAS 02435+6144 and they may also be associated with the Sharpless HII region Sh 2-194. Outflows 47 and 48 are associated with IRAS 02461+6147, also known as AFGL 5085. Outflows 49 and 50 are nearby but not necessarily associated with IRAS 02475+6156, and may be associated with Sh 2-196. Outflows 51 and 52 are associated with IRAS 02541+6208.

2.8 Conclusions

We have identified 40 molecular outflow candidates in the W5 star forming region and an additional 15 outflows spatially coincident but located in the outer arm of the Galaxy.

- The majority of the CO clouds in the W5 complex are forming stars. Star formation is not limited to cloud edges around the HII region. Because star formation activity is observed outside of the region of influence of the W5 O-stars, it is apparent that direct triggering by massive star feedback is not responsible for all of the star formation in W5.
- The W5 complex is seen nearly face-on as evidenced by a strict upper limit on the CO column through the center of the HII-region bubbles. It is therefore an excellent region to study massive star feedback and revealed and triggered star formation.
- Outflows contribute negligibly to the turbulent energy of molecular clouds in the W5 complex. This result is unsurprising near an HII region, but supports the idea that massive

star forming regions are qualitatively different from low-mass star-forming regions in which the observed turbulence could be driven by outflow feedback. Even in regions far separated from the O-stars, there is more turbulence and less energy injection from outflows than in, e.g., Perseus.

- Despite detecting a significant number of powerful outflows, the total outflowing mass detected in this survey ($\sim 1.5 M_{\odot}$ without optical depth correction, perhaps $10 - 20 M_{\odot}$ when optical depth is considered) was somewhat smaller than in Perseus, a low to intermediate mass star forming region with $\sim 1/6$ the molecular mass of W5.
- The low mass measured may be partly because the CO 3-2 line is sub-thermally excited in outflows. Therefore, while CO 3-2 is an excellent tracer of outflows for detection, it does not serve as a ‘calorimeter’ in the same capacity as CO 1-0.
- Even considering excitation and optical depth corrections, it is likely that the mass of outflows in W5 is less than would be expected from a simple extrapolation from Perseus based on cloud mass. CO is likely to be photodissociated in the outflows when they reach the HII region, accounting for the deficiency around the HII region edges. However, in areas unaffected by the W5 O-stars such as W5NW, the deficiency may be because the greater turbulence in the W5 clouds suppresses star formation or hides outflows.
- Velocity gradients across the tails of many cometary clouds have been observed, hinting at their geometry and confirming that the outflows seen from their heads must be generated by protostars within.
- Outflows have been detected in the Outer Arm at galactocentric distances $\gtrsim 12$ kpc. These represent some of the highest galactocentric distance star forming regions discovered to date.

2.9 Acknowledgements

We thank the two anonymous referees for their assistance in refining this document. We thank Devin Silvia for a careful proofread of the text. This work has made use of the APLpy plotting package (<http://aplpy.sourceforge.net>), the pyregion package (<http://leejjoon.github.com/pyregion/>), the agpy code package (<http://code.google.com/p/agpy/>) , IPAC's Montage (<http://montage.ipac.caltech.edu/>), the DS9 visualization tool (<http://hea-www.harvard.edu/RD/ds9/>), the pyspeckit spectroscopic analysis toolkit (<http://pyspeckit.bitbucket.org>), and the STARLINK package (<http://starlink.jach.hawaii.edu/>). IRAS data was acquired through IRSA at IPAC (<http://irsa.ipac.caltech.edu/>). DRAO 21 cm data was acquired from the Canadian Astronomical Data Center (<http://cadcwww.hia.nrc.ca/cgps/>). The authors are supported by the National Science Foundation through NSF grant AST-0708403. This research has made use of the SIMBAD database, operated at CDS, Strasbourg, France

2.10 W5 Appendix: Optically Thin, LTE dipole molecule

While many authors have solved the problem of converting CO 1-0 beam temperatures to H₂ column densities (????), there are no examples in the literature of a full derivation of the LTE, optically thin CO-to-H₂ conversion process for higher rotational states. We present the full derivation here, and quantify the systematic errors generated by various assumptions.

We begin with the assumption of an optically thin cloud such that the radiative transfer equation (? , eqn 1.9) simplifies to

$$\frac{dI_\nu}{ds} = -\kappa_\nu I_\nu \quad (2.3)$$

The absorption and stimulated emission terms yield

$$\kappa_\nu = \frac{h\nu_{ul}B_{ul}n_u}{c}\varphi(\nu) - \frac{h\nu_{ul}B_{lu}n_l}{c}\varphi(\nu) \quad (2.4)$$

where $\varphi(\nu)$ is the line shape function ($\int \varphi(\nu)d\nu \equiv 1$), n is the density in the given state, ν is the frequency of the transition, B is the Einstein B coefficient, and h is Planck's constant.

By assuming LTE (the Boltzmann distribution) and using Kirchoff's Law and the definition of the Einstein A and B values, we can derive a more useful version of this equation

$$\kappa_\nu = \frac{c^2}{8\pi\nu_{ul}^2}n_uA_{ul}\left[\exp\left(\frac{h\nu_{ul}}{k_B T_{ex}}\right) - 1\right]\varphi(\nu) \quad (2.5)$$

where k_B is Boltzmann's constant.

The observable T_B can be related to the optical depth, which is given by

$$\int \tau_\nu d\nu = \frac{c^2}{8\pi\nu_{ul}^2}A_{ul}\left[\exp\left(\frac{h\nu_{ul}}{k_B T_{ex}}\right) - 1\right] \int \varphi(\nu)d\nu \int n_u ds \quad (2.6)$$

Rearranging and converting from density to column ($\int n ds = N$) gives an equation for the column density of the molecule in the upper energy state of the transition:

$$N_u = \frac{8\pi\nu_{ul}^2}{c^2 A_{ul}} \left[\exp\left(\frac{h\nu_{ul}}{k_B T_{ex}}\right) - 1\right]^{-1} \int \tau_\nu d\nu \quad (2.7)$$

In order to relate the brightness temperature to the optical depth, at CO transition frequencies the full blackbody formula must be used and the CMB must also be taken into account. ?)

equation 15.29

$$T_B(\nu) = \frac{h\nu}{k_B} \left(\left[e^{h\nu/k_B T_{ex}} - 1 \right]^{-1} - \left[e^{h\nu/k_B T_{CMB}} - 1 \right]^{-1} \right) (1 - e^{-\tau_\nu}) \quad (2.8)$$

is rearranged to solve for τ_ν :

$$\tau_\nu = -\ln \left[1 - \frac{k_B T_B}{h\nu} \left(\left[e^{h\nu/k_B T_{ex}} - 1 \right]^{-1} - \left[e^{h\nu/k_B T_{CMB}} - 1 \right]^{-1} \right)^{-1} \right] \quad (2.9)$$

We convert from frequency to velocity units with $d\nu = \nu/cdv$, and plug Equation ?? into Equation ?? to get

$$N_u = \frac{8\pi\nu_{ul}^3}{c^3 A_{ul}} \left[\exp \left(\frac{h\nu_{ul}}{k_B T_{ex}} \right) - 1 \right]^{-1} \int -\ln \left[1 - \frac{k_B T_B}{h\nu_{ul}} \left(\left[e^{h\nu_{ul}/k_B T_{ex}} - 1 \right]^{-1} - \left[e^{h\nu_{ul}/k_B T_{CMB}} - 1 \right]^{-1} \right)^{-1} \right] dv \quad (2.10)$$

which is the full LTE upper-level column density with no approximations applied.

The first term of the Taylor expansion is appropriate for $\tau << 1$ ($\ln[1+x] \approx x - \frac{x^2}{2} + \frac{x^3}{3} \dots$)

$$N_u = \frac{8\pi\nu_{ul}^3}{c^3 A_{ul}} \left[\exp \left(\frac{h\nu_{ul}}{k_B T_{ex}} \right) - 1 \right]^{-1} \int \frac{k_B T_B}{h\nu_{ul}} \left(\left[e^{h\nu_{ul}/k_B T_{ex}} - 1 \right]^{-1} - \left[e^{h\nu_{ul}/k_B T_{CMB}} - 1 \right]^{-1} \right)^{-1} dv \quad (2.11)$$

which simplifies to

$$N_u = \frac{8\pi\nu_{ul}^2 k_B}{c^3 A_{ul} h} \frac{e^{h\nu_{ul}/k_B T_{CMB}} - 1}{e^{h\nu_{ul}/k_B T_{CMB}} - e^{h\nu_{ul}/k_B T_{ex}}} \int T_B dv \quad (2.12)$$

This can be converted to use μ_e (0.1222 for ^{12}CO ; ?), the electric dipole moment of the molecule, instead of A_{ul} , using ?) equation 15.20 ($(A_{ul} = (64\pi^4)/(3hc^3)) \nu^3 \mu_e^2$):

$$N_u = \frac{3}{8\pi^3 \mu_e^2} \frac{k_B}{\nu_{ul}} \frac{2J_u + 1}{J_u} \frac{e^{h\nu_{ul}/k_B T_{CMB}} - 1}{e^{h\nu_{ul}/k_B T_{CMB}} - e^{h\nu_{ul}/k_B T_{ex}}} \int T_B dv \quad (2.13)$$

The total column can be derived from the column in the upper state using the partition function and the Boltzmann distribution

$$n_{tot} = \sum_{J=0}^{\infty} n_J = n_0 \sum_{J=0}^{\infty} (2J+1) \exp \left(-\frac{J(J+1)B_e h}{k_B T_{ex}} \right) \quad (2.14)$$

This equation is frequently approximated using an integral (e.g. ?), but a more accurate numerical solution using up to thousands of rotational states is easily computed

$$n_J = \left[\sum_{j=0}^{j_{max}} (2j+1) \exp \left(-\frac{j(j+1)B_e h}{k_B T_{ex}} \right) \right]^{-1} (2J+1) \exp \left(-\frac{J(J+1)B_e h}{k_B T_{ex}} \right) \quad (2.15)$$

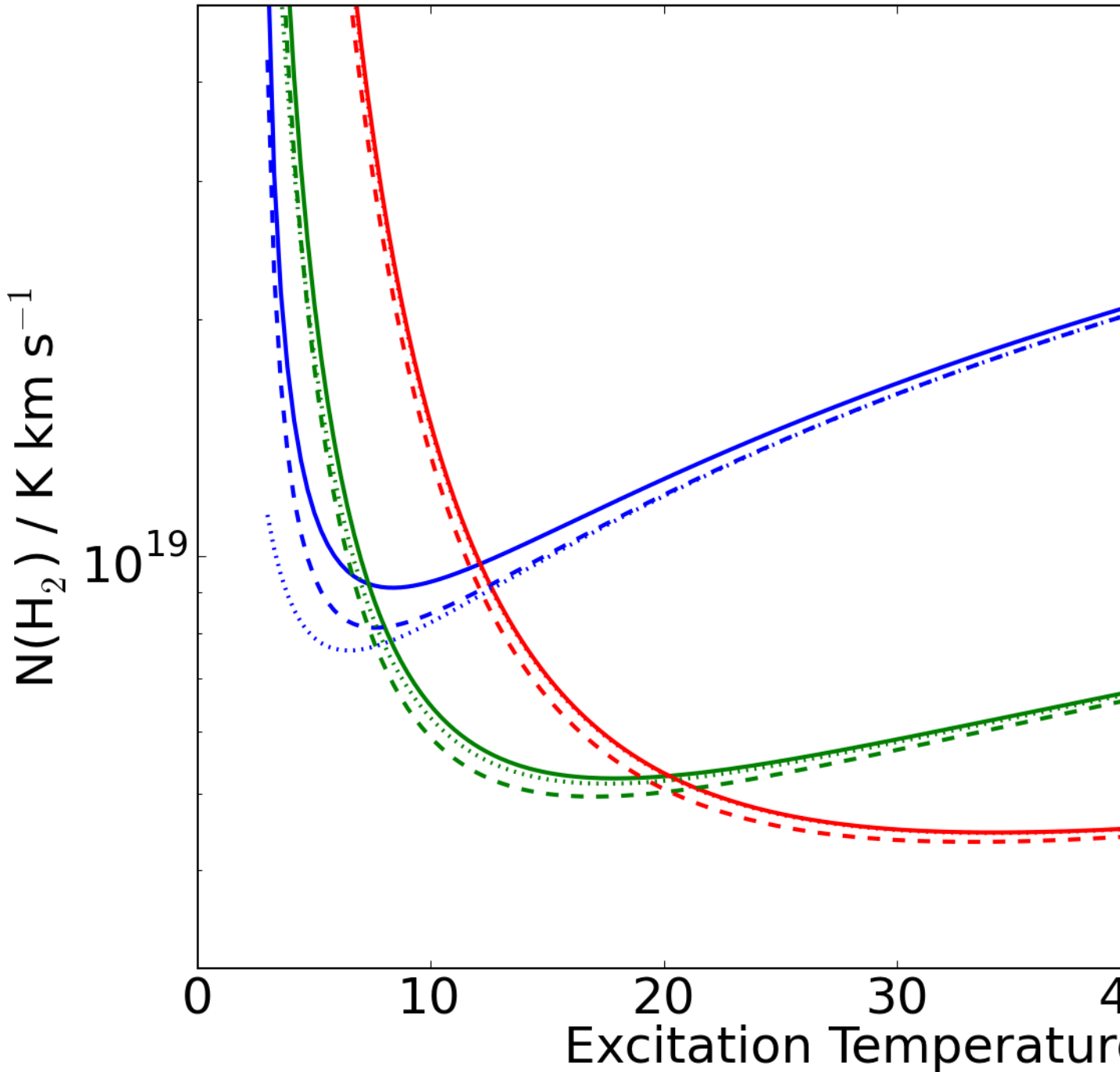


Figure 2.27 The LTE, optically thin conversion factor from T_B (K km s^{-1}) to $N(\text{H}_2)$ (cm^{-2}) assuming $X_{^{12}\text{CO}} = 10^{-4}$ plotted against T_{ex} . The dashed line shows the effect of using the integral approximation of the partition function (e.g. ??). It is a better approximation away from the critical point, and is a better approximation for higher transitions. The dotted line shows the effects of removing the CMB term from Equation ??; the CMB populates the lowest two excited states, but contributes nearly nothing to the $J = 3$ state. Top (blue): $J=1-0$, Middle (green): $J=2-1$, Bottom (red): $J=3-2$.

The effects of using the approximation and the full numerical solution are shown in figure ??.

The CO 3-2 transition is also less likely to be in LTE than the 1-0 transition. The critical density ($n_{cr} \equiv A_{ul}/C_{ul}$) of ^{12}CO 3-2 is 27 times higher than that for 1-0. We have run RADEX (?) LVG models of CO to examine the impact of sub-thermal excitation on column derivation. The results of the RADEX models are shown in Figure ?? . They illustrate that, while it is quite safe to assume the CO 1-0 transition is in LTE in most circumstances, a similar assumption is probably invalid for the CO 3-2 transition in typical molecular cloud environments.

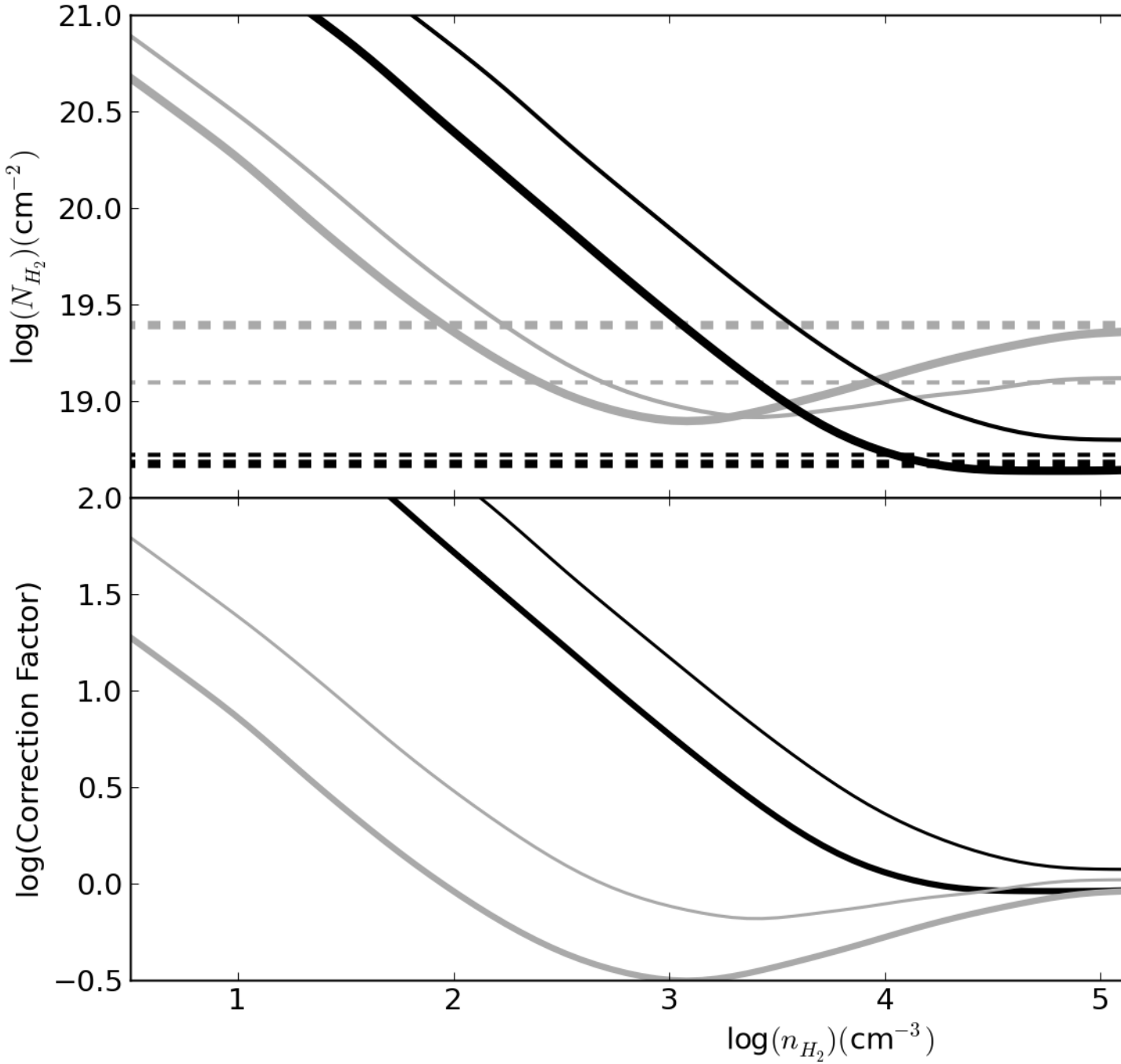


Figure 2.28 *Top*: The derived $N(H_2)$ as a function of n_{H_2} for $T_B = 1$ K. The dashed lines represent the LTE-derived $N(H_2)/T_B$ factor, which has no density dependence and, for CO 3-2, only a weak dependence on temperature. We assume an abundance of ^{12}CO relative to H_2 $X_{CO} = 10^{-4}$. *Bottom*: The correction factor ($N(H_2)_{RADEX} / N(H_2)_{LTE}$) as a function of n_{H_2} . For $T_K = 20$ K, the “correction factor” at 10^3 cm^{-3} (typical GMC mean volume densities) is ~ 15 , while at 10^4 cm^{-3} (closer to n_{crit} but perhaps substantially higher than GMC densities) it becomes negligible. The correction factor is also systematically lower for a higher gas kinetic temperature. For some densities, the “correction factor” dips below 1, particularly for CO 1-0. This effect is from a slight population inversion due to fast spontaneous decay rates from the higher levels and has been noted before (e.g. ?).

Chapter 3

The Bolocam Galactic Plane Survey

3.1 Preface

The Bolocam Galactic Plane Survey consumed the bulk of my time on this thesis. A great deal of that time was dedicated to development of the BGPS Pipeline (Section ??). That software is described in ?) and this chapter.

3.2 Version 1

The Bolocam Galactic Plane Survey (BGPS) Version 1 (v1.0) was released in 2009 and published in ?) and ?). ?) summarizes a great deal of the work in this thesis, in particular the reduction strategy implemented for the BGPS. However, since that paper was written in cooperation with James Aguirre, the text is not reproduced here and instead references to the paper are included within the description of v2.0 below.

3.3 Introduction

Surveys of the Galactic Plane have great legacy value and open broad regions of discovery space, e.g. the infrared IRAS (?), MSX (?), GLIMPSE (?), and MIPSGAL (?) surveys. Until the recent advent of hundred-bolometer millimeter arrays, blind surveys of large regions of the sky were impractical. However, instruments like Bolocam, Aztec, and LABOCA have changed the field, and Herschel has opened the terahertz window with the Hi-Gal galactic plane survey (?).

These Galactic plane surveys have lasting legacy value. The BGPS has been used to examine the properties of maser sources (??), outflow sources (?), and high-mass star-forming regions (???). It has served as the basis for studies of forming clusters (??) and intermediate-mass stars (?). The BGPS and other surveys have served as finder charts for large-scale millimeter line studies of the Galactic plane (??). These and many other studies demonstrate the need for, and benefits of, publicly available blind legacy surveys.

The Herschel space observatory and the Hi-Gal survey have provided access to the peak of the dust spectral energy distribution at reasonably high ($\sim 30''$) resolution. With these data becoming available, the need for long-wavelength data at comparable resolution is no less pressing: long-wavelength data is essential for constraining the dust emissivity, one of the free parameters in SED fits. ?) and ?) demonstrated the power of long-wavelength data in accurately determining both β and temperature.

The millimeter regime has been the last decade of wavelength space to become available to astronomers. While shorter and longer wavelength observations from the ground see through a transparent atmosphere, millimeter observations are plagued by a bright foreground that dominates the astrophysical signal by orders of magnitude. This signal must be removed in order to create maps of astrophysical emission.

? presented a summary of the techniques used to separate astrophysical and atmospheric signals in bolometric observations. The Bolocam observations reported here were conducted with a fast-scanning strategy that places the ‘fixed’ astrophysical emission at a different sampling frequency than the varying foreground atmosphere. This approach is one of the most efficient and flexible and has been used predominantly over alternatives like a nodding secondary in most recent large-scale observing campaigns.

While fast-scanning provides some separation between astrophysical and atmospheric signal, the atmospheric signal is still predominant and must be excised. Most approaches to removing atmospheric signal will also remove astrophysical signal with an angular scale comparable to the array. In order to recover signal on these large angular scales, the most commonly used approach for

bright Galactic signals is an iterative reconstruction process, in which a model of the astrophysical signal is subtracted from the observed timestream repeatedly. This process was first used by ?) and refined in ?).

This paper presents v2.0 of the Bolocam Galactic Plane Survey (BGPS). In Paper I (?), the initial processing of the BGPS v1.0 was described in detail. It was noted in Section 5 that there was a discrepancy between our survey and previously published results. This discrepancy raised the possibility of a flux calibration error in the Version 1 (hereafter v1.0) results. We resolve that discrepancy in Section ???. In Section ???, we discuss new observations included in the v2.0 data. Section ?? describes changes to the data reduction process and new data products. Section ?? and Section ?? measure the angular transfer function of the BGPS v2.0 pipeline and properties of extracted sources respectively. The paper concludes with a brief discussion of some simple results and a summary.

3.4 Calibration

3.4.1 Why was there a multiplicative offset in the v1.0 data release?

In ?), we reported that a ‘correction factor’ of about 1.5 on average was needed to bring our data into agreement with other 1 mm data sets. We discovered that the published v1.0 BGPS images have a different calibration reported in their FITS headers than was used in processing the data. The calibration used in the released data was borrowed from a previous observing run and differed from the pipeline-derived calibration by a factor ≈ 1.5 , completely explaining the discrepancy.

3.4.2 Comparing v1 and v2 calibration

We checked the data for consistency with the measured calibration offset. In order to compare flux densities in identical sources, we performed aperture photometry on the v2.0 data based on the locations of v1.0 sources using both the ‘source masks’ from Bolocat v1.0 (?) and circular

apertures centered on the Bolocat v1.0 peaks.

We measured the multiplicative offset between v1.0 and v2.0 by comparing these aperture-extracted fluxes. For each aperture size, we measured the best-fit line between the v1.0 and v2.0 data using a total least squares (TLS¹) method weighted by the flux measurement errors as reported in the catalogs. The agreement with $S_{\text{v}2.0} = 1.5 S_{\text{v}1.0}$, as expected based on Section ?? is generally within 10%, although the larger apertures show a slight excess with $S_{\text{v}2.0} \approx (1.6 - 1.7) S_{\text{v}1.0}$, which is expected from the improved extended flux recovery in v2.0 (see Section ??). The v2.0/v1.0 flux ratio is weakly dependent on the source flux, with generally higher v2.0/v1.0 ratios for brighter sources.

3.4.3 Comparison to Other Surveys

In Section 5.5 of ?), we compared the BGPS v1.0 data to other data sets from similar-wavelength observations. We repeat those comparisons here using the v2.0 data.

We compare to 3 data sets in the same ~ 1 mm atmospheric window. Two data sets from MAMBO II, the ?, M07) Cygnus X survey and the ?, R06) IRDC survey, overlap with the BGPS. The SIMBA 1.3 mm survey of the $\ell = 44$ region is the largest survey in the 1 mm band that overlaps with ours (?), M09).

The surveys we compare have different angular transfer functions. In order to account for the difference, we allow for a large angular scale offset between the observations. We fit a line of the form $y = mx + b$ to the data, where x and y represent the pixel values gridded to $7.2''$ pixels. The b value allows for a local offset. Since such an offset is unlikely to apply across the entire observed region, we also fit the offset for small sub-regions in the M07 and M09 data, focusing on DR21 and a region centered on G45.5+0.1 respectively.

The results of that comparison are displayed in Table ??, which includes the original comparison from ?)². BGPS v2 is in much better agreement with the other data sets than v1, but

¹ https://code.google.com/p/agpy/source/browse/trunk/agpy/fit_a_line.py, see also http://astroml.github.com/book_figures/chapter8/fig_total_least_squares.html

² In ?), there was a minor error in the table: M07 and M09 were swapped. This has been corrected in Table ??.

Table 3.1. Flux comparison with R06, M07, and M09

Comparison Survey	Pixels $> 3 \text{ MJy sr}^{-1}$		Pixels $> 10 \text{ MJy sr}^{-1}$		Pixels $> 20 \text{ MJy sr}^{-1}$		
BGPS v1	m	b	m	b	m	b	
R06	1.39	-2.00	1.46	-2.79	1.53	-4.77	
M07	1.51	4.13	1.44	13.78	1.36	27.45	
M07DR21	1.36	28.03	1.31	37.91	1.25	49.44	
M09	1.32	-0.22	1.25	4.94	1.21	9.88	
M09a	1.50	-5.15	1.51	-4.82	1.53	-5.11	

BGPS v2						
R06	1.05	3.67	1.02	5.03	1.00	7.05
M07	1.16	6.51	1.12	12.75	1.08	21.04
M07DR21	1.09	21.98	1.07	27.61	1.04	34.21
M09	0.73	1.33	0.69	6.75	0.66	13.45
M09a	0.96	-3.21	0.94	-0.69	0.89	2.91

The table values m and b are given for a linear fit of the form $y = mx + b$

it retains a significant additive offset, particularly with respect to MAMBO. The additive offset is explained by a difference in the angular transfer function; the MAMBO observing strategy of fast position switching allows structures on the scale of the array to be preserved, while Bolocam's fast-scan strategy does not. This also explains why there is an additive offset between Bolocam and MAMBO, but no such offset for SIMBA, which was used in a fast-scan mode similar to Bolocam. The differing backgrounds in different regions account for some of the remaining multiplicative difference. When individual sub-regions are compared, the additive and multiplicative offsets more clearly separate into independent components.

To enable flux density comparison between the surveys, we must account for the different spectral bandpasses of the instruments. The relative flux density measured between the instruments depends on the spectral index α_ν of the observed source; $\alpha_\nu = 2$ corresponds to a perfect black body on the Rayleigh-Jeans tail. In Table ?? we show the relative flux densities expected for Bolocam, MAMBO and SIMBA; they differ by at most 17% for spectral indices we expect to see. Bolocam flux densities are expected to be higher because it has a higher effective central frequency than either of the other instruments.

In ?), we measured Bolocam/MAMBO and Bolocam/SIMBA ratios in the range $0.66 < R < 0.83$, indicating a clear disagreement between the surveys. With the v2.0 data, we measure ratios $0.97 < R_{SIMBA} < 1.08$ and $0.89 < R_{MAMBO} < 0.99$. These numbers still indicate that the BGPS is too faint by $\lesssim 20\%$ relative to the expectations laid out in Table ??, but with a systematic calibration error no better than 20% in each survey, the agreement is reasonable.

3.5 Expansion of the BGPS and Observations

Thirteen nights of additional data were acquired from December 15th, 2009 to January 1st, 2010. The target fields and areas covered are listed in Table ?? as boxes in galactic latitude and longitude, with position angles to the galactic plane indicated. The original observations are described in Section 2 of ?).

The new target fields were selected from visual inspection of FCRAO OGS ^{12}CO integrated

Table 3.2. Relative flux expectation for Bolocam, MAMBO, and SIMBA given different input source spectral indices

α_ν	Bolocam/MAMBO	Bolocam/SIMBA
1.0	1.06274	1.06348
1.5	1.07926	1.08246
2.0	1.09746	1.10382
2.5	1.11448	1.12488
3.0	1.12877	1.14393
3.5	1.13962	1.1601
4.0	1.14685	1.17301
4.5	1.15057	1.18264
5.0	1.15108	1.18918

Response functions are computed using an atmospheric transmittance corresponding to 1 mm of precipitable water vapor

Table 3.3. Observations

Target	Longitude	Latitude	Longitude Size	Latitude Size	Position Angle
IRAS 22172	102.91	-0.64	1.67	1.07	0
l106	105.81	0.15	1.48	1.33	0
l111w	108.23	-0.43	3.35	2.78	0
l111n	110.50	2.18	4.19	2.21	0
l111s	111.07	-1.64	2.32	1.10	0
l119	119.40	3.08	3.29	0.83	330
l123	123.68	2.65	2.87	1.07	12
l126	125.70	1.93	1.06	1.08	0
l129	129.21	0.11	1.82	1.63	0
camob1	141.20	-0.31	2.79	3.40	0
l154	154.83	2.38	1.68	1.27	0
l169	169.42	-0.32	4.08	2.05	0
sh235	172.94	2.50	4.60	1.34	0
l181	181.11	4.40	2.19	1.20	0
l182	182.36	0.23	3.25	1.18	28
l195	195.92	-0.66	3.04	1.18	56
l201	201.57	0.30	1.32	1.37	0
ngc2264	202.97	2.21	2.20	1.32	0
orionBnorth	204.01	-11.86	2.17	1.33	335
orionB	206.73	-16.21	2.36	2.35	30
orionAspine	212.45	-19.24	4.35	2.48	0
monr2	213.54	-12.13	2.70	2.78	0
l217	217.69	-0.24	1.91	1.04	0

maps, ?) ^{12}CO maps, and IRAS 100 μm maps. The fields were selected primarily to provide even spacing in RA in order to maximize observing efficiency, and were therefore not blindly selected. However, selection on the basis of the presence of CO and hot dust emission should not be a significant bias - it is highly unlikely that any cold dust will be present in the absence of CO gas. A blind survey was more important in the inner galaxy, where the warm dust component is totally confused and essentially fills the inner ± 1 degree in latitude out to $\ell \sim 60^\circ$.

Additionally, the Orion A and B and Mon R2 clouds were observed in parallel observing campaigns by collaborators. These complexes are much closer than typical BGPS sources and their selection for mapping is very biased, but we include them in the archival data. Parts of the Orion A nebula remain proprietary as of this release, but are expected to be released upon publication of Kauffmann et al (in prep). The California nebula has also been observed and published in ?).

Finally, some archival CSO data was recovered and added to the BGPS. These data include maps of M16 and M17. M17 is an extraordinarily bright 1.1 mm source that was poorly covered in the BGPS because it is below $b = -0.5$.

The Bolocat cataloging tool was run on these new fields and they have been included in the v2.0 catalog. Some of their properties are displayed in Section ???. A total of 548 new sources not covered in the v1.0 survey were extracted.

3.6 Data Reduction and Data Products

3.6.1 Sky Subtraction

We compared a few different methods for atmospheric subtraction and astrophysical image reconstruction, but settled on an approach very similar to that used in v1.0. This subsection recounts the minor changes from v1.0 and explores some alternative approaches.

The PCA method (?) with iterative flux density restoration was used for v2.0 as for v1.0. In the PCA atmosphere removal method, the n eigenvectors corresponding to the highest values along the diagonal of the covariance matrix (the most correlated components) are nulled. We nulled

13 PCA components in both v1.0 and v2.0. The selection of 13 components produced the best compromise between uniform background noise and fully restored peak signal. Simulations show that the point source recovery is a very weak function of number of PCA components nulled (nPCA), while extended flux recovery is a strong function of nPCA. However, image artifacts including high-frequency correlated noise and low-angular-frequency blobs were substantially reduced with higher nPCA.

The iterative process adopts the positive flux density above some cutoff as a model of the astrophysical sky and subtracts that flux density from the timestream before repeating the atmospheric subtraction. This approach allows large angular scale structures to be recovered by removing them from the timestreams before they can contribute to the correlated signal. In v2.0, it was more successful than in v1.0 at removing negative bowls (see Section ??). Negative bowls are introduced because the atmospheric subtraction process assumes that the mean level of any timestream, and therefore any map, is zero; the iterative process allows this assumption to be violated, creating maps with net positive signal.

In the v1.0 data product, the median value at each time was subtracted before the PCA subtraction. We switched to an iterative median subtraction in v2.0, in which 80% of the median is subtracted from the timestream 5 times. The improvement from this process is minor, but it increased the stability of the pipeline (i.e., reduced the likelihood of spurious signal in the maps).

The quadratic planar fit sky subtraction method discussed in ?) was implemented for 1.1mm galactic plane data in the v2.0 pipeline. In principle, this method should do a substantially better job at removing smooth atmospheric signal from timestreams than PCA cleaning because it is based on a physically reasonable expectation of atmospheric variation. The spatial recovery was better than the aggressive 13-PCA approach, but as with the median and average subtraction approaches, a great deal of spurious signal from the atmosphere remained in the maps, and the noise properties were highly non-uniform, rendering source extraction difficult. It was also more computationally expensive and did not remove correlated electronic noise, which PCA subtraction did. The ?) approach is likely more effective at 143 GHz because the atmosphere is better-behaved at lower

frequencies. We speculate that it is also more effective for deep extragalactic fields in which more repeat observations of the same field are able to distinguish atmosphere from real signal on the angular scales of the array.

3.6.2 New Map Types

In the v2.0 data release, there are two new map types released: noise maps and median maps. A variant of the noise maps was produced in v1.0, while the median maps are an entirely new data product.

3.6.2.1 Noise Maps

Residual timestreams are automatically generated as part of the iterative map-making process. The residual is the result of subtracting the astrophysical model (which is smooth, noiseless, and positive) from the atmosphere-subtracted data timestream. The resulting timestream should only contain the remaining astrophysical noise. However, maps of the residual timestream contain sharp edge features because the astrophysical model is sharp-edged (i.e., transitions from 0 to a non-zero value from one pixel to the next).

We therefore created noise maps by taking the local standard deviation of the residual map. Pixels in the original map that were not sampled (i.e., represented by NaN in the FITS data file) are ignored when computing this local standard deviation and their values are set to be an arbitrarily high number (~ 100 Jy) such that pixels near the map edge are assumed to have extremely high noise (which is reasonable, since these pixels are affected by a variety of artifacts rendering them unreliable measurements of the true astrophysical flux). The local noise is computed within a $FWHM = 10$ -pixel gaussian, which enforces a high noise level within $\sim 2'$ of the map edge. This method produces reasonable noise maps (i.e., in agreement with the standard deviation calculated from blank regions of the signal map) and was used both within the iterative process and for cataloging.

3.6.3 Median Maps

Some artifacts (cosmic ray hits, instrumental artifacts) inevitably remained at the end of the process. In order to mitigate these effects, “median maps” were created. The value of each spatial pixel was set to the median value of the timestream points that intersected that pixel. The noise in the median maps was in some cases lower than that in the weighted mean maps, particularly for fields with fewer total observations. They uniformly have mitigated instrument-related artifacts such as streaking. These maps are released in addition to the weighted-mean maps, which often have higher signal-to-noise.

3.6.4 Pointing

In order to get the best possible pointing accuracy in each field, all observations of a given area were median-combined using the MONTAGE package, which performs image reprojections, to create a pointing master map (?). Each individual observation was then aligned to the master using a cross-correlation technique (?):

- (1) The master and target image were projected to the same pixel space
- (2) The images were cross-correlated and the peak pixel in the cross-correlation map identified
- (3) Sub-pixel alignment was measured by performing a 2nd-order Taylor expansion around the peak pixel

This method is similar to the version 1.0 method but improved by using MONTAGE to create the master images (which deals with reprojection better than IRAF), and the peak-finding method proved more robust than the previous gaussian fitting approach. The v1.0 gaussian fitting approach is often used in astronomy (e.g., <http://www.astro.ucla.edu/~mperrin/IDL/sources/subreg.pro>), but is biased when images are dominated by extended structure because the least-squares fitting approach will identify the broader peak that represents auto-correlation of astrophysical structure rather than correlation between the two images. In v1.0, we attempted to mitigate this

issue by subtracting off a ‘background’ component before fitting the gaussian peak, but this method was not robust.

The improved approach to pointing in general resulted in typical RMS offsets between the individual frames and the master of $\sim 2''$. The improvement in the point spread function is readily observed (see Section ??)

3.6.5 Pointing Comparison

We carefully re-examined the pointing throughout the BGPS using a degree-by-degree cross-correlation analysis between the v1.0, v2.0, and Herschel Hi-Gal $350\mu m$ data. The Herschel data were unsharp-masked (high-pass filtered) by subtracting a version of the data smoothed with a $\sigma = 120''$ gaussian. The result was then convolved with a $\sigma = 8.9''$ gaussian to match the beam sizes.

Errors on the offsets were measured utilizing the fourier scaling theorem to achieve sub-pixel resolution (inspired by ?). The errors on the best-fit shift were determined using errors estimated from the BGPS data and treating the filtered Hi-Gal data as an ideal model. The tools for this process, along with a test suite demonstrating their applicability to extended data, are publicly available at https://github.com/keflavich/image_registration.

The cross-correlation technique calculated the χ^2 statistic as a function of the offset. For a reference image Y and observed image X with error per pixel σ ,

$$\chi^2 = \sum \frac{(X - Y(dx, dy))^2}{\sigma^2}$$

where dx and dy are the pixel shifts. Because Y is not, in fact, an ideal model but instead is a noisy image, we increase σ by the rms of the difference between the aligned images, using a corrected $\sigma_c^2 = \sigma_{BGPS}^2 + RMS(X - Y(dx_b, dy_b))$, where dx_b, dy_b are the best-fit shifts.

For the majority of the examined 1-square-degree fields, the signal dominated the noise and we were able to measure the offsets to sub-pixel accuracy. A plot of the longitude / latitude offsets between v2.0 and v1.0 and Herschel Hi-Gal is shown in Figure ??.

Table ?? lists the measured offsets in arcseconds between images for all 1 degree fields from $\ell = 351$ to $\ell = 65$. The offsets represent the galactic longitude and latitude shifts in arcseconds from the reference (left) to the ‘measured’ field (right).

Table ?? shows the means of the columns in Table ??, weighted by the error in the measurements and by the number of sources. Weighting by the number of sources is used for comparison with other works that attempt to measure the pointing offset on the basis of catalog source position offsets. None of the measured offsets are significant; in all cases the scatter exceeds the measured offset.

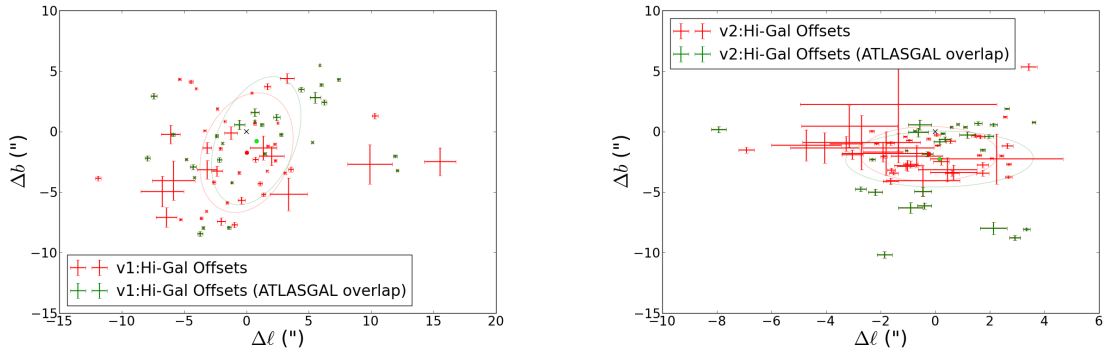


Figure 3.1 Plots of the latitude and longitude offsets of individual 1-degree fields in v1.0 (left) and v2.0 (right) as compared with Herschel Hi-Gal. Offsets were measured using a cross-correlation technique. The error bars correspond to $\Delta\chi^2 < 2.3$, or $1 - \sigma$ for Gaussian distributed noise and 2 degrees of freedom. The circles and ellipses represent the mean and standard deviation (unweighted) offsets in the whole survey (red) and the $(351 < \ell) \cup (\ell < 20)$ ATLASGAL-overlap regions (green). In both cases, the mean offset is consistent with zero, but many individual fields show significant offsets. Note that the scales are different; there are far fewer outliers in the v2-Herschel comparison (right) and the average offset is much closer to zero. The errors are larger in the non-ATLASGAL overlap region because there is less signal in the $35 < \ell < 65$ range.

Table 3.4. Cross-Correlation Offsets

Field Name	$\Delta\ell(\text{HG-v2})$	$\Delta b(\text{HG-v2})$	$\Delta\ell(\text{v1-v2})$	$\Delta b(\text{v1-v2})$	$\Delta\ell(\text{HG-v1})$	$\Delta b(\text{HG-v1})$	N(v1 sources)
l351	0.37 (-0.21)	-0.65 (0.21)	3.12 (-0.16)	1.83 (0.14)	-2.17 (-0.19)	-2.33 (0.19)	56
l352	1.10 (-0.07)	0.37 (0.07)	3.14 (-0.06)	1.45 (0.06)	-1.93 (-0.07)	-0.97 (0.07)	87
l353	3.35 (-0.13)	-8.07 (0.13)	-3.80 (-0.08)	-12.41 (0.08)	7.39 (-0.12)	4.30 (0.12)	65
l354	2.14 (-0.48)	-7.98 (0.50)	-3.71 (-0.11)	-12.04 (0.09)	5.51 (-0.43)	2.81 (0.44)	52
l355	2.92 (-0.20)	-8.78 (0.20)	-3.57 (-0.11)	-12.12 (0.09)	6.24 (-0.20)	2.42 (0.20)	54
l356	-0.62 (-0.37)	-0.06 (0.35)	-1.29 (-0.22)	-0.96 (0.17)	0.68 (-0.34)	1.58 (0.32)	42
l357	-0.56 (-0.43)	0.56 (0.41)	-0.06 (-0.24)	-0.39 (0.17)	-0.56 (-0.42)	0.56 (0.39)	23
l358	2.14 (-0.14)	0.56 (0.14)	-0.62 (-0.14)	0.17 (0.12)	2.78 (-0.14)	-0.25 (0.14)	35
l359	2.63 (-0.08)	1.90 (0.06)	-10.05 (-0.08)	5.86 (0.07)	12.10 (-0.10)	-3.21 (0.07)	248
1000	3.61 (-0.07)	0.77 (0.06)	-1.10 (-0.04)	1.55 (0.03)	5.30 (-0.07)	-0.89 (0.06)	318
1001	0.59 (-0.05)	0.37 (0.07)	-3.36 (-0.05)	1.31 (0.06)	11.92 (-0.16)	-2.02 (0.11)	368
1002	-0.39 (-0.26)	-6.13 (0.25)	1.46 (-0.24)	2.14 (0.19)	-1.41 (-0.15)	-7.93 (0.14)	170
1003	-2.73 (-0.21)	-4.75 (0.20)	0.62 (-0.18)	3.54 (0.17)	-3.46 (-0.10)	-7.96 (0.10)	243
1004	-1.86 (-0.28)	-10.18 (0.26)	-0.34 (-0.23)	0.11 (0.19)	-3.71 (-0.21)	-8.44 (0.19)	70
1005	1.18 (-0.29)	-0.28 (0.28)	-3.99 (-0.19)	-3.54 (0.19)	4.39 (-0.21)	3.49 (0.19)	78
1006	0.83 (-0.05)	0.60 (0.06)	-1.17 (-0.05)	-1.36 (0.06)	5.88 (-0.05)	5.48 (0.05)	109
1007	1.97 (-0.17)	-0.39 (0.16)	-4.50 (-0.09)	-4.50 (0.00)	6.00 (-0.12)	3.87 (0.11)	93
1008	1.58 (-0.14)	0.68 (0.16)	4.58 (-0.12)	1.43 (0.15)	-2.39 (-0.13)	-0.37 (0.15)	59
1009	1.74 (-0.10)	-1.52 (0.09)	6.15 (-0.09)	1.00 (0.09)	-4.82 (-0.08)	-2.29 (0.08)	55
1010	0.28 (-0.08)	-0.17 (0.08)	3.70 (-0.08)	1.98 (0.09)	-4.18 (-0.08)	-3.78 (0.07)	77
1011	-1.05 (-0.04)	-1.56 (0.04)	-0.94 (-0.03)	-0.04 (0.02)	-1.18 (-0.07)	-4.22 (0.08)	122
1012	-2.31 (-0.10)	-2.31 (0.10)	-3.80 (-0.08)	-0.70 (0.09)	1.49 (-0.09)	-1.83 (0.08)	102
1013	-0.75 (-0.05)	0.07 (0.05)	-1.49 (-0.05)	-0.59 (0.05)	0.66 (-0.05)	0.86 (0.06)	198
1014	-0.28 (-0.20)	-1.86 (0.20)	6.05 (-0.15)	-1.72 (0.16)	-5.88 (-0.15)	-0.25 (0.15)	137
1015	-2.19 (-0.26)	-5.01 (0.26)	5.79 (-0.17)	-2.64 (0.19)	-7.93 (-0.20)	-2.19 (0.20)	164
1016	-0.90 (-0.45)	-6.30 (0.45)	5.79 (-0.26)	-2.31 (0.28)	-4.28 (-0.25)	-2.92 (0.20)	63
1017	-0.45 (-0.32)	-4.95 (0.36)	-1.29 (-0.22)	-3.88 (0.26)	2.42 (-0.26)	1.18 (0.27)	62

Table 3.4 (cont'd)

Field Name	$\Delta\ell(\text{HG-v2})$	$\Delta b(\text{HG-v2})$	$\Delta\ell(\text{v1-v2})$	$\Delta b(\text{v1-v2})$	$\Delta\ell(\text{HG-v1})$	$\Delta b(\text{HG-v1})$	N(v1 sources)
l018	0.17 (-0.23)	-0.84 (0.21)	-1.07 (-0.17)	-1.97 (0.17)	1.24 (-0.15)	0.56 (0.14)	55
l019	-7.93 (-0.28)	0.17 (0.25)	0.89 (-0.11)	-2.69 (0.10)	-7.42 (-0.25)	2.92 (0.23)	179
l020	2.43 (-0.07)	-2.01 (0.08)	0.07 (-0.07)	-2.60 (0.06)	2.50 (-0.06)	0.70 (0.06)	110
l021	2.64 (-0.21)	-1.18 (0.21)	1.86 (-0.17)	-1.74 (0.16)	0.68 (-0.14)	0.68 (0.14)	103
l022	1.74 (-0.21)	-2.76 (0.21)	-0.65 (-0.16)	0.48 (0.14)	3.57 (-0.20)	-3.12 (0.20)	87
l023	2.69 (-0.12)	-3.75 (0.11)	-0.20 (-0.09)	-0.31 (0.08)	3.08 (-0.10)	-3.42 (0.10)	213
l024	2.70 (-0.09)	-2.70 (0.09)	-0.44 (-0.09)	-0.27 (0.08)	2.32 (-0.10)	-2.40 (0.10)	250
l025	1.62 (-0.08)	-1.95 (0.08)	0.08 (-0.07)	1.15 (0.07)	1.65 (-0.06)	-3.25 (0.07)	183
l026	1.66 (-0.15)	-0.42 (0.16)	0.06 (-0.12)	0.62 (0.13)	1.72 (-0.10)	-1.21 (0.11)	151
l027	1.46 (-0.15)	-0.34 (0.14)	-0.48 (-0.12)	0.87 (0.12)	2.28 (-0.10)	-1.04 (0.10)	119
l028	2.56 (-0.07)	1.21 (0.08)	6.22 (-0.07)	8.35 (0.07)	-3.63 (-0.11)	-7.17 (0.12)	188
l029	-0.96 (-0.11)	-0.73 (0.11)	4.58 (-0.09)	6.38 (0.09)	-5.27 (-0.09)	-7.27 (0.09)	177
l030	0.06 (-0.11)	-0.28 (0.12)	2.05 (-0.09)	3.23 (0.11)	-3.21 (-0.07)	-6.58 (0.06)	276
l031	-1.10 (-0.06)	-0.42 (0.05)	-1.69 (-0.03)	-1.46 (0.02)	0.44 (-0.07)	3.19 (0.07)	354
l032	-0.24 (-0.08)	-0.60 (0.09)	1.18 (-0.08)	-2.42 (0.08)	-2.33 (-0.09)	1.88 (0.08)	189
l033	2.07 (-0.05)	-2.21 (0.05)	6.10 (-0.06)	-5.71 (0.06)	-4.04 (-0.06)	3.56 (0.06)	210
l034	-2.32 (-0.09)	0.04 (0.08)	-0.46 (-0.05)	-0.10 (0.05)	-1.55 (-0.11)	-5.88 (0.10)	203
l035	-1.88 (-0.12)	-2.05 (0.12)	0.31 (-0.11)	-0.59 (0.10)	-2.08 (-0.13)	-1.41 (0.12)	247
l036	-1.63 (-0.14)	-0.96 (0.15)	0.82 (-0.12)	3.01 (0.11)	-2.62 (-0.14)	-4.19 (0.14)	126
l037	-1.07 (-0.32)	-2.87 (0.29)	-2.31 (-0.25)	0.51 (0.24)	0.73 (-0.23)	-2.31 (0.21)	83
l038	-1.60 (-0.15)	-3.18 (0.17)	-0.79 (-0.12)	0.34 (0.14)	-0.59 (-0.11)	-3.40 (0.12)	69
l039	0.62 (-0.26)	-3.43 (0.24)	-0.23 (-0.16)	1.12 (0.14)	1.10 (-0.19)	-4.30 (0.17)	69
l040	1.74 (-0.23)	-3.43 (0.24)	1.86 (-0.18)	2.98 (0.17)	1.38 (-0.17)	-5.20 (0.16)	40
l041	0.23 (-0.29)	-2.48 (0.29)	1.07 (-0.24)	5.23 (0.20)	-0.96 (-0.23)	-7.70 (0.23)	44
l042	-1.01 (-0.48)	-2.81 (0.45)	0.11 (-0.26)	5.06 (0.23)	-2.02 (-0.34)	-7.42 (0.29)	36
l043	0.08 (-0.10)	-1.15 (0.09)	2.07 (-0.08)	-2.52 (0.09)	-1.74 (-0.07)	0.84 (0.05)	17
l044	-1.63 (-0.29)	-4.11 (0.27)	4.78 (-0.26)	-8.16 (0.20)	-4.44 (-0.17)	4.11 (0.15)	27

3.6.6 ATLASGAL offset

?) performed a comparison of the Bolocam and ATLASGAL catalogs, identifying a systematic offset between the catalogs of $\Delta\ell = -4.7''$, $\Delta b = 1.2''$. Because the offset is measured between catalog points, the meaning of this measured offset is not immediately clear. In the BGPS maps in the ATLASGAL-BGPS overlap region, there were 12 individual sub-regions that could have independent pointing. Because we did not have direct access to the ATLASGAL maps or catalog, we compared the Bolocam v1.0 and v2.0 catalogs to each other determine whether the pointing changes in v2.0 might account for the observed ATLASGAL offset, assuming that the v2.0 pointing is more accurate than the v1.0 pointing.

We performed an inter-catalog match between v1.0 and v2.0, considering sources between the two catalogs to be a match if the distance between the centroid positions of the two sources is $< 40''$ (this distance is more conservative than that used in Section ??). We then compared the pointing offset as measured by the mean offset between the catalogs to the offset measured via cross-correlation analysis of the maps on a per-square-degree basis. The catalog and image offsets agree well, with no clear systematic offsets between the two estimators. The scatter in the catalog-based measurements is much greater, which is expected since the source positions are subject to spatial scale recovery differences between the versions and because the sources include less signal than the complete maps.

There is no clear net offset between either version of the BGPS and the Herschel Hi-Gal survey, or between the two versions of the BGPS. However, the scatter in the pointing offsets between v1.0 and Herschel is substantially greater than the v2.0-Herschel offsets. The offset measured in ?) is likely a result of particularly large offsets in a few fields with more identified sources. As shown in Table ??, the mean offset, **weighted by number of sources**, is greater for the ATLASGAL overlap region than overall. We reproduce a number similar to the ATLASGAL-measured longitude offset of $\Delta\ell = -4.7''$ (our source-count-weighted $\Delta\ell = -3.7''$), despite a much larger standard deviation and despite no significant offset being measured directly in the images.

Table 3.4 (cont'd)

Field Name	$\Delta\ell(\text{HG-v2})$	$\Delta b(\text{HG-v2})$	$\Delta\ell(\text{v1-v2})$	$\Delta b(\text{v1-v2})$	$\Delta\ell(\text{HG-v1})$	$\Delta b(\text{HG-v1})$	N(v1 sources)
l045	-1.52 (-0.16)	-3.43 (0.15)	4.42 (-0.14)	-7.73 (0.12)	-5.36 (-0.10)	4.32 (0.09)	30
l046	-0.90 (-0.27)	-2.70 (0.27)	-1.24 (-0.26)	-5.29 (0.21)	1.69 (-0.25)	3.71 (0.25)	53
l047	0.68 (-0.85)	-3.38 (0.63)	0.34 (-0.38)	-3.71 (0.27)	3.26 (-0.56)	4.39 (0.41)	11
l048	-0.45 (-1.35)	-4.05 (1.31)	8.16 (-0.27)	-3.32 (0.30)	-6.08 (-0.76)	-0.23 (0.76)	6
l049	-2.15 (-0.08)	-1.00 (0.08)	-0.35 (-0.05)	-0.75 (0.06)	-3.35 (-0.09)	0.08 (0.05)	113
l050	0.56 (-0.18)	-0.79 (0.19)	1.77 (-0.14)	-0.14 (0.12)	-0.73 (-0.06)	-12.66 (0.30)	31
l051	-1.91 (-0.73)	-1.69 (0.82)	4.95 (-0.23)	0.45 (0.32)	-3.15 (-0.36)	-1.35 (0.45)	9
l052	-2.70 (-2.16)	-0.90 (2.25)	-3.71 (-0.54)	3.26 (0.21)	3.38 (-1.51)	-5.18 (1.35)	0
l053	-3.04 (-0.39)	-1.91 (0.38)	-1.01 (-0.28)	2.59 (0.19)	-0.39 (-0.30)	-5.68 (0.28)	26
l054	-3.26 (-0.60)	-1.01 (0.61)	1.35 (-0.27)	1.35 (0.18)	-2.36 (-0.45)	-3.26 (0.43)	26
l055	-4.05 (-1.26)	-1.35 (1.26)	-0.23 (-0.34)	1.58 (0.23)	-3.15 (-0.81)	-3.15 (0.76)	4
l056	-4.72 (-1.28)	-1.12 (1.28)	4.39 (-0.44)	-0.79 (0.24)	-1.24 (-0.53)	-0.11 (0.53)	10
l057	-3.15 (-1.76)	0.45 (1.71)	2.81 (-0.50)	0.11 (0.21)	1.35 (-1.08)	-1.35 (0.99)	1
l058	-1.35 (-1.30)	-1.35 (1.22)	-6.86 (-0.48)	0.79 (0.25)	2.02 (-0.99)	-2.02 (0.79)	4
l059	0.45 (-1.08)	-3.15 (0.99)	-4.28 (-0.23)	1.12 (0.68)	-6.75 (-1.71)	-4.95 (1.26)	2
l060	3.43 (-0.29)	5.34 (0.29)	-7.09 (-0.14)	4.61 (0.17)	10.30 (-0.24)	1.29 (0.23)	17
l061	-6.92 (-0.29)	-1.52 (0.23)	5.12 (-0.16)	3.54 (0.16)	-11.89 (-0.23)	-3.85 (0.19)	4
l062	-1.80 (-1.62)	-1.80 (1.80)	4.72 (-0.18)	5.18 (0.25)	-5.85 (-1.71)	-4.05 (1.62)	1
l063	-0.68 (-0.95)	-2.02 (0.88)	2.64 (-0.18)	4.67 (0.27)	-6.41 (-0.83)	-7.09 (0.81)	5
l064	2.25 (-2.43)	-2.25 (2.07)	-24.98 (-0.43)	-2.92 (0.83)	15.52 (-1.26)	-2.48 (1.15)	1
l065	-1.35 (-3.60)	2.25 (3.82)	-24.08 (-0.63)	-4.28 (0.99)	9.90 (-1.80)	-2.70 (1.62)	1

Table 3.5. Cross-Correlation Offset Means and Standard Deviations

	$\Delta\ell(\text{HG-v2})$	$\Delta b(\text{HG-v2})$	$\Delta\ell(\text{v1-v2})$	$\Delta b(\text{v1-v2})$	$\Delta\ell(\text{HG-v1})$	$\Delta b(\text{HG-v1})$
Mean	0.23	-1.8	0.16	-0.37	-0.0047	-1.7
Standard Deviation	2.2	2.5	5.3	3.9	4.9	3.7
Weighted Mean	-0.47	-0.89	0.26	-1.1	-0.089	-0.87
Weighted Standard Deviation	1.7	1.8	3.1	3.5	4	3.6
N(src) Weighted Mean	-0.24	-1.1	0.26	0.58	-1.3	-1.9
N(src) Weighted Standard Deviation	2.3	2.1	3.5	3.2	5.7	3.6
N(src) Weighted Mean $\ell < 21$	-0.24	-1	1.5	0.84	-3.7	-1.9
N(src) Weighted Standard Deviation $\ell < 21$	2.9	2.8	4.1	3.2	7.3	3.4

These measurements imply that the pointing offset measured by ?) was localized to a few fields and that the offset is corrected in the v2.0 data.

3.7 The Angular Transfer Function of the BGPS

3.7.1 Simulations with synthetic sky and atmosphere

In order to determine the angular response of the Bolocam array and BGPS pipeline in realistic observing conditions, we performed simulations of a plausible synthetic astrophysical sky with synthetic atmospheric signal added to the timestream.

To generate the simulated atmosphere, we fit a piecewise power law to a power spectrum of a raw observed timestream (Figure ??). The power spectrum varies in amplitude depending on weather conditions and observation length, but the shape is generally well-represented by $1/f$ (pink) noise $P \propto \nu^{-1.5}$ for $\nu < 2$ Hz and white noise $P \sim \text{const}$ for $\nu \geq 2$ Hz where ν is the frequency. We show a fitted timestream power spectrum in Figure ???. The deviations from $1/f$ and white noise have little affect on the reduction process.

The Fourier transform of the atmosphere timestream is generated by applying noise to the fitted power spectrum. The power at each frequency is multiplied by a random number sampled from a gaussian distribution with width 1.2, determined to be a reasonable match to the data, and mean 1.0^3 . The resulting Fourier-transformed timestream is $FT(ts) = (r_{\nu 1} P_f)^{1/2} + i(r_{\nu 2} P_f)^{1/2}$, where r_1 and r_2 are the normally distributed random variables and P_f is the fitted power-law power spectrum. The atmosphere timestream is then created by inverse Fourier transforming this signal.

Gaussian noise is added to the atmospheric timestream of each bolometer independently, which renders the correlation between timestreams imperfect. This decorrelation is important for the PCA cleaning, which would remove all of the atmosphere with just one nulled component if the correlation was exact. The noise level set in the individual timestreams determines the noise level in the output map.

³ We experimented with different noise distributions that reasonably matched the data, including a lognormal distribution, and found that the angular transfer function was highly insensitive to the noise applied to the atmosphere time series power spectrum.

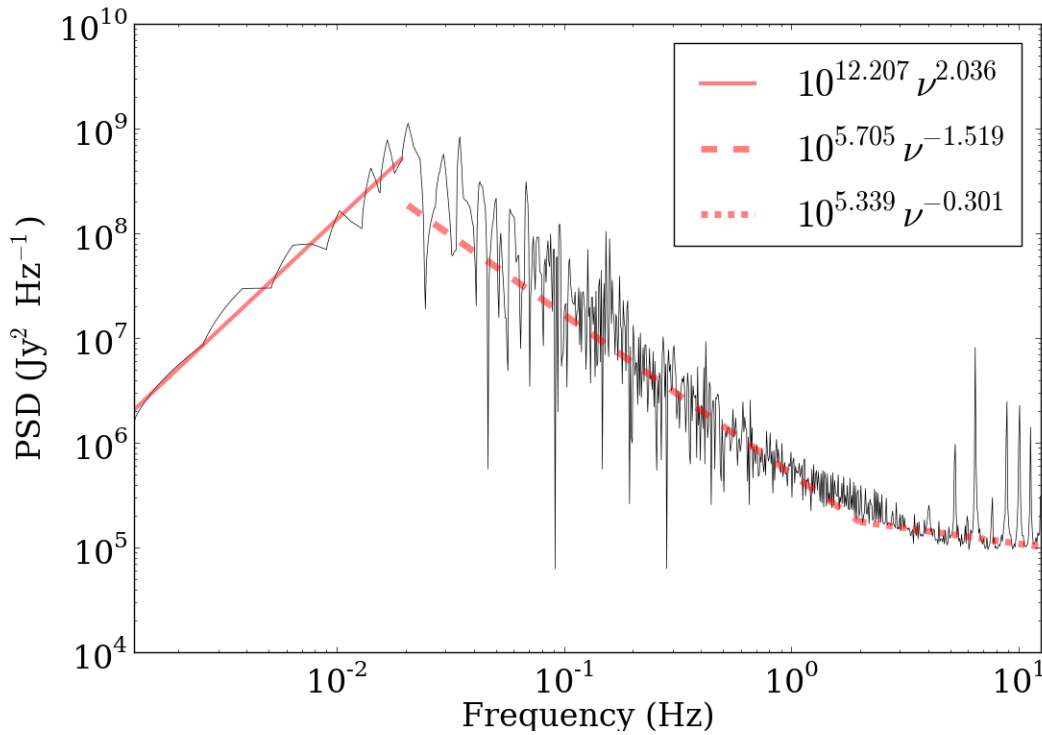


Figure 3.2 Fit to the power spectrum of a ~ 30 minute observation. Three independent power laws are fit to the data, with a fixed break at 0.02 Hz (below which the AC sampler removes signal) and a fitted break at higher frequency, near 2 Hz, where the power spectrum flattens towards white noise. The beam FWHM is at about 4 Hz using the standard scan rate of $120'' \text{ s}^{-1}$.

3.7.1.1 Simulated Map Parameters

We simulated the astrophysical sky by randomly sampling signal from a circularly symmetric 2D power-law distribution in Fourier space. The power distribution as a function of angular frequency is given by

$$P(1/r) \propto (1/r)^{-\alpha_{ps}} \quad (3.1)$$

where r is the angular size-scale and α_{ps} is the power-law spectral index for power spectra. We modeled this signal using power spectrum power-law indices ranging from -3 to +0.5; in the HiGal $\ell = 30$ Science Demonstration Phase (SDP) field, the power-law index measured from the 500 μm map is $\alpha_{ps} \sim 2$ (see Section ??). The data were smoothed with a model of the instrument PSF to simulate the telescope's aperture and illumination pattern. For each power-law index, four realizations of the map using different random seeds were created. The signal map was then sampled into timestreams with the Bolocam array using a standard pair of perpendicular boustrophedonic scan patterns. Examples of one of these realizations with identical random numbers and different power laws are shown in Figure ??.

3.7.2 The Angular Transfer Function

We used a subset of these power-law simulations to measure the amount of recovered signal at each angular (spatial) scale. For each power-law in the range $2 < \alpha_{ps} < 1$, which best match the Herschel 500 μm power-spectra, we used five different realizations of the map to measure the angular transfer function, defined as $STF(f) = F_{out}(f)/F_{in}(f)$ where f is the angular frequency, F_{out} is the azimuthally averaged power-spectrum of the pipeline-processed map, and F_{in} is the azimuthally averaged power-spectrum of the simulated input map.

The angular transfer function shows only weak dependence on the ratio of astrophysical to atmospheric power, and is approximately constant at $\sim 95\%$ recovery over the range of angular scales between the beam size and $\sim 2'$. The angular transfer function is shown in Figure ???. At larger angular scales, in the range $2' - 8'$, the recovery is generally low. Our simulations included the

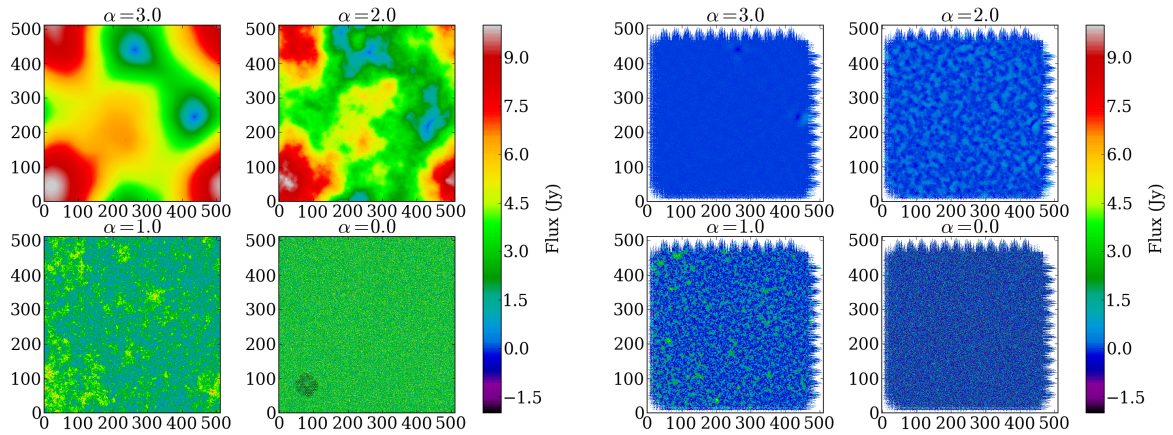


Figure 3.3 Examples of input (top) and output (bottom) maps for different input power-spectrum power law α_{ps} values. For very steep power laws, most of the power is on the largest scales. $\alpha_{ps} = 0$ is white noise. The axis scales are in pixels, where each pixel is $7.2''$, so each field is approximately 1° on a side. The Bolocam footprint is plotted in the lower-right panel of the top figure as an indication of the largest possible recovered angular scales. The input images are normalized to have the same **peak** flux density. The pipeline recovers no emission from the simulation with $\alpha_{ps} = 3$, but this value of α_{ps} is not representative of the real astrophysical sky - Herschel sees structure with $\alpha_{ps} \lesssim 2$, and the BGPS detected a great deal of astrophysical signal (see Section ?? and Figure ??).

full range of observed astrophysical to atmospheric flux density ratios, from $\sim 10^{-2}$ for the Central Molecular Zone (CMZ) down to $\sim 10^{-4}$ for sparsely populated regions in the $\ell \sim 70$ region.

?) perform a similar analysis for the SCUBA-2 pipeline. Our transfer function (Figure ??) cuts off at a scale $\sim 1/6$ the SCUBA-2 scale. While the angular extent of the Bolocam footprint is only slightly smaller than SCUBA-2's, some feature of the instrument or pipeline allows SCUBA-2 to recover larger angular scales. We speculate that the much larger number of bolometers in the SCUBA-2 array allows the atmosphere to be more reliably separated from astrophysical and internal electrical signals, so the SCUBA-2 pipeline is able to run with an atmosphere subtraction algorithm less aggressive than the 13-PCA approach we adopted.

3.7.3 Comparison with other data sets

Given an understanding of the spatial transfer function, it is possible to compare the BGPS to other surveys, e.g. Hi-Gal, ATLASGAL, and the JCMT Galactic Plane Survey (JPS), for temperature and beta measurements.

Because the systematic uncertainties in temperature/beta derivation from dust SEDs are severe (e.g. ???), we recommend a conservative approach when comparing BGPS data with other data sets. For compact sources, aperture extraction with background subtraction in both the BGPS and other data set should be effective. In Figure ??, we show the results of aperture extraction with and without background subtraction on a simulated power-law generated image with $\alpha_{ps} = 1$. The scatter between the flux density measurements derived from the input simulated sky map and the iteratively produced map is small, $\sim 5\%$, when background subtraction is used.

The agreement between the flux densities extracted from the iterative map and the input synthetic map is excellent for $40''$ diameter background-subtracted apertures. For these apertures, the RMS of the difference between the iterative map and the input map fluxes is $\sigma = 0.06$ when background subtraction is used, indicating the utility and necessity of this approach. The agreement is good for larger apertures, including the largest ($120''$) diameter used in bolocat, albeit with slightly more scatter $\sigma = 0.75$ and a small systematic bias. To correct for the systematic bias,

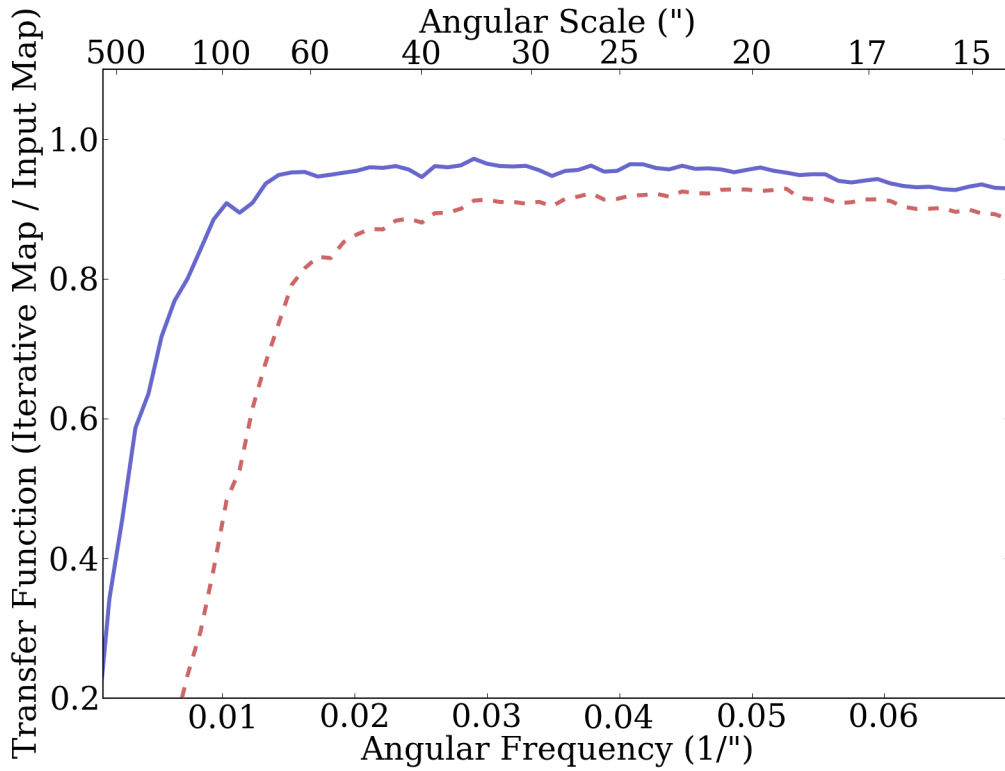


Figure 3.4 The angular transfer function over the range of angular scales where the BGPS data are reliable after 20 iterations (blue) and without iterative mapping (red dashed). At higher angular frequency (smaller angular scale), the beam smooths out any signal. At lower angular frequency, the atmospheric subtraction removes signal. The benefits of iterative mapping in recovered flux density on all scales, but particularly the improvement in large-scale recovery, are evident.

the $120''$ aperture flux densities should be scaled up by a correction factor $CF_{120''} = 1.13 \pm 0.02$. However, the offset is not very well represented by a simple multiplicative scaling because the extracted fluxes are background-dependent, so when using the $120''$ apertures, one should include a systematic uncertainty of $\sim 5\%$ in addition to the error in the multiplicative correction.

In order to compare extended structures, a different approach is required. The safest approach is to “unsharp mask” (high-pass-filter) both the BGPS and the other data set with a gaussian kernel with FWHM $\lesssim 120''$ ($\sigma \lesssim 51''$). The filtering will limit the spatial dynamic range, but will provide accurate results over the angular scales sampled.

Direct comparison of power spectra over the reproduced range is also possible. A demonstration of this approach is given in Figure ???. The BGPS power spectrum has a shape very similar to that of HiGal. The spectral index is a commonly used measure of the ratio between flux densities at two different wavelengths in the radio,

$$\frac{F_1}{F_2} = \left(\frac{\lambda_1}{\lambda_2} \right)^{-\alpha_\nu} = \left(\frac{\nu_1}{\nu_2} \right)^{\alpha_\nu} \quad (3.2)$$

The spectral index between the BGPS at 1.1 mm and Herschel at $500 \mu m$ is $\alpha_\nu \approx 3.7$ over the range $33'' < dx < 300''$. On the Rayleigh-Jeans tail, $\alpha_\nu = \beta + 2$, so this spectral index is consistent with typical dust emissivity index β measurements in the range $1.5 < \beta < 2$.

3.7.4 Power Spectral Density comparison

In Section ??, we showed the power spectral density of the Bolocam and Herschel Hi-Gal observations of the $\ell = 30^\circ$ field. Over the range in which the Bolocam and Herschel data are both sensitive, the data are consistent with a $500 \mu m$ - $1100 \mu m$ spectral index $\alpha_\nu \sim 3.7$, or $\beta \gtrsim 1.7$ depending on the temperature. This measurement suggests that structures over a range of spatial scales (0.5-6 pc in the $\ell = 30^\circ$ region) have similar dust emissivity properties.

Changes in the spectral index as a function of angular scale are evident when comparing to shorter wavelengths (250 and $350 \mu m$; Figure ??). This variation indicates that either temperature or emissivity is scale-dependent. If dust emissivity (or opacity, i.e. κ_ν , the dust absorption

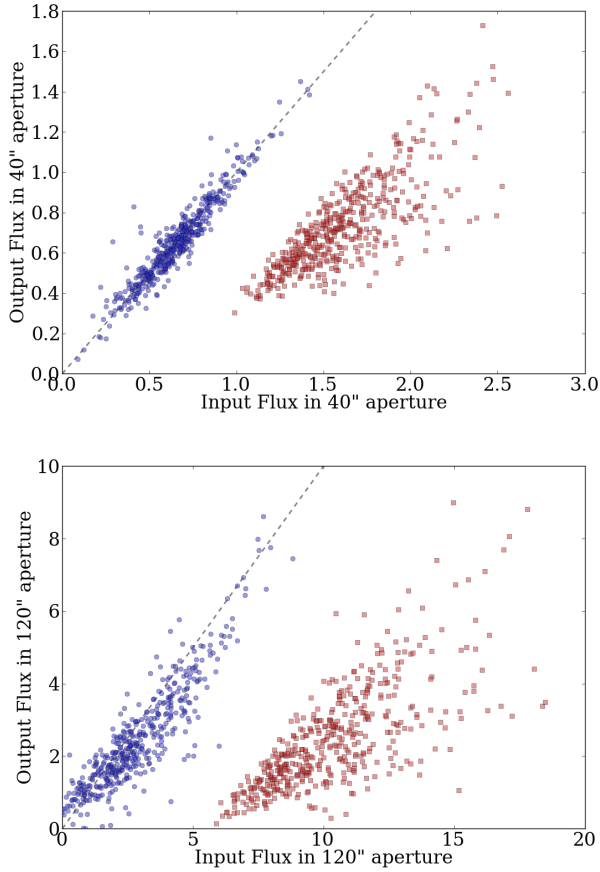


Figure 3.5 The aperture-extracted flux densities in a simulated map. The X-axis shows the flux density of the source in the input map with (blue circles) and without (red squares) the flux density averaged in a background annulus subtracted. The black dashed line is the 1-1 line.

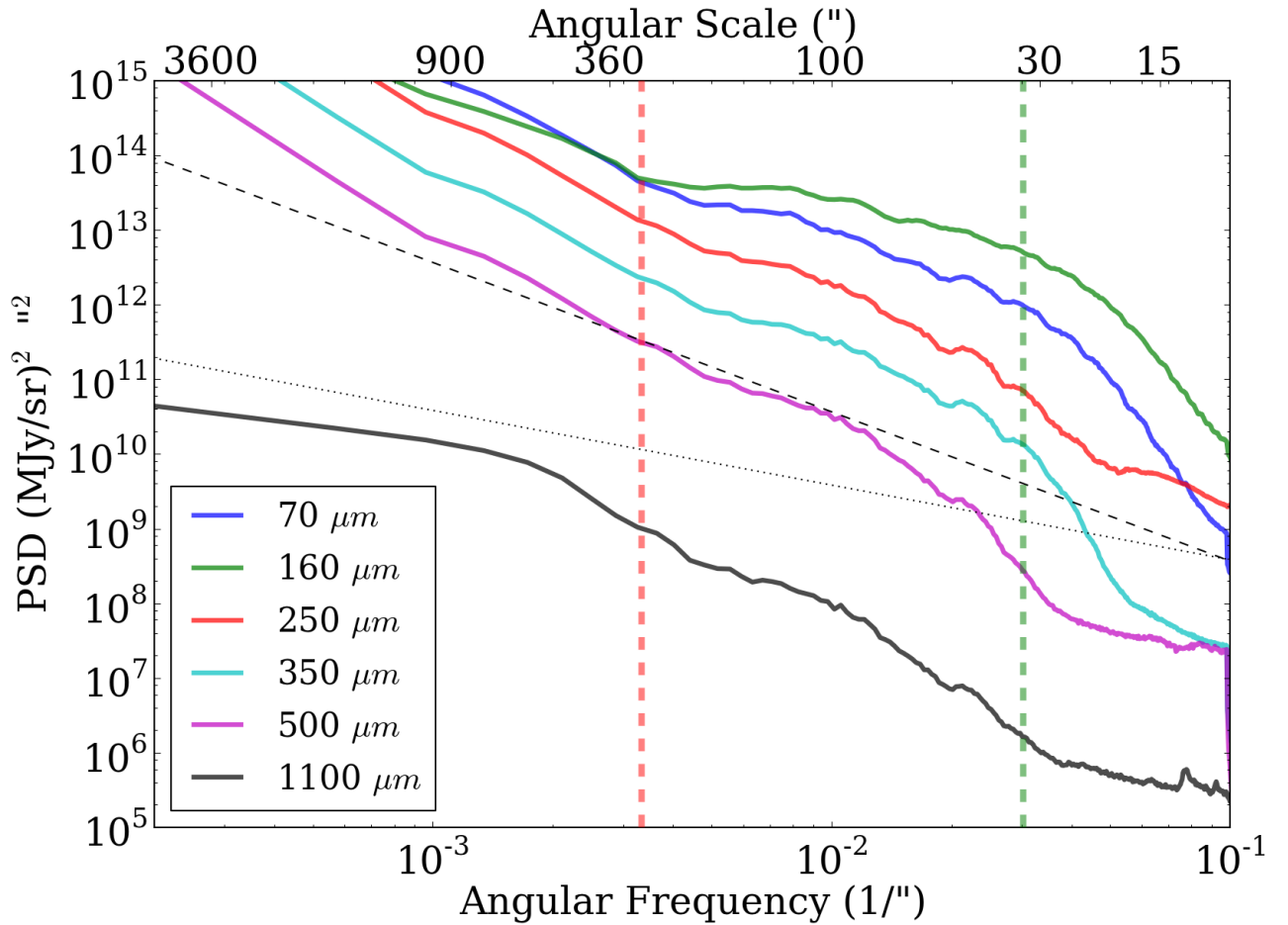


Figure 3.6 A comparison of the power spectra of the $\ell = 30$ HiGal SDP fields with the BGPS power spectrum covering the same area. The area included is 1 square degree. The dashed and dotted black lines indicate power laws with $\alpha_{ps} = -2$ and $\alpha_{ps} = -1$ respectively, with arbitrary normalizations, as a guide for comparison. The vertical dashed red and green lines indicate the large angular scale 50% recovery point of the BGPS and the BGPS beam FWHM respectively. The ratio of $500 \mu\text{m}$ to $1100 \mu\text{m}$ in this example has a spectral index $\alpha_\nu \sim 3.7$. Note that the $500 \mu\text{m}$ power begins falling off more steeply at $\sim 40''$ because the Herschel FWHM beam size is $36''$, slightly larger than Bolocam's.

coefficient) varies with scale, the lowest emissivity (opacity) is on the largest angular scales. If the variation is caused by differing temperatures at different angular scales, which is very likely, the smallest structures exhibit the highest temperatures in the $\ell = 30$ region, implying that, at least in this region, internal heating dominates external.

3.8 Examination of BGPS and HiGal power-spectra

We measured the power spectral density of both the Herschel Hi-Gal images and the BGPS images on a per-square-degree basis as described in Section ???. The spectral indices reveal interesting details about some regions of the Galactic Plane.

The dust spectral index is sensitive to both the temperature, which controls the location of the blackbody peak, and the dust opacity power-law index β , which controls the Rayleigh-Jeans slope. Depending on the properties of the dust, it may be possible to constrain one parameter or the other. For high temperatures, $T \gtrsim 30$ K, the Herschel SPIRE and BGPS wavelengths are firmly on the Rayleigh-Jeans (RJ) tail, and therefore can be used to tightly constrain the slope of the RJ tail or the β index. For lower temperatures, with λ_{max} near one of the SPIRE wavelengths, the spectral indices constrain T but provide only weak constraints on β (though β measurements could be obtained by comparison with $850\ \mu m$ measurements from ATLASGAL or SCUBA-2).

To measure temperature and opacity properties, we show the allowed $T-\beta$ parameter space for the measured spectral indices in two regimes: small angular scale ($40'' < dx < 100''$, selected to avoid the $500\ \mu m$ beam at $36''$) and large angular scale ($100'' < dx < 300''$). These two regimes are notably different in Figure ???, showing the short-wavelength spectral indices rising towards smaller angular scales while $\alpha_{500\mu m}$ remains flat down to the Herschel beam size. In Figure ???, we show the parameter space allowed by the full range of the spectral index measurements in these regimes. Small angular scales only have a lower-limit on temperature $T \gtrsim 20$ K and a reasonably narrow constraint on beta $1.8 \lesssim \beta \lesssim 2.3$. Large angular scales, however, have a temperature $15 < T < 25$ K and beta $2.1 \lesssim \beta \lesssim 2.6$.

For some regions, in particular the Galactic Center, no valid regions of $T-\beta$ parameter space

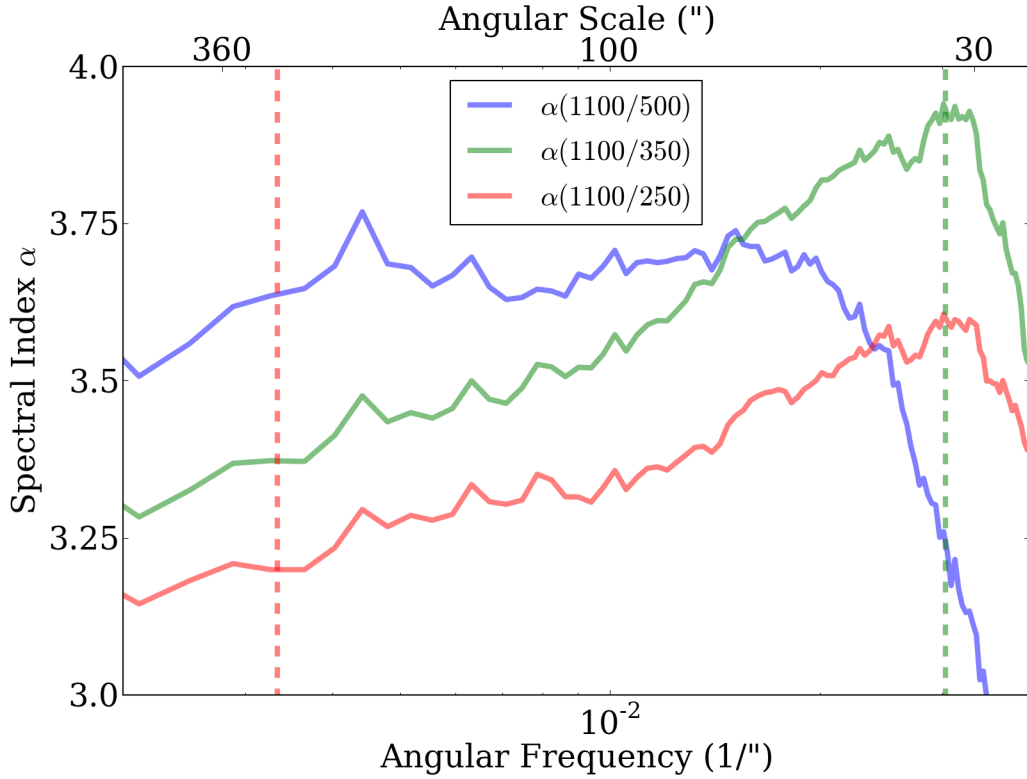


Figure 3.7 The ‘spectral index’ α_{nu} between the BGPS and the three Herschel-SPIRE bands as a function of angular scale. This figure shows the power spectrum ratio for the $\ell = 30$ 1-square degree field.

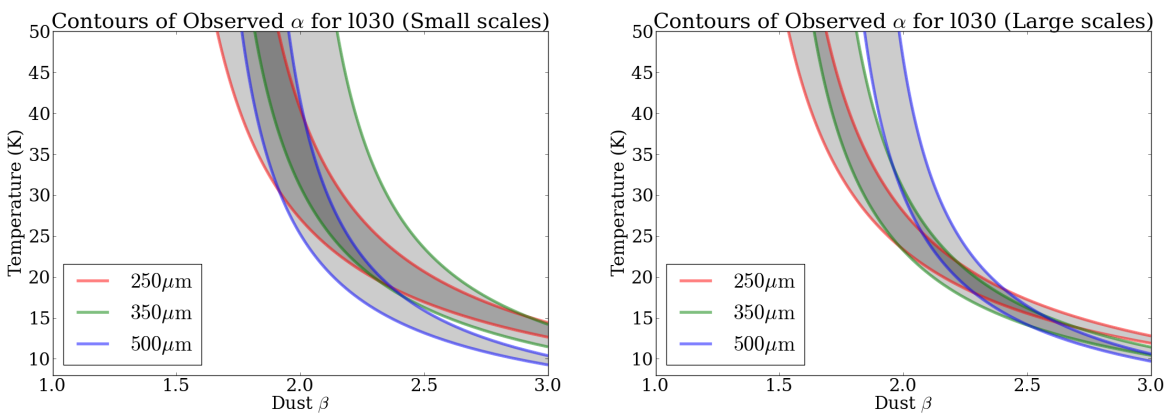


Figure 3.8 Contours of the ‘spectral index’ α_ν between the BGPS and the three Herschel-SPIRE bands on scales 40-100'' (left) and 100-300'' (right) for the $\ell = 30$ 1-square degree field.

are allowed; in that specific case, at least, the prevalent synchrotron and free-free emission likely dominates the spectral indices.

For $\ell \gtrsim 45$, the constraints on beta tend toward upper limits at both large and small scale as the spectral indices get shallower. While there are exceptions for some 1-square-degree fields, for these regions beta is constrained to be $\beta \lesssim 2$ for large scales and $\beta \lesssim 1.8$ for small scales. In the inner galaxy, $\ell < 45$, more typically $2 \lesssim \beta$ on large scales, and β is more often larger on small scales.

These values are consistent with larger **spatial** scales having steeper β , since the same **angular** scale probes a larger **spatial** scale at $\ell < 45$ because the distance to the bulk of the emission is greater in the inner galaxy on average.

3.9 Source Extraction

?) presented the Bolocat catalog of sources extracted from the v1.0 data with a watershed decomposition algorithm. We have used the same algorithm to create a catalog from the v2.0 catalog. We have also performed comparisons between the v1.0 and v2.0 data based on the extracted sources. The new catalog was derived using the same Bolocat parameters as in v1.0. This catalog includes regions that were not part of the v1.0 survey area, but we restrict our comparison between v1.0 and v2.0 to the area covered by both surveys.

3.9.1 Catalog Matching between v1.0 and v2.0

We matched the v1.0 and v2.0 catalogs based on source proximity. For each source in v1.0, we identified the nearest neighbor from v2.0, and found that 5741 v2.0 sources are the nearest neighbor for a v1.0 source out of 8004 v2.0 sources in the v1.0-v2.0 overlap region. Similarly, we identified the nearest neighbor in v1.0 for each v2.0 source, finding 5745 v1.0 sources are the nearest neighbor for a v2.0 source out of 8358 v1.0 sources. There are 5538 v1.0-v2.0 source pairs for which each member of the pair has the other as its nearest-neighbor. These sources are clearly reliable and stable source identifications and constitute about 70% of the v2.0 sample.

Most of the unmatched sources have low flux density (Figure ??), but some were significantly higher - these generally represent sources that were split or merged going from v1.0 to v2.0. A few examples of how mismatches can happen are shown in Figures ?? and ?? . The low-flux-density sources were most commonly unmatched in regions where the noise in v1.0 and v2.0 disagreed significantly. The high-flux-density mismatches tend to be different decompositions of bright sources and are preferentially found near very bright objects, e.g. in the Galactic Center region.

3.9.2 Source flux density, size, shape, and location distributions

We reproduce parts of ?) Figures 17 and 19 as our own Figures ?? and ?? . These figures show the distributions of extracted source properties (flux density, size, and aspect ratio) for the v1.0 and v2.0 data. The source flux density distributions above the completeness cutoff are consistent between v1.0 and v2.0, both exhibiting power-law flux density distributions

$$\frac{dN}{dS_\nu} \propto S_\nu^{-\alpha_{src}} \quad (3.3)$$

with values in the range $\alpha_{src} = 2.3 - 2.5$ for sources with $S_\nu \gtrsim 0.5$ Jy. The v2.0 data include more large sources. In the left panel of Figure ?? , we have included the v2.0 aperture-extracted data both with and without annular background subtraction; the v1.0 catalog had no background subtraction performed, but the v2.0 catalog has had background subtraction performed.

The longitude and latitude source flux density distribution plots, Figure 15 of ?), are reproduced in Figure ?? . The properties are generally well-matched, although even with the $1.5 \times$ correction factor to the v1.0 data, there is more flux density per square degree in v2.0 sources. The gain in flux density recovery is both because of an increased flux density recovery on large angular scales and because of improved noise estimation, which results in a greater number of pixels being included in sources (see Section ?? for more details and Figures ?? and ?? for examples).

A two-dimensional histogram is shown in Figure ?? . The ratio of source counts per half square degree is included in panel 3. This figure illustrates that two catalog versions are broadly consistent, and the regions in which they differ significantly tend to have fewer sources. The most extreme

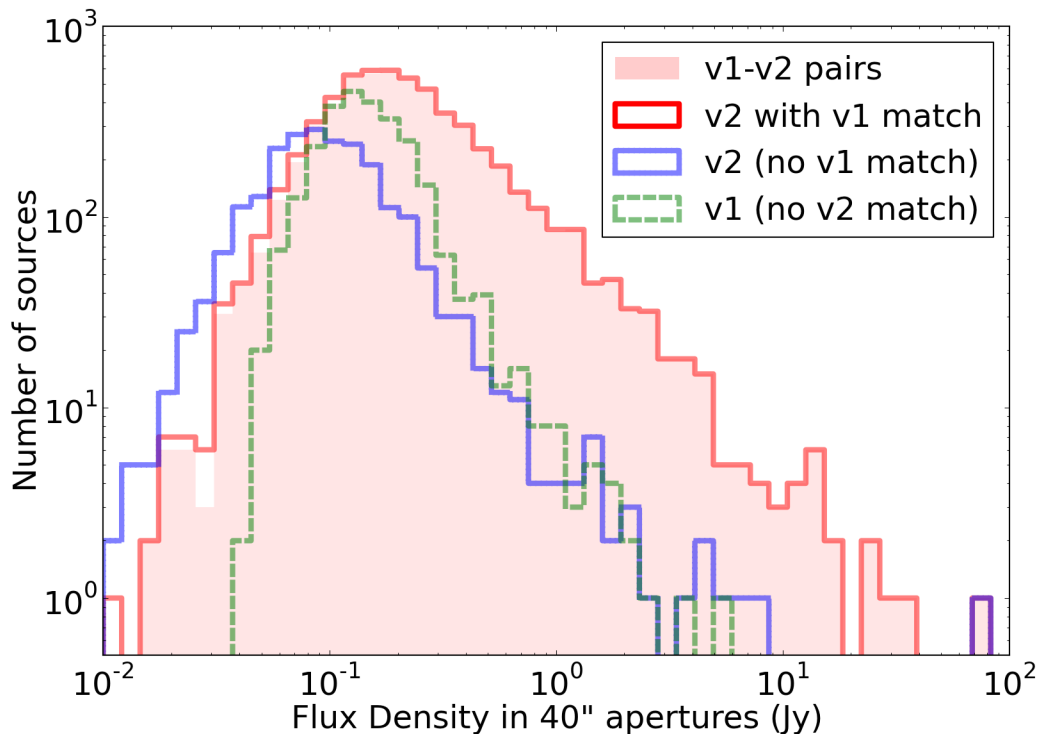


Figure 3.9 Histograms showing the sources matched between the v1.0 and v2.0 catalogs. Most of the v2.0 sources (5741 of 8004 v2.0 sources in the v1.0-v2.0 overlap region) have matches from v1.0, but there is a substantial population with no match. The unmatched sources tend to have lower flux densities. The shaded area shows 1-1 matches, while the solid red line shows one-way (unreciprocated) matches.

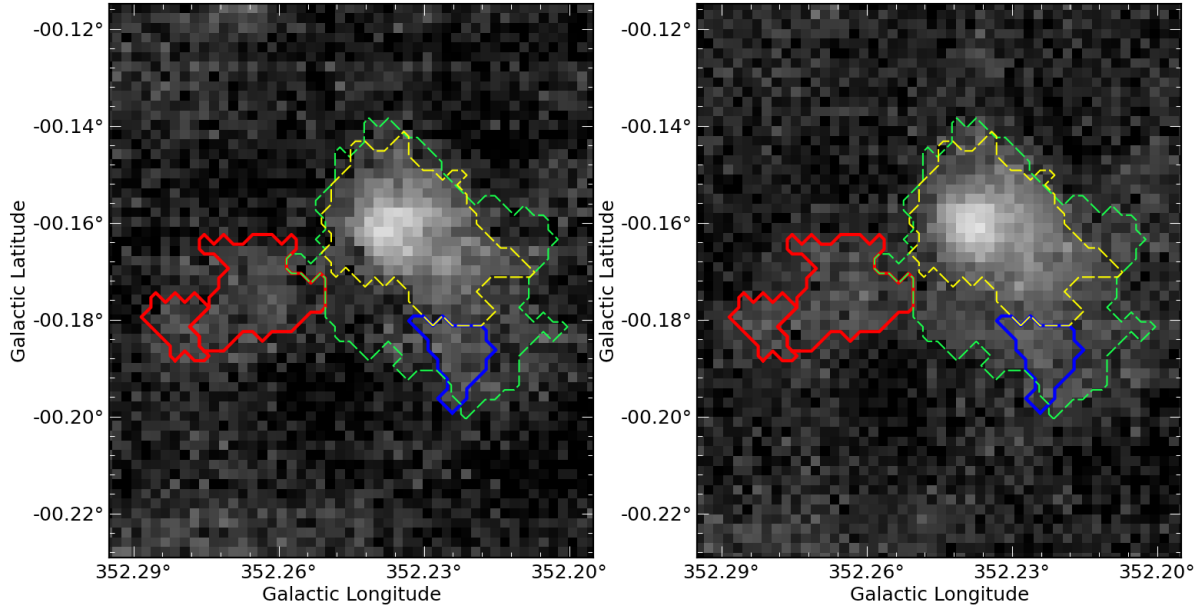


Figure 3.10 Contours of the extracted sources overlaid on grayscale images of a region in v1.0 (left) and v2.0 (right). The v1.0 data are scaled up by the $1.5\times$ calibration correction. The red contours show new v2.0 sources with no v1.0 match, while the blue contours show v1.0 sources with no v2.0 match. The green and yellow contours show v2.0 and v1.0 sources with a one-to-one match, respectively. In this example, the v2.0 source is significantly larger than the v1.0 source and merges with a shoulder that was classified as a separate source in v1.0. Additional v2.0 sources are detected because of increased signal-to-noise in the red-contoured regions.

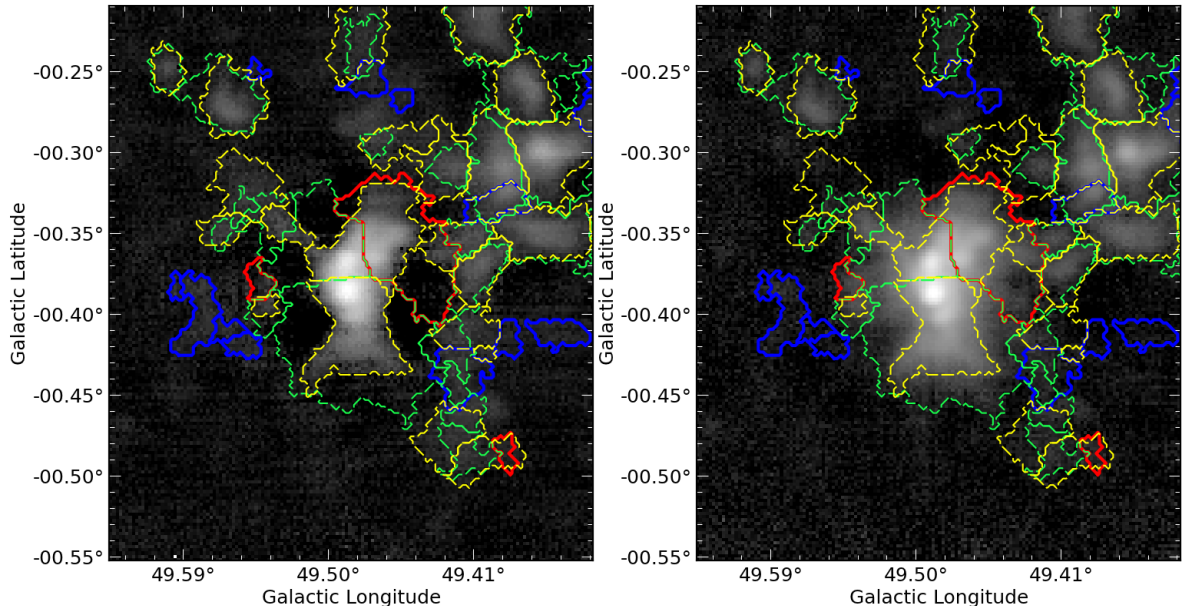


Figure 3.11 Same as Figure ??, but for the W51 complex. The area displayed is larger in order to encompass the entire source structure. The v2.0 sources are larger than the corresponding v1.0 sources because the negative bowl structures have been filled in. The red contour shows a region where v1.0 sources were detected, but because of crowding no nearest-neighbor pair was identified.

ratios of v2.0 to v1.0 source counts tend to occur along field edges both because of preferentially low source counts and because the v2.0 images have slightly greater extents in latitude than the v1.0. The figure provides a broad overview of the survey contents.

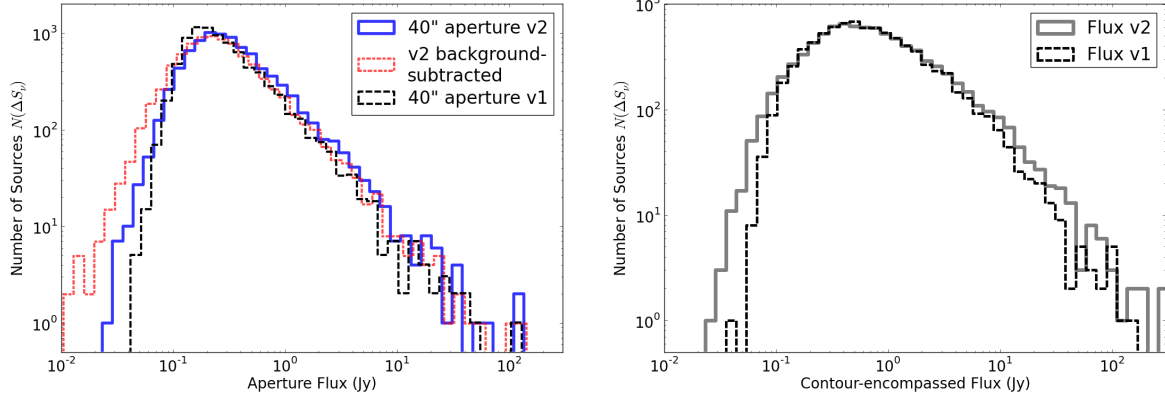


Figure 3.12 Comparisons of v1.0 and v2.0 flux density histograms. (*left*) Flux density distribution within $40''$ diameter apertures. The $40''$ apertures show the v2.0 data both with and without annular background subtraction; the v1.0 data are not background-subtracted. The histogram lines are slightly offset in order to minimize overlap. (*right*) Flux density distribution in contour-defined apertures. No background subtraction is performed for the contour-based flux densities in either version.

3.10 Conclusions

We presented Version 2 of the Bolocam Galactic Plane Survey, which is a significant improvement over v1.0 in pointing and flux calibration accuracy. The v2.0 data show an improvement in large angular scale recovery. The v2.0 release includes new observations of regions in the outer galaxy.

- We have characterized the angular transfer function of the Bolocam pipeline. The angular transfer function shows a sharp drop in recovered power above $\gtrsim 100''$ scales.
- We compared the pointing of the BGPS to that in Hi-Gal, and found that the surveys are consistent to within the measurement error $\sigma \approx 3.5''$.
- We measured the power spectral density in some regions and compared it to that in Hi-Gal, concluding that the power spectra are consistent with the normally used dust emissivity

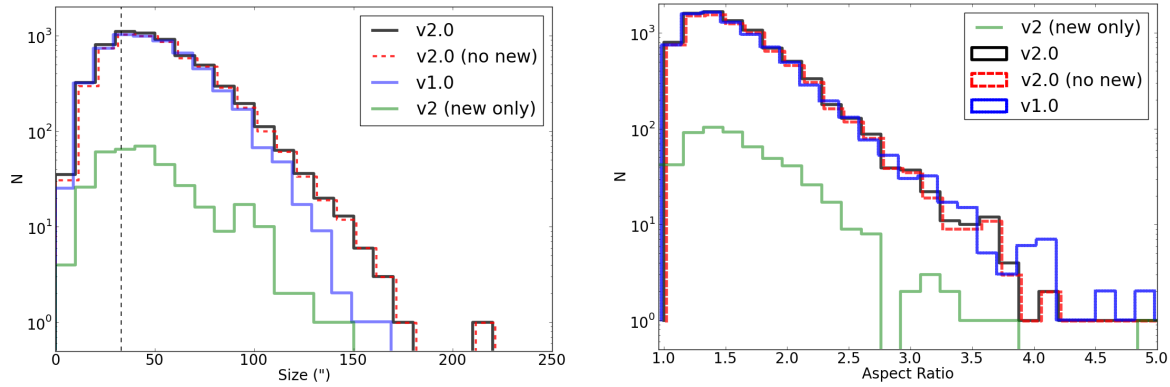


Figure 3.13 Distributions of deconvolved angular sizes (left) and aspect ratios (right) of sources in the BGPS catalog. The vertical dashed line in the left figure is plotted at the FWHM of the beam. The BGPS v2.0 includes newly observed regions not in the v1.0 survey, so separate histograms excluding the new (red dashed) and excluding the old (green solid) regions are shown. In both plots, the histograms are slightly offset to reduce line overlap.

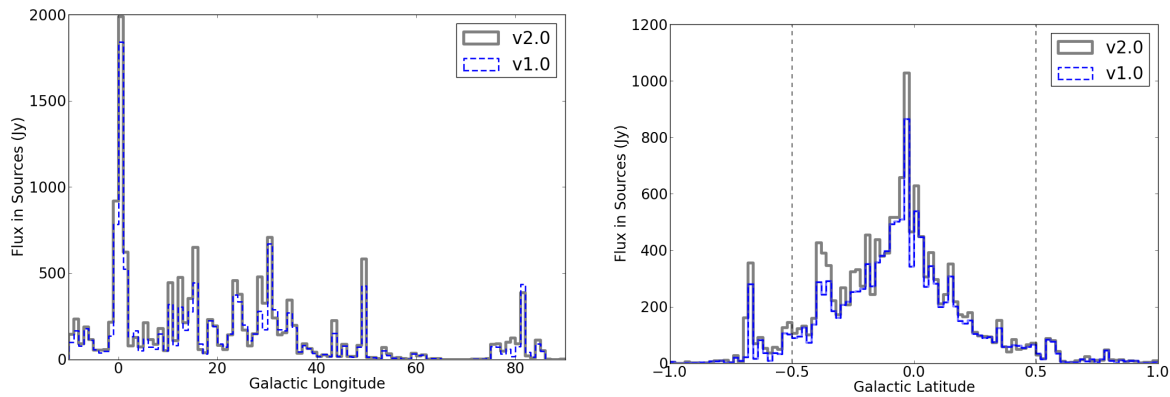


Figure 3.14 Distribution of total flux density in catalog sources as a function of longitude (*left*) and latitude (*right*) in the Galactic plane. The distributions contain sources extracted in the $-10^\circ < \ell < 90^\circ$ region. (*right*) Vertical dashed lines indicate the extent of complete coverage in the latitude direction ($\pm 0.5^\circ$). The large excess in v2.0 compared to v1.0 at $b \sim -0.4$ is due to the W51 complex, in which the flux density recovered in v2.0 was $1.5\times$ greater than in v1.0, largely because of reduced negative bowls around the brightest two sources (see Figure ??).

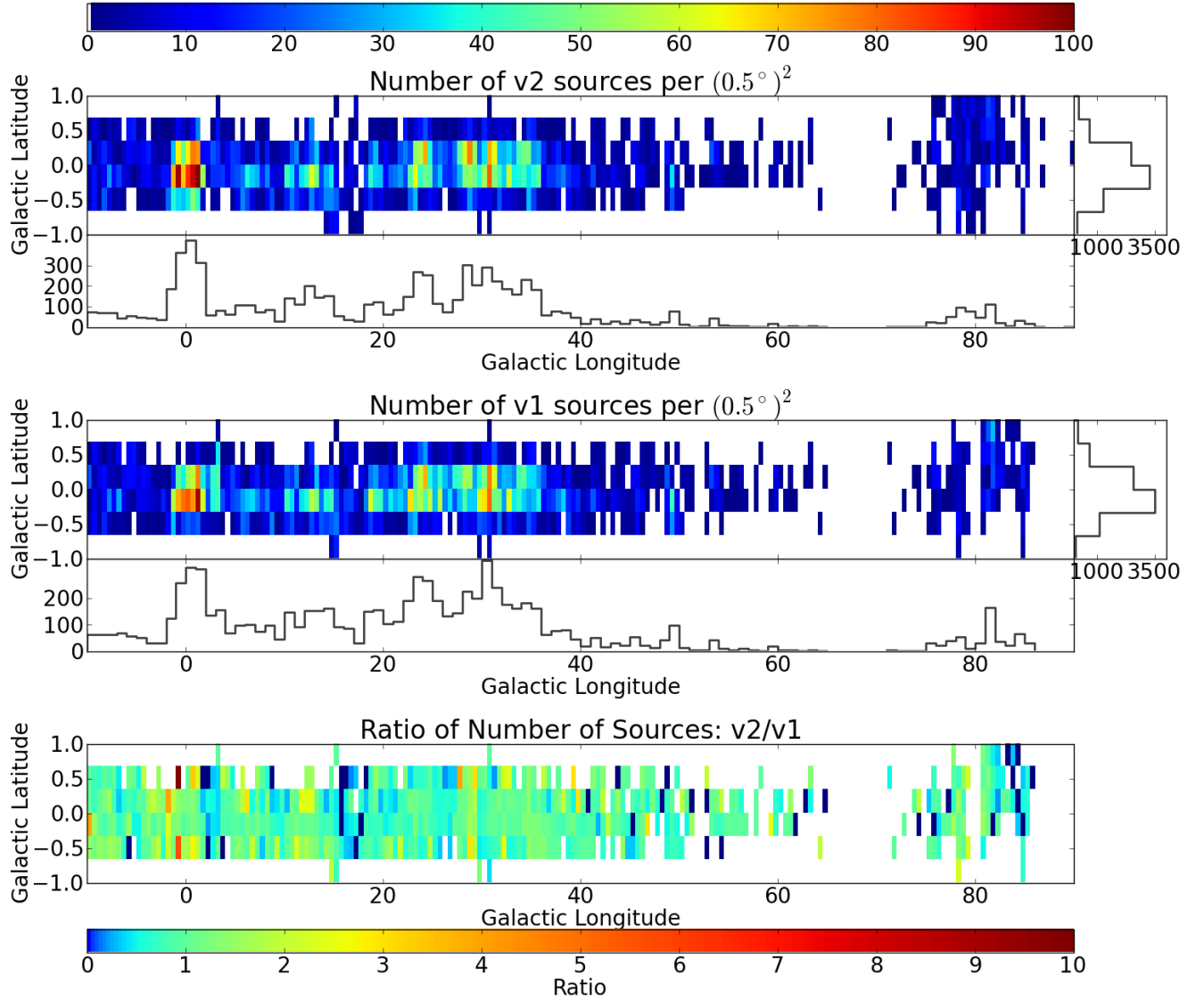


Figure 3.15 The two-dimensional distribution of source count in both v1.0 and v2.0. The colors in the first two panels illustrate the number of sources per half-degree-squared bin as indicated by the top colorbar. The bottom colorbar labels the ratio of the count of v2.0 to v1.0 sources. The histograms are coarse versions of Figure ?? and show the projection of the 2D histograms along each axis. A preference toward negative-latitude sources is evident at $\ell < 60$ deg, corresponding to our view of the Galaxy from slightly above the plane.

values in the range $\beta \sim 1.5 - 2$. The largest-scale structures appear to be the coolest.

- A new version of the catalog has been released. The improved quality of the v2.0 images has some effects on the BGPS catalog but the basic statistical properties of the catalog have not significantly changed. Because of changing noise properties within the images, only 70% of the individual sources in v2.0 have an obvious v1.0 counterpart and vice versa. The remaining 30% of sources do not have obvious counterparts because of two effects:
 - (1) At low significance, changing noise levels recover different features at marginal significance. It is likely that low significance sources in v1 and v2 are **both** real features but have been rejected in the other catalog because of the relatively conservative limits placed on catalog membership.
 - (2) At high significance, the catalog algorithm is dividing up complex structure using the underlying watershed algorithm. In this case, the precise boundaries between objects are sensitive to the shape of the emission. All of the high significance features appear in both catalogs, but the objects to which a piece of bright emission are assigned can vary.

Despite these changes in the catalogs, the overall statistical properties of the population show little variation except that the largest sources appear brighter and larger owing to better recovery of the large scale flux density.